



HAL
open science

Conjugated polymer blends for faster organic mixed ionic-electronic conductors

Micah Barker

► **To cite this version:**

Micah Barker. Conjugated polymer blends for faster organic mixed ionic-electronic conductors. Other. Université de Bordeaux, 2021. English. NNT : 2021BORD0401 . tel-03537553

HAL Id: tel-03537553

<https://theses.hal.science/tel-03537553v1>

Submitted on 20 Jan 2022

HAL is a multi-disciplinary open access archive for the deposit and dissemination of scientific research documents, whether they are published or not. The documents may come from teaching and research institutions in France or abroad, or from public or private research centers.

L'archive ouverte pluridisciplinaire **HAL**, est destinée au dépôt et à la diffusion de documents scientifiques de niveau recherche, publiés ou non, émanant des établissements d'enseignement et de recherche français ou étrangers, des laboratoires publics ou privés.

THÈSE PRÉSENTÉE
POUR OBTENIR LE GRADE DE

**DOCTEUR DE
L'UNIVERSITÉ DE BORDEAUX**

ECOLE DOCTORALE DES SCIENCES CHIMIQUES
SPECIALITE POLYMERES

Par Micah BARKER

**Conjugated polymer blends for faster organic
mixed ionic-electronic conductors**

Sous la direction du Prof. Georges Hadziioannou et du Prof. Natalie Stingelin

Soutenue le 20 Décembre 2021

Membres du jury :

M. Toupance, Thierry	Professeur, Université de Bordeaux	Président du Jury
M. Malliaras, George	Professeur, Cambridge University	Rapporteur
M. Salleo, Alberto	Professeur, Stanford University	Rapporteur
M. Berggren, Magnus	Professeur, Linköping University	Examineur
Mme. Inal, Sahika	Professeure agrégée, King Abdullah University of Science and Technology	Examinatrice
M. Brochon, Cyril	Professeur, Université de Bordeaux	Invité
M. Hadziioannou, Georges	Professeur, Université de Bordeaux	Directeur
Mme. Stingelin, Natalie	Professeure, Georgia Institute of Technology	Directrice

Mélange de polymères conjugués pour conducteurs ionique et électronique organiques plus rapides

Le fonctionnement de divers dispositifs électrochimiques organiques relève de leur propriété intrinsèque de conductivité mixte par les polymères π -conjugués. Un facteur clé, qui généralement limite les performances d'un dispositif, est le transport trop lent des ions à travers le polymère semiconducteur, nécessaire pour le dopage et dé-dopage en masse. De plus, de nombreux efforts ont été réalisés pour améliorer la conductivité ionique de différents polymères conjugués en travaillant chimiquement sur la polarité de la chaîne latérale sur ces matériaux. De tels groupements peuvent cependant impacter la structure de ces matériaux et rendre leurs propriétés électroniques sensibles aux conditions environnementales. Ce travail démontre la viabilité d'un mélange de polymères multicomposants comme alternative pour régler la conductivité mixte. Un copolymère à bloc hydrophile de poly(3-hexylthiophène) et poly(oxyde d'éthylène) (P3HT-*b*-PEO) est mélangé avec un copolymère aléatoire conducteur mixte de P3HT et poly(3-hydroxyhexylthiophène) (P3HT-*co*-P3HHT). Les transistors électrochimiques du mélange montrent une performance de transduction similaire au matériau P3HT-*co*-P3HHT pur à l'état stable, cependant le temps de réponse est grandement réduit. On attribue cela à un dopage électrochimique plus rapide puisque la captation des ions s'améliore quand on augmente l'hydrophilie du matériau grâce à l'ajout du copolymère à bloc. En parallèle, la partie P3HT du copolymère à bloc semble agir comme un compatibilisant qui améliore la stabilité structurale du mélange, améliorant ainsi la stabilité opérationnelle du dispositif. Par conséquent, notre travail impliquant cette ingénierie des copolymères à blocs pour fabriquer des mélanges compatibles est une méthode prometteuse pour améliorer les performances et la stabilité des matériaux conducteurs mixtes.

Mots clés : conducteurs mixtes, mélange de polymères semi-conducteurs, transistors électrochimiques organiques

Conjugated polymer blends for faster organic mixed ionic-electronic conductors

The operation of various organic electrochemical devices relies on the intrinsic mixed conducting properties of π -conjugated polymers. One key factor that generally limits device performance is the slow transport of ions throughout the semiconducting polymer, necessary for bulk doping and de-doping. Thus, there has been increasing efforts to enhance the ionic conductivity of various conjugated polymers by chemically engineering the polarity of the side chains of the material. Such substituents however can impact the structure of these materials and render their electronic properties sensitive to environmental conditions. This work demonstrates the viability of multicomponent polymer blending as an alternative approach to tune mixed conductivity. A hydrophilic block copolymer of poly(3-hexylthiophene) and poly(ethylene oxide) (P3HT-*b*-PEO) is blended with a mixed conducting random copolymer of P3HT and poly(3-hydroxyhexylthiophene) (P3HT-*co*-P3HHT). Electrochemical transistors of the blends exhibit similar transduction performance at steady state relative to those of the neat P3HT-*co*-P3HHT, however the response time is greatly reduced. We attribute this to faster electrochemical doping related to ion uptake due to the increased material hydrophilicity upon adding the block copolymer. Meanwhile, the P3HT-moiety of the block copolymer seems to act as a compatibilizer that can support the structural stability of the blend, which can subsequently support the operational stability of resulting devices. Thus, our work implies that engineering block copolymers to fabricate compatible blends is a promising method to enhance the performance and stability of mixed conducting materials.

Keywords: mixed conductors, semiconducting polymer blends, organic electrochemical transistors

General Table of Contents

List of Abbreviations and Symbols	xi
Résumé de Thèse	1
General Introduction	13
CHAPTER 1: Bibliographic research.....	19
1.1. Introduction	21
1.2. Organic electrochemical transistors.....	22
1.2.1. Basic operating principles.....	22
1.2.2. Physical model of OECTs.....	25
1.2.2.1. Steady-state characteristics.....	26
1.2.2.2. Transient characteristics.....	27
1.2.3. Influence of channel geometry on OECT performance	28
1.3. Key features of mixed ionic-electronic conducting polymers.....	31
1.3.1. Semiconducting behavior of conjugated polymers.....	31
1.3.2. Doping conjugated polymers	33
1.3.3. Ionic transport in mixed conducting polymers	36
1.3.4. Volumetric capacitance in mixed conducting polymers.....	39
1.3.5. Electronic charge transport in conjugated polymers	40
1.4. Progress in mixed conducting polymer design	44
1.4.1. Early mixed conducting polymers: Ppy and PANI	45
1.4.2. Polythiophene derivatives.....	47
1.4.3. Conjugated polyelectrolytes	49
1.4.4. Diketopyrrolopyrrole-based conjugated polymers.....	51
1.4.5. N-type polymers	53
1.4.6. Multicomponent polymer systems	56
1.5. Summary and research direction.....	60

General Table of Contents

1.6. References	64
CHAPTER 2: Mixed conducting polymer blends for faster organic electrochemical transistors.....	75
2.1. Introduction.....	77
2.2. OECT characteristics at various operating rates	77
2.2.1. P3HT-co-P3HHT.....	79
2.2.2. Blends with P3HT- <i>b</i> -PEO	81
2.2.3. OECT performance indicators, g_m and ΔV_t	83
2.3. Performance across different channel dimensions.....	86
2.3.1. Channel material performance indicator, μC^*	89
2.3.2. Influence of channel dimensions on current hysteresis	91
2.4. Performance across blend composition	93
2.5. Transient response	98
2.5.1. Response to a V_g pulse	98
2.5.2. Response to various V_g waveforms	100
2.6. Summary	101
2.7. References	102
CHAPTER 3: Modulation of electrochemical doping kinetics <i>via</i> blending	107
3.1. Introduction.....	109
3.2. Physical properties of P3HT-co-P3HHT blended with P3HT- <i>b</i> -PEO	109
3.2.1. Solid-state structure	109
3.2.2. Thermal properties.....	112
3.2.3. Surface polarity.....	117
3.3. Electrochemical properties.....	118
3.3.1. Cyclic Voltammetry	118
3.3.2. Spectroelectrochemistry	122
3.3.2.1. Electrochemical bleaching.....	123

3.3.2.2. Electrochemical doping rates.....	125
3.3.2.3. Monophasic exponential kinetic model	127
3.3.2.4. Biphasic exponential kinetic model	128
3.3.3. Impedance behavior.....	130
3.3.3.1. Equivalent circuit model-fitting.....	133
3.3.3.2. Volumetric capacitance, C^*	136
3.4. Summary	137
3.5. References.....	138
CHAPTER 4: Stability of mixed conducting polymer blends.....	143
4.1. Introduction	145
4.2. Operational stability of blends with P3HT- <i>b</i> -PEO	145
4.2.1. Transfer characteristics	146
4.2.1. Transient performance	147
4.2.2. Stability in water: preliminary QCM investigation	148
4.3. Blends of P3HT- <i>co</i> -P3HHT with PEO.....	152
4.3.1. Physical properties	152
4.3.2. Electrochemical properties	157
4.3.3. OECT performance	164
4.4. Stability of blends with PEO	167
4.4.1. Preliminary QCM analysis	167
4.4.2. OECT transfer characteristics	168
4.4.3. OECT transient characteristics	169
4.5. Summary	171
4.6. References.....	173
General conclusions and perspectives.....	177
APPENDIX: Methodology and supplementary information	183
A.1. Materials and film deposition	185

General Table of Contents

A.2. Organic electrochemical transistors (OECT)	186
A.2.1 Instrumentation	186
A.2.2 OECT device architecture	186
A.2.3 OECT measurement parameters.....	189
A.2.4 OECT operational stability in water	189
A.3. Characterization of physical properties	189
A.3.1 Grazing incidence wide angle x-ray scattering (GIWAXS)	189
A.3.2 Differential scanning calorimetry.....	190
A.3.3 Optical microscopy	191
A.3.4 Contact angle measurements.....	191
A.4. Electrochemical characterization.....	191
A.4.1 Cyclic voltammetry	192
A.4.2 Spectroelectrochemistry.....	193
A.4.3 Electrochemical impedance spectroscopy.....	194
A.5. Quartz crystal microbalance (QCM)	194
A.6. References	195

List of Abbreviations and Symbols

 Z 	Impedance magnitude
A_{0-0}/A_{0-1}	0-0/0-1 vibronic peak absorbance ratio
AC	Alternating current
Ag/AgCl	Silver chloride electrode
C	Capacitance
C^*	Volumetric capacitance
CE	Counter electrode
C_f	Mass sensitivity factor of a quartz microbalance sensor
CPE	Constant phase element
D	OECT drain electrode
d	Polymer film thickness
DC	Direct current
DSC	Differential scanning calorimetry
\bar{D}	Polymer dispersity
$E_{1/2}$	Half-wave potential from cyclic voltammetry
EIS	Electrochemical impedance spectroscopy
$E_{ox,on}$	Oxidation onset potential from cyclic voltammetry
E_{pa}	Peak anodic current from cyclic voltammetry
f	frequency
f_c	OECT cut-off frequency
G	OECT gate electrode
GIWAXS	Grazing-Incidence Wide-Angle X-ray Scattering
g_m	OECT transconductance
$g_{m,max}$	Maximum OECT transconductance
I_d	OECT drain current
I_g	OECT gate current

List of Abbreviations and Symbols

$I_{\text{ON/OFF}}$	OECT "on" to "off" drain current ratio
I_{ss}	OECT drain current at steady state
ITO	Indium tin oxide
j	j Operator
k	Rate constants
k_d^{-1}	Thickness-normalized rate constants
L	OECT channel length
M	Molar concentration in moles per liter
micro-OECT	Micro-scaled OECT
M_n	Polymer number average molecular weight
OECT	Organic electrochemical transistor
P3HHT	Poly(3-hydroxyhexylthiophene)
P3HT	Poly(3-hexylthiophene)
P3HT-<i>b</i>-PEO	Block copolymer of P3HT and PEO
P3HT-<i>co</i>-P3HHT	Random copolymer of P3HT and P3HHT
PDMS	Polydimethylsiloxane
PEO	Polyethylene oxide
QCM	Quartz crystal microbalance
R	Resistance
S	OECT source electrode
T_c	Crystallization onset temperature from thermograms
$T_{m,\text{end}}$	Melting endset temperature from thermograms
V_d	OECT drain voltage
V_g	OECT gate voltage
V_t	OECT threshold voltage
$V_{t,\text{fwd}}$	OECT V_t in forward V_g sweep
$V_{t,\text{rev}}$	OECT V_t in reverse V_g sweep
W	OECT channel width

WE	Working electrode
wt%	Percentage by weight
X_c	Reactance of a capacitor
Z	Complex impedance
Z_{im}	Imaginary part of complex impedance
Z_{re}	Real part of complex impedance
Δf	Frequency shift
ΔH	Enthalpy from integrating area under thermogram peaks
Δm	Change of mass
ΔV_t	OECT V _t difference between forward and reverse scan
θ	Phase angle associated with complex impedance
μ	Electron or hole mobility
τ	Time constant / OECT response time
ω	Angular frequency

Résumé de Thèse

Les performances des récents dispositifs électrochimiques organiques reposent principalement sur leur propriété unique à être à la fois des conducteurs ioniques et des conducteurs électroniques via les liaisons pi-conjuguées. Les propriétés électrochimiques de ces matériaux permettent un dopage en masse ainsi qu'un dé-dopage en présence d'électrolytes qui permettent de changer efficacement leur conductance. Ceci peut être exploité, par exemple, dans des bio-capteurs où la transduction entre les flux biochimiques ioniques et électroniques est nécessaire. De plus, les interactions équilibrant les charges entre les ions injectés et les charges déjà présentes dans le polymère entraînent de larges capacités volumétriques. Ces dernières peuvent contribuer d'avantage aux fortes magnitudes des signaux de transduction, lorsqu'elles sont exploitées dans un dispositif. Cependant, ces phénomènes semblent reposer sur le mouvement des ions au niveau de l'interface polymère-analyte, ainsi que dans le polymère lui-même. La vitesse de réponse des dispositifs est ainsi limitée par la conductivité ionique du matériau actif. Par conséquent de nombreux travaux ont été menés pour élargir la gamme des matériaux disponibles, ayant des propriétés conductives mixtes, en améliorant l'efficacité du transport ionique dans ces matériaux.

Nous avons démontré que l'association d'un polymère conducteur mixte avec un composé hydrophile conducteur d'ions, est une stratégie simple et efficace pour améliorer le transport ionique dans ces matériaux. Cette méthode permet d'augmenter la fonctionnalité du matériau sans avoir recours à de modifications chimiques complexes de la structure du polymère semi-conducteur. En effet ces dernières requièrent souvent une substitution par des groupements complexes, encombrants ou polaires, qui peuvent avoir un effet néfaste sur l'ordre moléculaire du polymère et donc sur ses propriétés électriques. Pour le conducteur mixte actif, nous avons sélectionné le copolymère poly(3-hexylthiophène) et poly(3-(6-hydroxyhexylthiophène) (P3HT-co-P3HHT; masse molaire

moyenne en nombre $M_n = 30 \text{ kg/mol}$, dispersité $\mathcal{D} = 1.9$, **Figure i.1**, gauche). En effet, des travaux précédents ont montré que ce matériau permet une réponse électrochimique rapide, sans gonflement excessif qui pourrait détériorer ses propriétés sur le long terme, lorsqu'il est utilisé en électrolyte aqueux. Le P3HT-co-P3HHT a été mélangé avec un copolymère à bloc de P3HT et de poly(oxyde d'éthylène) (P3HT-*b*-PEO, $M_n, P3HT = 5 \text{ kg mol}^{-1}$, $\mathcal{D}_{P3HT} = 1.2$, $M_n, PEO = 20 \text{ kg mol}^{-1}$, $\mathcal{D}_{PEO} \leq 1.2$, **Figure i.1**, droite), pour améliorer le caractère hydrophile et la conductivité ionique du matériau. De plus, le bloc P3HT pourrait agir comme compatibilisant pour limiter la séparation de phase à grande échelle, contribuant ainsi la stabilité structurale du mélange, particulièrement lorsqu'il est utilisé dans des milieux riches en eau.

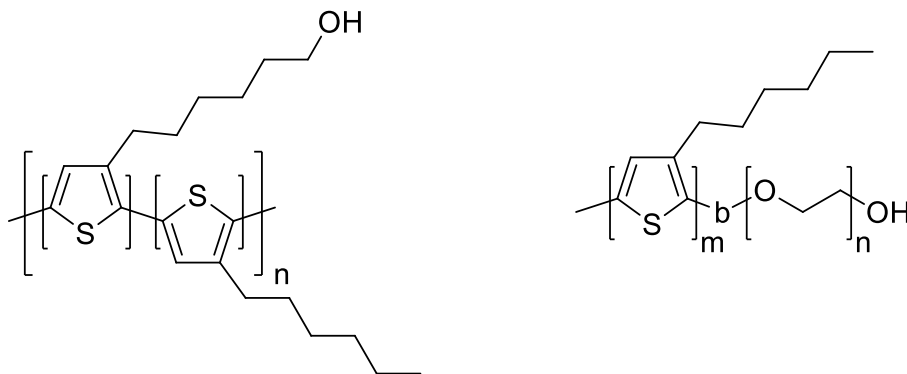


Figure i.1. Structures chimiques du P3HT-co-P3HHT (à gauche) et P3HT-*b*-PEO (à droite).

Premièrement, nous avons évalué l'impact du mélange sur la conductivité mixte du matériau et les performances des dispositifs, en réalisant et caractérisant des transistors électrochimiques organiques (OECT). Ces derniers sont généralement constitués d'une électrode grille (G) immergée dans un électrolyte (0.1 M KCl), qui a une interface avec le

polymère actif, lui-même en contact avec les électrodes source (S) et drain (D). (Figure i.2, en haut)

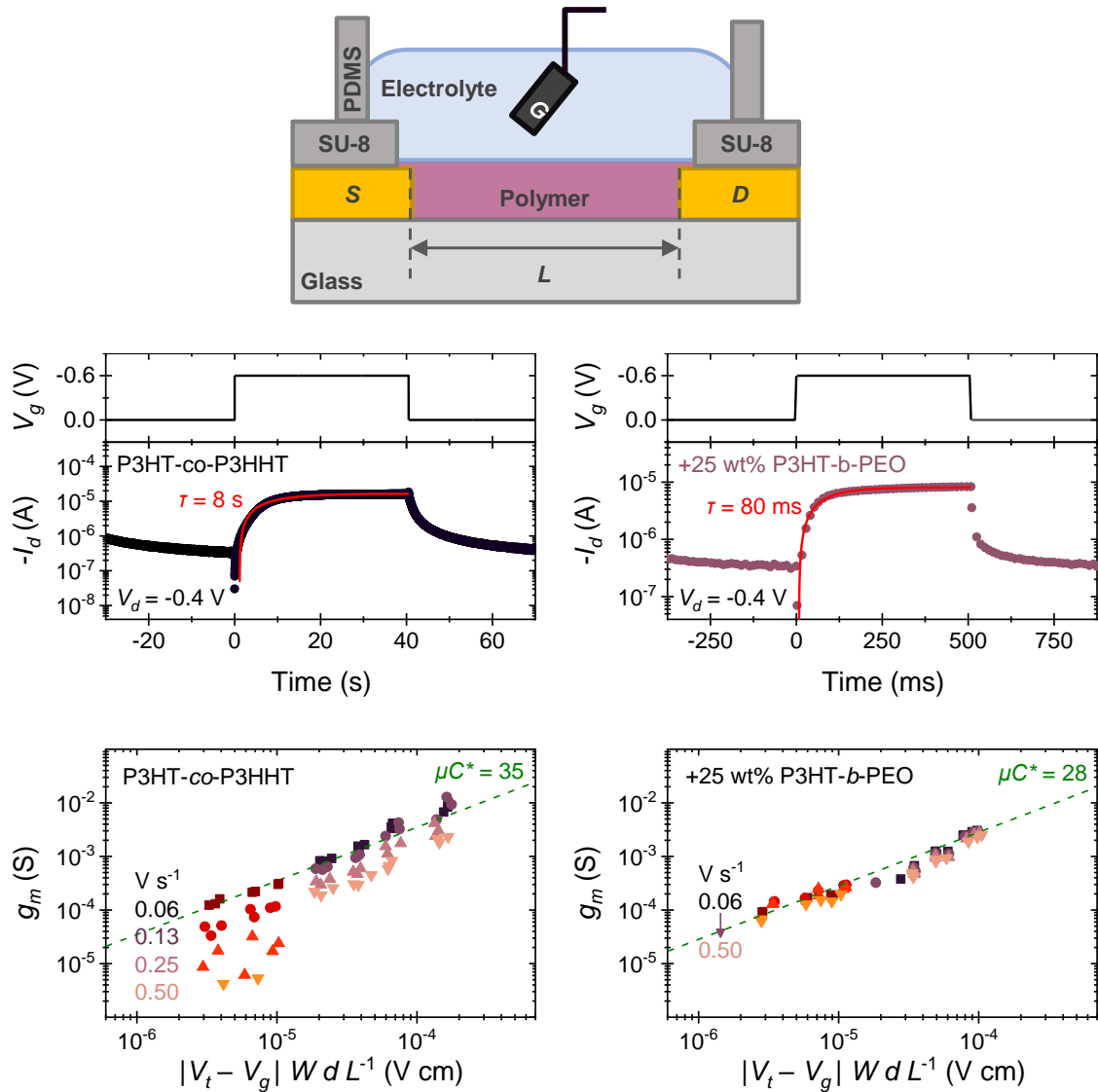


Figure i.2. Architecture générale des OEETs utilisés dans ces travaux (en haut).

Courants transitoires mesurés pour des OEETs faits de P3HT-co-P3HHT et leurs mélanges avec 25 wt% de P3HT-b-PEO avec des constantes de temps (τ) indiquées en rouge (au milieu). Influence du taux de balayage de la tension de grille ($V s^{-1}$) sur mise à l'échelle de la transconductance (g_m) avec la géométrie du dispositif et les paramètres de polarisation dans les OEET du matériau pur et de son mélange (en bas). μC^* moyennes extraites de la régression linéaire des pentes représentées en vert.

Les résultats indiquent que le mélange affecte tout d'abord les performances transitoires des OECT. Plus particulièrement, le P3HT-*co*-P3HHT pur a un long temps de réponse OECT ($\tau = 8$ s) qui est extrait depuis le courant transitoire au niveau du drain après application d'une différence de potentiel. Il en résulte que les performances en transduction des OECTs (indiquées par la transconductance g_m et extraite de mesures de I_d après un balayage en tension de la grille (V_g)), sont particulièrement sensibles à la vitesse de balayage des paramètres étudiés ici. En effet, ces résultats de transduction peuvent diminuer de deux ordres de grandeur lorsque la vitesse de balayage V_g passe de 0.1 à 1 V s⁻¹. La détermination de μC^* , figure de mérite des OECTs, permet de différencier et décrire les performances des matériaux utilisés comme canal des transistors. Cette figure de mérite peut être obtenue en caractérisant le g_m de différents dispositifs en faisant varier la taille des canaux, dans la gamme de V_g utilisée ici. Le paramètre μC^* varie ainsi grandement suivant la vitesse de balayage utilisée (**Figure i.2**, en bas à gauche). Les valeurs de μC^* extraites pour P3HT-*co*-P3HHT varient de 10 à 55 F cm⁻¹ V⁻¹ s⁻¹, avec une moyenne à 35 F cm⁻¹ V⁻¹ s⁻¹. Ces résultats semblent indiquer que la vitesse d'injection des charges impliquées dans le dopage électrochimique de P3HT-*co*-P3HHT, lors de l'utilisation du dispositif, est faible. Ces résultats soulignent aussi l'importance de la résolution temporelle lorsque des conducteurs mixtes « lents » sont étudiés. D'autre part, mélanger du P3HT-*co*-P3HHT avec 25 wt% de P3HT-*b*-PEO permet d'obtenir une vitesse de réponse plus courte (temps de réponse plus court, $\tau = 80$ ms, **Figure i.2**, au milieu à droite). Les valeurs de transconductance g_m de ces dispositifs sont stables sur une large gamme de tension de grille V_g , même jusqu'à 10 V s⁻¹, et un μC^* de 28 F cm⁻¹ V⁻¹ s⁻¹ avec des variations minimales est mesuré (**Figure i.2**, en bas à droite). Nous remarquons que cette valeur n'est pas très différente du matériau pur, impliquant que le mélange n'a pas d'effet marqué sur les performances en masse du matériau dopé. De plus, le I_d à saturation des courants transitoires (**Figure i.2**, au milieu) pour les deux polymères sont virtuellement équivalents ($\approx 10^{-5}$ A) (en considérant les mêmes paramètres et dimensions des canaux). Ces résultats

montrent que mélanger P3HT-co-P3HHT avec du P3HT-b-PEO permet d'améliorer efficacement la vitesse de réponse des OECTs, sans trop affecter négativement sa performance à l'état d'équilibre.

Nous supposons que cette amélioration des performances à l'état d'équilibre des OECT est dû à une augmentation de l'hydrophilie du matériau de canal lors de l'ajout de PEO, ce qui pourrait entraîner une interdiffusion plus efficace des ions entre le film polymère et l'électrolyte aqueux externe. Nous supposons également que le bloc P3HT, lié chimiquement au PEO, contribue à stabiliser le mélange et limite la séparation de phase à une échelle microscopique, entraînant une distribution macroscopique uniforme des composants. Ceci pourrait aider au maintien des propriétés électriques en masse du matériau, expliquant ainsi que les propriétés à l'état d'équilibre des OECTs restent relativement constantes, même après mélange. Pour étudier d'avantage ces notions, nous avons examiné en quoi le mélange (réalisé de la même façon que lors de la fabrication des OECTs) affecte les propriétés physiques et électrochimiques du matériau.

Les premières caractérisations de mélange de P3HT-co-P3HHT/P3HT-b-PEO, préparé en solution, indiquent que les composants ne sont pas dans la même phase, mais il semblerait qu'ils aient un certain degré de compatibilité, lié à leur comportement en température (**Figure i.3**, en haut à gauche). De par cette séparation de phase, l'ordre à courte et longue distances obtenu dans les films de P3HT-co-P3HHT, n'est pas particulièrement affecté après mélange (d'après mesures d'absorbance et de GIWAXS, respectivement). Aucune séparation de phase à grande échelle n'a pu être observée par microscopie optique, à cause de certaines compatibilités dans le mélange (**Figure i.3**, en haut à droite).

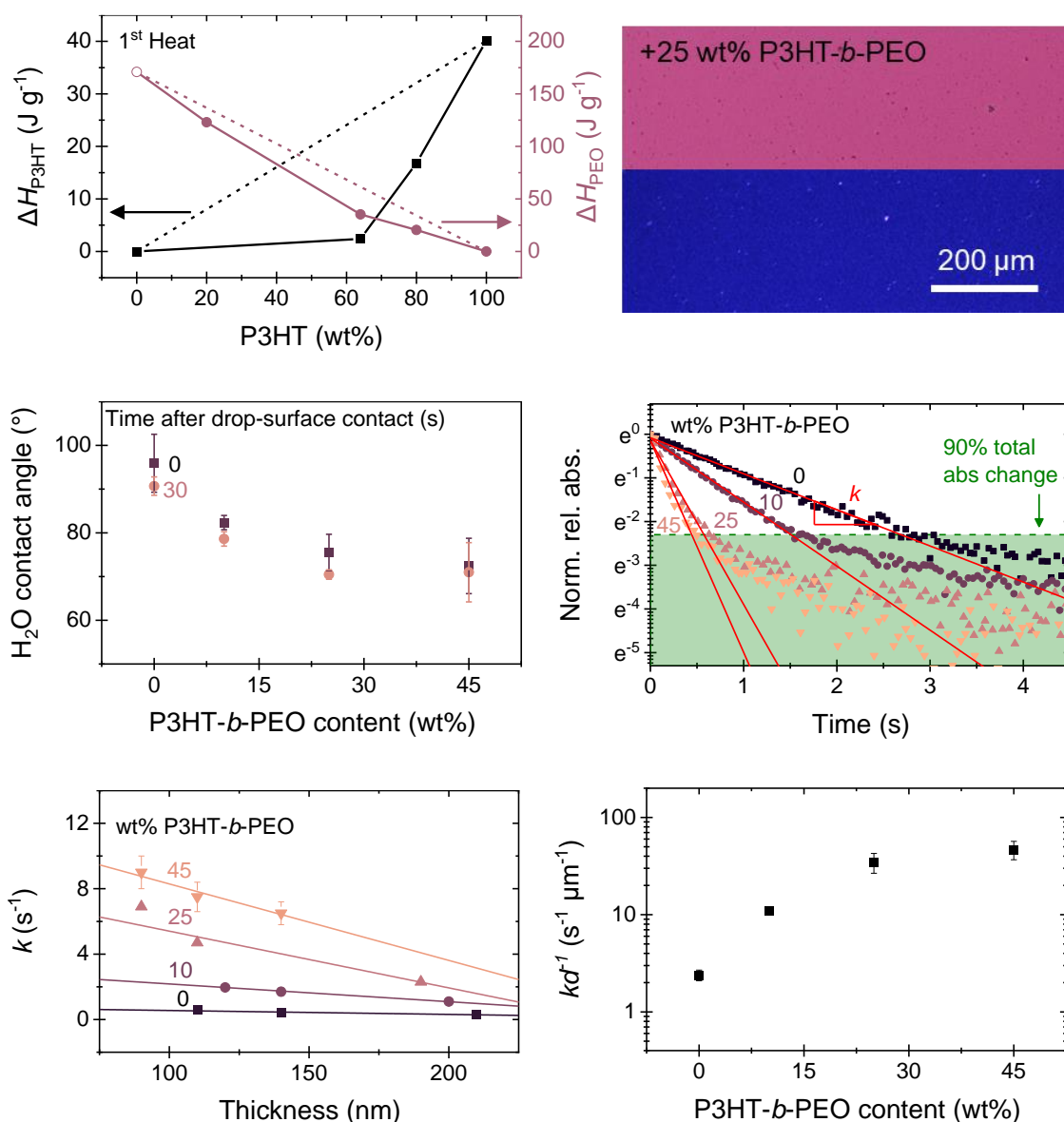


Figure i.3. Enthalpies (ΔH) de mélange du P3HT (incluant le P3HHT) et du PEO dans des solutions de diverses compositions extraites de leur thermogrammes (haut, gauche). Les tirets indiquent les valeurs «idéales» pour des phases complètement séparées. Les enthalpies inférieures à leur valeur idéale indiquent un manque de cristallisation dû à la compatibilité entre les phases. Image de microscopie optique d'un mélange ne montrant aucune séparation de phase à grande échelle même lorsqu'elle est vue sous polarisation croisée pour observer la biréfringence (en haut à droite). Angles de contacts avec l'eau des mélanges (au milieu à gauche). Absorbance transitoire lors du dopage électrochimique des polymères avec des ajustements exponentiels indiqués en rouge pour extraire les taux de dopage (k ; au milieu à droite). Normalisation de k à l'épaisseur du film (en bas à gauche). k normalisé par l'épaisseur en fonction de la composition du mélange (en bas à droite).

D'autre part, le mélange diminue nettement l'angle de contact de l'eau sur les films (**Figure i.3**, à gauche), ce qui pourrait indiquer une augmentation de l'hydrophilie de la surface, et donc une meilleure compatibilité entre l'interface polymère et un milieu riche en eau. Par conséquent, les mélanges semblent augmenter l'efficacité de fixation des ions lorsqu'ils sont utilisés dans des électrolytes aqueux, ce qui entraîne une augmentation drastique de la vitesse des procédés de dopage, observés par spectro-électrochimie (**Figure i.3**, au milieu à droite). La constante de vitesse spectro-électrochimique kd^1 rapportée à l'épaisseur du film peut être estimée par une courbe de tendance exponentielle des absorptions transitoires des films de différentes épaisseurs, en considérant qu'elle est proportionnelle à la vitesse de dopage électrochimique. Cette constante kd^1 , d'environ $2.4 \pm 0.3 \text{ s}^{-1} \mu\text{m}^{-1}$ pour le P3HT-*co*-P3HHT pur, pourrait être augmentée d'au moins un ordre de grandeur en le mélangeant avec seulement 25 wt% de P3HT-*b*-PEO ($kd^1 \approx 35 \pm 8 \text{ s}^{-1} \mu\text{m}^{-1}$), alors qu'une augmentation plus faible est observée avec une quantité de copolymère à blocs plus importante ($kd^1 \approx 48 \pm 10 \text{ s}^{-1} \mu\text{m}^{-1}$) (**Figure i.3**, en bas). Inversement, la capacitance volumétrique du P3HT-*co*-P3HHT ($190 \pm 30 \text{ F cm}^{-3}$), extraite d'un modèle de circuit équivalent qui s'adapte au spectre d'impédance des films dopés, ne semble pas changer lors du mélange. Cela pourrait indiquer que la densité des porteurs de charges, dont nous supposons qu'ils interagissent avec les ions injectés pour contribuer aux capacités à double couche en masse, est relativement similaire dans les différentes compositions de mélange. Cela implique qu'une grande partie du P3HT-*co*-P3HHT pur ne participe pas lui-même à la formation et au transport des porteurs de charges. Nous soupçonnons alors que les propriétés électriques du matériau en masse peuvent être relativement insensibles au mélange avec un composant électroniquement isolant, tant qu'il maintient l'ordre structurel nécessaire du composant semi-conducteur actif dans les films résultants. Nous pensons que cela est le cas dans nos mélanges car ils présentent une séparation de phase sur des échelles de longueur très fines. Ceci expliquerait donc les

performances électriques C^* et OECT soutenues des mélanges par rapport à celles du matériau pur.

Outre l'induction d'une séparation de phase à des échelles de longueurs microscopiques, nous soupçonnons également que l'effet de compatibilité du bloc P3HT, chimiquement lié au PEO lorsqu'il est mélangé avec P3HT-co-P3HHT, devrait aider à maintenir la stabilité structurale et, par la suite, les performances à long terme du dispositif. Pour tester cela, nous examinons les performances de leurs OECTs lors d'un stockage prolongé dans l'eau. Le dispositif de P3HT-co-P3HHT pur présente un fonctionnement stable indiqué par des courants transitoires relativement reproductibles même après un mois de mesures répétées et d'immersion continue dans l'eau (**Figure i.4**, en haut à gauche). Lors du mélange avec P3HT-*b*-PEO, bien que le transistor montre des performances transitoires initialement améliorées, sa vitesse de réponse ralentit finalement après deux semaines, indiquée par une augmentation de sa constante de temps de 80 ms à environ 4 s (**Figure i.4**, en haut à droite). L'analyse via microbalance de Quartz (QCM) préliminaire suggère que le mélange semble perdre environ 10 % de sa masse lors d'une exposition prolongée à des milieux aqueux, ce que nous attribuons à la fraction PEO soluble dans l'eau ainsi qu'à sa faible masse moléculaire. Pour explorer un peu plus cela, nous étudions des mélanges de P3HT-co-P3HHT et d'un homopolymère PEO du même masse moléculaire que la fraction PEO dans le copolymère à blocs ($M_{n,PEO} = 20 \text{ kg mol}^{-1}$). Nous constatons que le mélange avec le PEO affecte les propriétés du matériau tout comme le mélange avec le copolymère à blocs, ce qui semble-t-il, pourrait permettre d'éviter les étapes de synthèse supplémentaires nécessaire à la fabrication d'un copolymère à blocs. Plus spécifiquement, les deux mélanges présentent une diminution de l'angle de contact à 70° avec l'eau et une amélioration similaire des taux de dopage électrochimique par rapport au matériau pur. Cela pourrait indiquer que l'effet du mélange sur les propriétés transitoires du conducteur mixte est dicté par la fraction de PEO. En outre, nous déterminons que seulement 20 wt% de teneur en PEO dans l'un ou l'autre système suffit à moduler

efficacement les propriétés du matériau. En conséquence, les OECTs du mélange avec PEO présentent un comportement transitoire amélioré indiqué par des temps de réponse relativement faibles ($\tau = 70$ ms). En même temps, la capacité volumétrique des mélanges avec PEO est relativement similaire à celle du matériau pur (190 ± 30 F cm⁻³). Par la suite, les OECTs comprenant le mélange avec le PEO présentent des caractéristiques à l'état d'équilibre similaires et un paramètre μC^* (14 F cm⁻¹ V⁻¹ s⁻¹) dans la plage de celle du P3HT-co-P3HHT pur (10 - 55 F cm⁻¹ V⁻¹ s⁻¹). Toutefois, le système comprenant 25 % en masse de l'homopolymère PEO présente une plus grande séparation de phases et moins de preuves de compatibilité, notamment indiquée par ses propriétés thermiques, ce qui pourrait conduire à une stabilité structurale moindre. En effet, une analyse QCM préliminaire suggère que les mélanges avec PEO peuvent présenter une perte d'environ 20 % en poids de matière lors d'une exposition prolongée à des milieux aqueux, plus élevée que celle observée dans les mélanges avec le copolymère à blocs. En conséquence, ces dispositifs présentent une mauvaise stabilité opérationnelle à long terme (**Figure i.4**, en bas à gauche), montrant ainsi une dégradation plus rapide et plus importante de ses performances transitoires, de $\tau = 70$ ms à environ 30 s, que celle observée dans le mélange avec le copolymère à blocs dans la semaine de stockage continu dans l'eau (**Figure i.4**, en bas à droite). La stabilité supérieure à long terme des mélanges avec le copolymère à blocs pourrait être due à sa compatibilité et également au bloc P3HT hydrophobe lié au PEO, qui aide à limiter sa solubilité et soutient donc la stabilité structurale du mélange. Ces résultats ouvrent des opportunités pour de futures recherches sur la conception et l'ingénierie de copolymères à blocs en tant que co-composants prometteurs pour améliorer les performances et la stabilité des mélanges de polymères conducteurs mixtes.

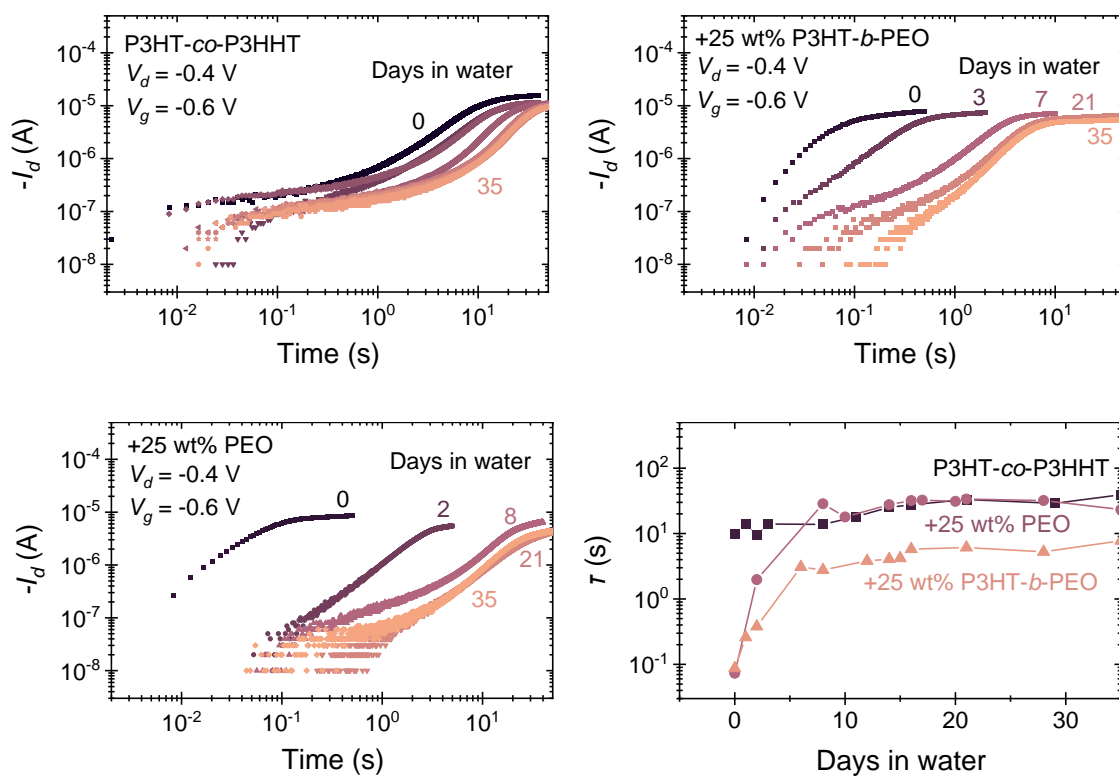


Figure i.4. Evolution de l' I_d transitoire du système P3HT-co-P3HHT (en haut à gauche) et ses mélanges avec le P3HT-b-PEO (en haut à droite) et le PEO (en bas à gauche) lors d'une immersion continue dans l'eau en fonction du temps. Evolution de la constante de temps (τ , en bas à droite) extraite à partir des courants transitoires mesurés lors de ce même stockage dans l'eau.

General Introduction

The rapid growth in the field of organic bioelectronics over the past two decades demonstrates the potential of π -conjugated polymers to be the primary active materials in future commercial medical technologies. Among the key features of these materials are their unique electrochemistry and mixed ionic and electronic conducting properties that leads to bulk doping and/or de-doping in the presence of electrolytes, which can be exploited in applications where transduction between biochemical ionic fluxes and electronics is required. For instance, the charge-balancing interaction of ionic species with polarons during electrochemical oxidation (or reduction) of the conjugated backbone not only modulates the conductivity of the material but also induces large volumetric capacitances, which contributes to high signal amplification when integrated in biosensors. However, these phenomena seem to rely on the movement of ions across the polymer-analyte interface and within the polymer itself, thereby limiting the response speed of devices across various applications to the ionic conductivity of the active material. Thus, in the quest to expand the range of options for organic mixed conducting materials there has been great interest to enhance the ionic transport efficiency of various conjugated polymers.

One common strategy to develop new classes of polymeric mixed conductors involves chemically engineering the polarity of side chains functionalized on a conjugated backbone. Polythiophene derivatives with different substituents including acidic moieties, ionic species, and oligo(ethylene glycol) side chains have been explored. The resulting materials show mixed conductor properties such as enhanced ionic conductivity, bulk electrochemical doping, and high volumetric capacitances, and offer features such as depletion, accumulation, or ambipolar modes of device operation. Although this has led to the steady growth of the polymer mixed conductor library, the limitations of single-component materials have also become more apparent. For example, most of conjugated polyelectrolytes are usually water-soluble and require cross-linkers or bulky counter-ions to

be compatible with aqueous applications. In another case, although glycol modification of sidechains results in the highest augmentation of the capacitance in conjugated polymers, which leads to materials exhibiting the highest steady-state transduction performance in organic electrochemical transistors (OECTs), significant water uptake during operation can bring about irreversible morphological changes in the conjugated structure that heavily impact their electrical properties and device stability. This renders the optoelectronic properties of these materials sensitive to humidity. Furthermore, bulky and charged side groups can lead to torsional disorder in the backbone which has detrimental effects on charge-carrier mobility. Often the synthesis of a series of derivatives incorporating multiple monomers to rearrange side group and backbone unit distribution is required to further tune material performance. The mechanisms of OECT operation, the key features of mixed conducting polymers, and the recently reported polymers that have been designed and applied to OECTs are discussed further in **Chapter 1** of the manuscript.

Polymer blending is another viable method that can incorporate various functionalities into a material without the need for complex chemical design on the active semiconducting polymer itself. We demonstrate here that we can greatly expedite the response speed of electrochemical devices operating in accumulation mode by blending a mixed conductor with an ion-conducting block copolymer, while using simple low-temperature, solution-based techniques, and without the need for special post-processing treatments. As the active mixed conductor, we selected the random copolymer of poly(3-hexyl thiophene) and poly[3-(6-hydroxy)hexyl thiophene] (P3HT-*co*-P3HHT, 50% comonomer composition) in which the hydroxyhexyl ($-C_6H_{12}OH$) side chain modification enhances this material's electrochemical response at low potentials in aqueous media, without drastically changing the molecular order and mechanical properties of solution-cast films even after operation. This was blended with a block copolymer of P3HT and poly(ethylene oxide) (P3HT-*b*-PEO) to enhance the hydrophilicity and ionic conductivity of the material. Furthermore, the P3HT block as a compatibilizer may limit large scale phase

separation, which can help preserve the electronic properties of the semiconducting material and maintain its stability especially in the context of water-rich environments. The rationale for choosing these materials is detailed more in the conclusion of **Chapter 1**. In **Chapter 2**, we show that adding P3HT-*b*-PEO to P3HT-*co*-P3HHT does indeed permit faster OECT operation while apparently preserving its ion-electron transduction performance at steady state. This correlates with further electrochemical characterization of the blends, discussed in **Chapter 3**, which indicate that blending enhances the electrochemical doping kinetics of the material operating in aqueous electrolyte but without changing its volumetric capacitance. Finally, in **Chapter 4**, we show the potential of block copolymers as co-components in mixed conducting polymer blends to sustain long-term structural stability and device performance during operation in water-rich media.

CHAPTER 1:

Bibliographic research

1.1. Introduction	21
1.2. Organic electrochemical transistors.....	22
1.2.1. Basic operating principles.....	22
1.2.2. Physical model of OECTs.....	25
1.2.2.1. Steady-state characteristics.....	26
1.2.2.2. Transient characteristics.....	27
1.2.3. Influence of channel geometry on OECT performance	28
1.3. Key features of mixed ionic-electronic conducting polymers.....	31
1.3.1. Semiconducting behavior of conjugated polymers.....	31
1.3.2. Doping conjugated polymers	33
1.3.3. Ionic transport in mixed conducting polymers	36
1.3.4. Volumetric capacitance in mixed conducting polymers.....	39
1.3.5. Electronic charge transport in conjugated polymers	40
1.4. Progress in mixed conducting polymer design	44
1.4.1. Early mixed conducting polymers: Ppy and PANI.....	45
1.4.2. Polythiophene derivatives.....	47
1.4.3. Conjugated polyelectrolytes	49
1.4.4. Diketopyrrolopyrrole-based conjugated polymers.....	51
1.4.5. N-type polymers	53
1.4.6. Multicomponent polymer systems	56
1.5. Summary and research direction.....	60
1.6. References.....	64

1.1. Introduction

Mixed ionic-electronic conducting polymers have attracted much attention over recent years due to their increasing application in the field of bioelectronics.¹ These materials are ideal candidates for interfacing between biology and electronics for several reasons, one of which is that their chemistry consists mainly of carbon, hydrogen, nitrogen, and oxygen atoms, which matches that of biological molecules.² Their mechanical stiffness can also be tuned to be more compatible with that of biological tissue. Furthermore, they can be easily biofunctionalized using a variety of synthetic techniques. Meanwhile, owing to the unique electrochemical properties of conjugated polymers, they may conduct both ions and electrons, which offers a mechanism to efficiently transduce between ionic and electronic signals.

One particular device whose operation relies heavily on the intrinsic properties of mixed conducting polymers is the organic electrochemical transistor (OECT).³ Owing to its device architecture, OECTs are amplifiers. However, with a mixed conducting polymer as the active channel material, OECTs can yield large output signals compared to that of other related organic thin film transistors. Additionally, multiple conductance states of the channel can be achieved depending on the applied input voltage. As a result, OECTs have gained interest for applications in biosensing and neuromorphic memory storage.^{2,3} Another practical use for OECTs is that their characterization can offer plenty of insight into the properties of the active mixed conducting polymer. This requires some understanding of the basic operating principles and device physics of OECTs. Determining the key performance indicators of OECTs allows the extraction of materials-specific parameters such as the charge carrier mobility and volumetric capacitance. Comparison of the performance of OECTs employing different channel materials can also be used to benchmark mixed conducting polymers. Thus, OECTs are indispensable tools in the quest to expand the range of polymers that can be used for applications in bioelectronics.

1.2. Organic electrochemical transistors

1.2.1. Basic operating principles

The typical architecture of an OEET shown in **Figure 1.1** consists of a gate electrode immersed in an electrolyte that is in contact with a conjugated polymer film, which is also in contact with a source and a drain electrode separated over a length L that makes up the channel across which holes and electrons flow during operation.

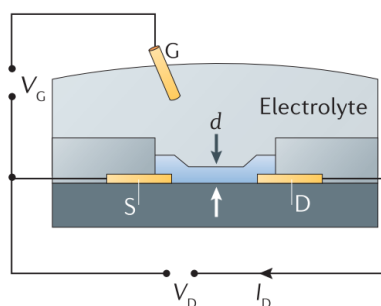


Figure 1.1. Schematic diagram of a typical OEET. Image from ref. ³.

Depending on the nature of the polymer, application of a drain, V_d , and a gate potential, V_g , induces both ion flow from the electrolyte into the polymer and charge injection or extraction at the channel *via* the source or drain electrode. The left panel in **Figure 1.2** depicts that an initially neutral conjugated polymer produces little to no drain current, I_d , at zero gate bias, and the device is in the “OFF” state. Sufficient increase of the gate potential can effectively oxidize (p-type doping) or reduce (n-type doping) the polymer by injecting holes (p-type charge carrier) or electrons (n-type charge carrier) which are stabilized in a charge balancing process by the simultaneous injection of counter-ions from the surrounding electrolyte. This leads to an increase of the channel conductivity and increase of I_d , switching the device to the “ON” state. Such OEET behavior is characterized as “accumulation mode” operation. On the other hand, as shown in the right panel of **Figure**

1.2, an intrinsically conducting polymeric channel, essentially a self-doped conjugated polymer with already existing charges stabilized within the bulk material, will be in the “ON” state and show appreciable drain currents at zero gate bias. Upon increasing the gate potential, ions drift from the electrolyte to the channel and electrostatically interact with the counterions inherent to the polymer. This consequently destabilizes and extracts the charge carriers (holes or electrons) along the polymer backbone, which effectively de-dopes the material. Eventually the channel loses its conductivity and the OECT switches to the “OFF” state, a behavior characterized as “depletion mode” operation. In either mode of operation, the change in drain current measured with gate voltage, $\left(\frac{\partial I_d}{\partial V_g}\right)$, yields the transconductance (g_m), which describes the transduction performance of devices and serves as the figure-of-merit for transistors.

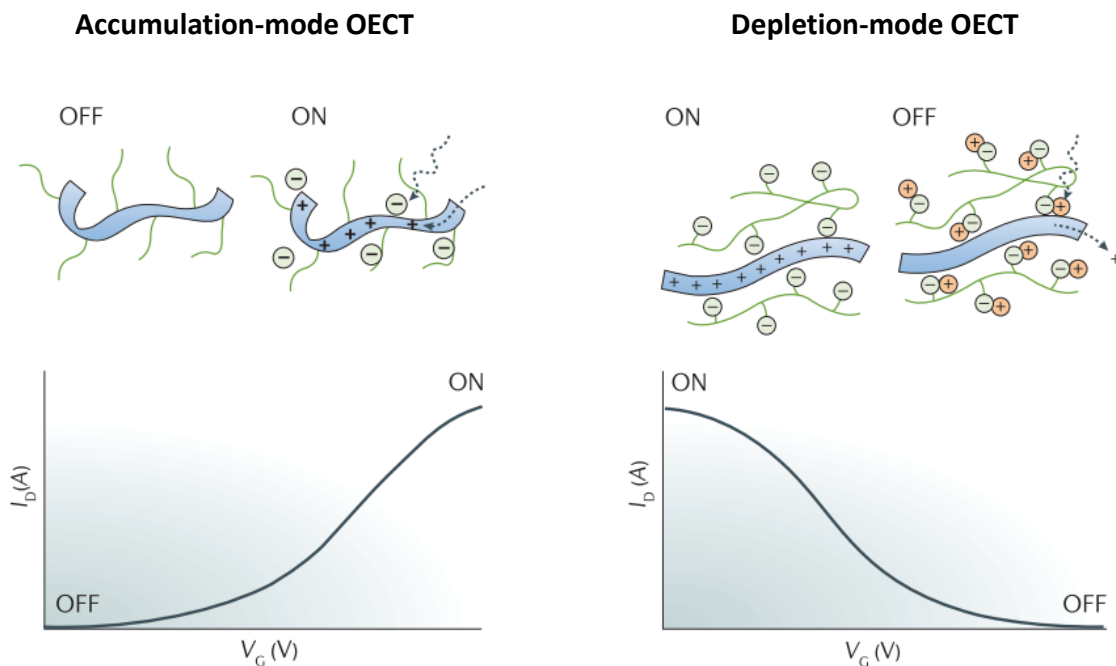


Figure 1.2. Graphical representations elucidating the processes involved in the polymeric channel material for accumulation and depletion mode OECTs (top), as well as the general profiles of the drain current that can be expected during application of a gate potential sweep from each device mode (bottom). Image from ref³.

Bulk doping processes in the OECT channel, owing to the electrochemical properties and soft nature of the conjugated polymer as well as the presence of mobile ions in the electrolyte, is the defining characteristic of OECTs that distinguishes them from other closely related organic transistors such as organic field effect transistors (OFET) and even electrolyte gated OFETs (EGOFETs). In the latter two devices, application of gate bias induces field-effect doping of the semiconducting polymer, that is, the accumulation of charge at the polymer-dielectric (in OFETs) or polymer-electrolyte (in EGOFETs) interface, whose architectures and charging behavior are depicted in **Figure 1.3**. Consequently, the amount of charge and the drain currents induced by device operation is limited by the area of these interfaces. Contrastingly, bulk doping in OECTs results to greater charge build up in the channel and significantly higher drain currents. Indeed, OFETs show capacitances of roughly $10^{-9} - 10^{-6} \text{ F cm}^{-2}$ regardless of semiconductor thickness,^{4,5} while an OECT comprising a 130-nm thick PEDOT:PSS channel, for example, can show up to $5 \times 10^{-4} \text{ F cm}^{-2}$.⁶ Thus, in describing the OECT device physics, a bulk capacitance term is used.

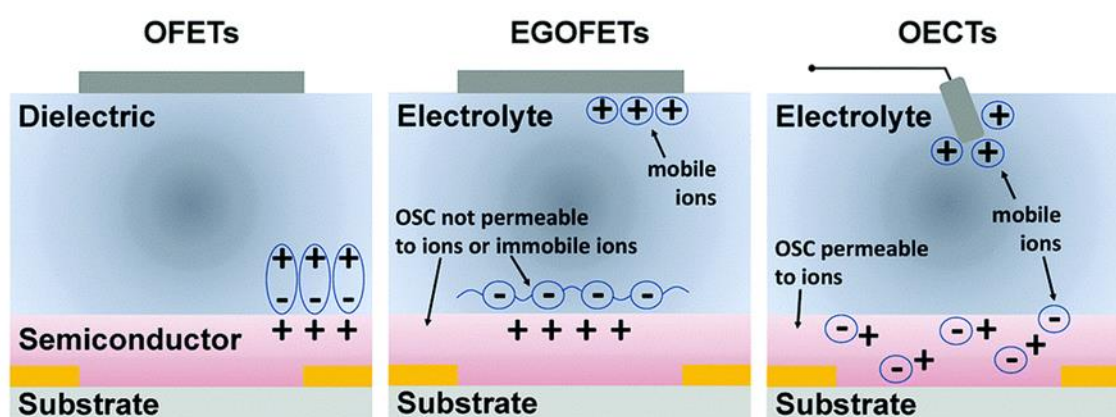


Figure 1.3. Differences between the architectures and charging behaviors of OFETs (left), EGOFETs (middle), and OECTs (right) upon application of gate potential. Here, OSC stands for “organic semiconductor”. Image from ref. ⁷.

1.2.2. Physical model of OECTs

Despite the increasing variety of polymers that have been employed in OECTs over recent years, which will be discussed in a following section (**1.4 Progress in mixed conducting polymer design**), substantial research on the behavior of OECTs and their applications have been made based on PEDOT:PSS as the active channel material owing to its potential to yield high conductivities, high stability, and commercial availability in aqueous solutions. As such, the most prominent models conceptualized to describe OECT device physics focuses on depletion mode operation with p-type materials, however similar principles may also be generalized to accumulation mode devices and n-type channel materials to extract important material-specific parameters.

The Bernards-Malliaras model describes the behavior of depletion mode OECTs by dividing the OECT into an electronic circuit, accounting for hole transport in the polymeric channel, and an ionic circuit, representing ion transport across the electrolyte, as shown in **Figure 1.4**.⁸

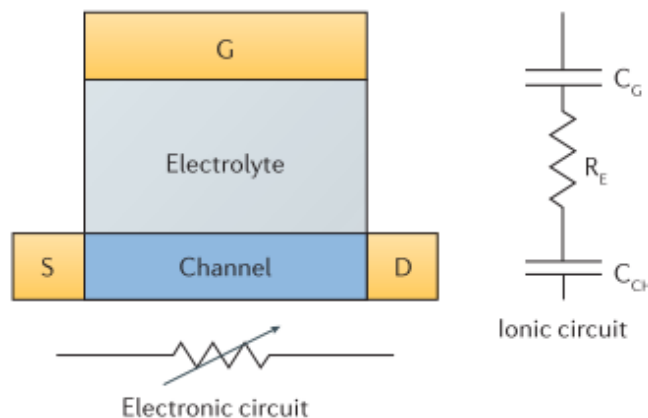


Figure 1.4. Electric circuit models used to describe the ionic and electronic parts of OECTs in the Bernards-Malliaras model. Image from ref. ³.

1.2.2.1. Steady-state characteristics

The electronic circuit is described by Ohm's law and the ionic circuit is treated as an ideal polarizable electrode, exhibiting the same behavior as a charging capacitor. Furthermore, the channel is considered to be a volumetric capacitor, rather than an interfacial one. This makes it possible to obtain the equation of the drain current at saturation ($I_{d,sat}$) given in **Equation 1.1**.⁶

$$I_{d,sat} = \frac{Wd}{2L} \mu C^* (V_t - V_g)^2 \quad 1.1$$

Where W , d , and L are the channel width, thickness, and length, respectively, μ is the channel charge carrier mobility ($\text{cm}^2 \text{V}^{-1} \text{s}^{-1}$), C^* is the volumetric capacitance (in F cm^{-3}) and V_t is the threshold voltage. Note that this equation is almost the same as that derived for MOSFETs⁹, except that the areal capacitance term (C') is replaced by the C^* term for OECTs. The drain current at saturation is independent of the drain voltage, which simplifies subsequent derivation of performance parameters.

The transconductance (g_m), which quantifies the transduction performance of the transistor, is experimentally obtained by measuring the change in drain currents over the change in gate voltage from differentiating the transfer curves (I_d versus V_g) of OECTs.³ We can also predict trends in g_m by taking the first derivative of **Equation 1.1** with respect to V_g to yield the description of the OECT transconductance at saturation, shown in **Equation 1.2**.⁶

$$g_m = \frac{Wd}{L} \mu C^* |V_t - V_g| \quad 1.2$$

1.2.2.2. Transient characteristics

The transient drain current in OECTs upon application of a constant gate voltage can be understood as the outcome of two major events occurring in the device: the charging behavior of the ionic circuit measured at the gate current (I_g) and the injection or extraction of holes or electrons at the channel effectively changing its conductivity.^{8,10} Assuming a constant average ionic current and hole density in the device, no saturation effects, and (de)doping occurring throughout the whole film, the transient response of the drain current can be described by **Equation 1.3**.

$$I_d(t, V_g) = I_{SS}(V_g) + \Delta I_{SS} \left(1 - f \frac{\tau_e}{\tau_i}\right) e^{-\left(\frac{t}{\tau_i}\right)} \quad \mathbf{1.3}$$

Where I_{SS} is the steady state drain current obtained at saturation, ΔI_{SS} is the total change in the drain current resulting from stepping V_g from zero to a certain bias, f is a geometrical factor defining the fraction of the ionic current measured at the drain, τ_e is the electron (or hole) transport time constant, and τ_i is the ionic transport time constant. Essentially there are three contributing terms to the total current transient: the drain current at saturation, the change in current due to conductance changes upon doping or de-doping the polymer, and a fraction of the gate current flowing into the channel, which can be understood to be split between the source and drain to account for the spatial non-uniformity of the doping or de-doping process across the channel. For simplicity, f can be made equal to 0.5 (equal division of the gate current at the source and drain)¹¹, however variations of the model define more accurate values of f by assuming its dependence on both the gate and drain voltages^{10,12}, for instance by extracting f from multi-parameter fits to experimental data or directly measuring the ratio of the gate and drain currents. Additionally, the exponential form in **Equation 1.3** implies that the time constant extracted from I_d transients is determined by the ionic time constant τ_i , suggesting that the overall response speed in an OECT is limited by the rate of ion injection into the channel.

Another operating condition that provides useful information about the device physics and channel material properties is the measurement of the transient drain current upon application of a constant gate current. This fixes the kinetics of the ionic circuit and focuses on the electronic transport behavior in the device. The transient behavior at constant I_g derived from the Bernards-Malliaras model is given in **Equation 1.4**.

$$I(t, I_g) = I_0 - I_g \left(f + \frac{t}{\tau_e} \right) \quad 1.4$$

Where I_0 is the initial drain current prior to application of I_g . τ_e measures the time it takes for the charge carriers to drift across the source and drain under an applied potential, and is related to their mobility (μ_e) by $\tau_e = L^2 (\mu_e V_d)^{-1}$.¹³ Thus, plotting the slope of the transient drain current $\left(\frac{\partial I_d}{\partial t} \right)$ versus I_g allows extraction of τ_e from the inverse of the slope, subsequently allowing calculation of μ_e for the active channel material. For example, the hole mobility for PEDOT:PSS extracted from OECT measurements, $\mu_{OECT} = 2.7 \text{ cm}^2 \text{ V}^{-1} \text{ s}^{-1}$, shows reasonable agreement with those obtained from Hall effect measurements, $\mu_H \approx 1\text{-}3 \text{ cm}^2 \text{ V}^{-1} \text{ s}^{-1}$,^{14,15} which gives some validation of the OECT method to extract hole mobilities. This is especially useful as an alternative tool to characterize semiconducting polymers that show unintentional bulk doping behavior, which can interfere with the stability of measurements in typical OFET configuration for hole mobility determination.¹⁶

1.2.3. Influence of channel geometry on OECT performance

Equations 1.1 and **1.2** imply that the magnitude of the OECT I_d and g_m scale with the channel thickness (d), unlike that of FETs, and reiterates the bulk doping phenomenon unique to OECT behavior. Furthermore, **Equation 1.2** allows the extraction of the μC^* parameter from the values of g_m measured for several devices composed of different channel dimensions. The left-most panel of **Figure 1.5** shows the g_m scaling of devices over

different channel geometry and bias, $WdL^{-1}|V_T-V_G|$, for several types of OECT channel materials reported in literature. The slope of each plot gives the μC^* product (marked $[\mu C^*]_{\text{OECT}}$ in **Figure 1.5**). The values almost directly agree with the products of individually extracted μ , from electron transit times in OECTs, and C^* , from equivalent circuit modelling of the impedance, in a 1:1 fashion, as shown in the middle panel of **Figure 1.5**. Since the terms μ and C^* capture the electronic transport properties and ionic charging behavior of the channel material, respectively, and are independent of the device dimensions and operating conditions, the μC^* product serves as the material-system figure-of-merit to benchmark OECT channel materials.¹⁷ Plots of μ_{OECT} versus C^* such as that given in the right-most panel of **Figure 1.5** provide a quick summary of the relative performance of different OECT materials, the optimum region being on the northeast part of the graph.

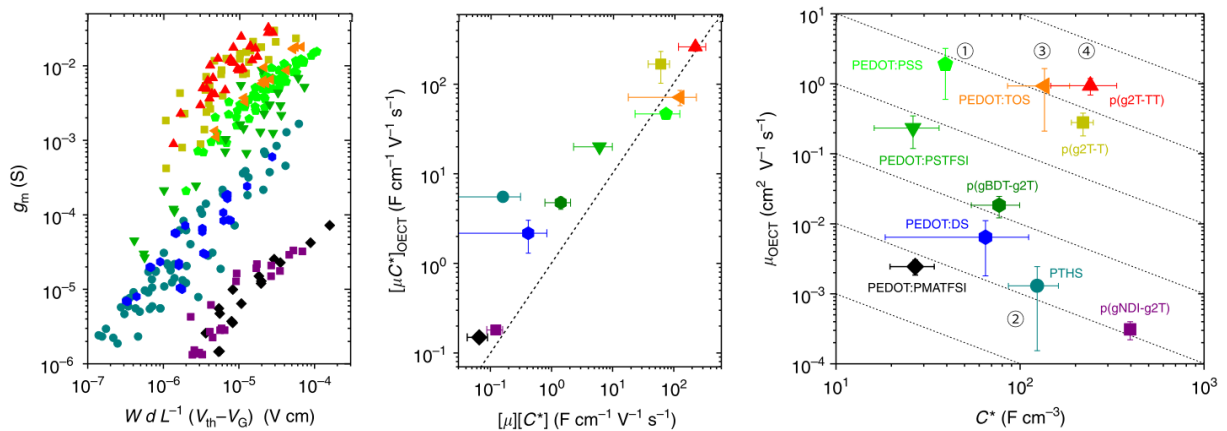


Figure 1.5. Scaling of g_m with OECT channel dimensions and bias, $WdL^{-1}|V_T-V_G|$ (left), whose slope, $[\mu C^*]_{\text{OECT}}$, is plotted against the product of individually obtained values of μ and C^* (middle) showing almost 1:1 agreement (dashed line), and a $\mu_{\text{OECT}}-C^*$ map of different OECT channel materials as labelled (right). Dotted lines indicate constant μC^* . The same color coding and shape is used for each channel material across all panels.

Figures from ref. ¹⁷.

According to **Equation 1.3**, the response time of an OECT upon application of a step gate potential is the time constant, $\tau_i = R_S C$, of the ionic circuit across the electrolyte and channel (refer to Figure 1.4). Using impedance spectroscopy, the solution resistance, R_S , and the channel capacitance, C , can be measured for devices with various channel dimensions. The C in OECTs of PEDOT:PSS has been shown to be proportional with WdL over a wide range of channel volumes, the slope of which can be used to extract the volumetric capacitance (C^*), about 40 F cm^{-3} for PEDOT:PSS.⁶ On the other hand, the solution resistance is inversely proportional with the area of the electrode in a simple electrochemical cell such as the one used to model the OECT ionic circuit. Indeed, R_S in PEDOT:PSS electrodes have been shown to scale linearly with $(WL)^{-1/2}$.¹⁸ Combining the scaling laws of C_{CH} and R_E yields $\tau_i = R_E C_{CH} \propto d(WL)^{1/2}$, which states that the response time of OECTs is proportional with channel size. This implies that thinner films may lead to faster devices but at the expense of the transduction performance. Therefore, the channel geometry should be tuned according to the requirements of intended applications.

The scaling laws derived from the basic model of OECTs discussed above provide practical implications for the design of devices and the active channel material, however certain conditions may cause real devices to deviate from these predictions. For instance, the capacitance only scales linearly with the channel volume if devices are operated such that enough time is given for the ions to penetrate completely throughout the bulk of the material. Above a characteristic frequency, $f_{ion} \approx \mu_{ion} V d^2$, that depends on the ion mobility (μ_{ion}), devices will show sublinear dependence of the capacitance with channel volume. At even higher frequencies devices eventually perform similar to OFETs. Additional effects that may result from either the specific device architecture (ex. overlapping electrodes¹⁹) or even functionalized devices (ex. blocking membranes¹⁰), will also be a factor in the final response times and transconductances. The Bernard-Malliaras model can be adapted and extended further with parameters that account for such effects to improve the accuracy in predicting OECT measurements.

1.3. Key features of mixed ionic-electronic conducting polymers

According to our understanding of the basic operating principles and device physics of OECTs discussed in the previous section, we can identify some key features of mixed ionic-electronic conducting polymers. First, the conductance state of the material must be electrochemically controllable. This is possible with conjugated polymers due to their unique semiconducting properties arising from their electronic structure. As will be discussed, the incorporation of ions in the polymer supports charge carrier formation and is therefore necessary to modulate its electronic conductivity. Consequently, efficient transport of ions in the material is important for fast device operation. The presence of ions can also lead to electrostatic interactions that may contribute to the high volumetric capacitance of these materials, which is relevant for high-transconductance OECTs. High OECT performance also relies on high charge carrier mobility, which is dependent on complex charge transport mechanisms occurring in conjugated polymers due to their inherently disordered structure.

1.3.1. Semiconducting behavior of conjugated polymers

The unique semiconducting behavior of conjugated polymers arises due to the electronic structure of their backbone.^{20,21} The carbon atoms of a conjugated polymer chain are sp^2 hybridized, each sharing three σ -bonds with neighboring atoms *via* the sp^2 hybridized orbitals and π -bonds with adjacent sp^2 hybridized carbons *via* the non-hybridized p_z orbitals, depicted in **Figure 1.6** (top).

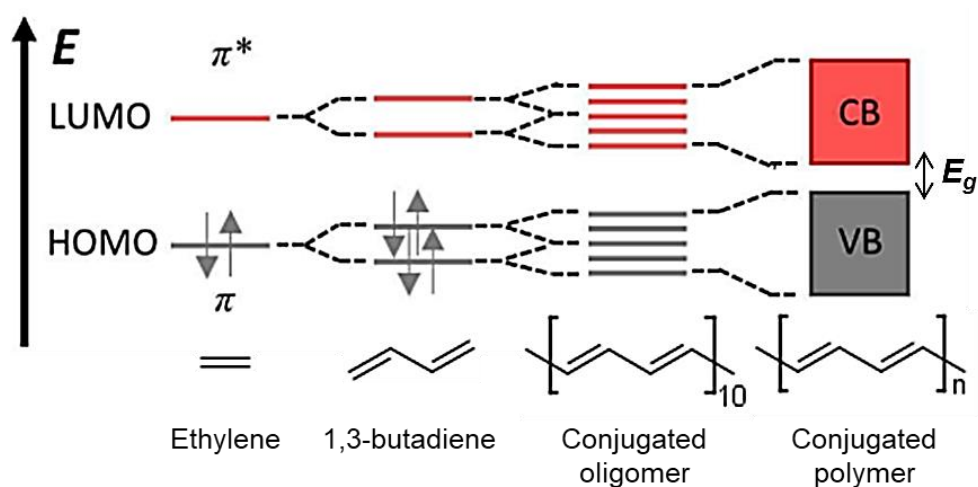
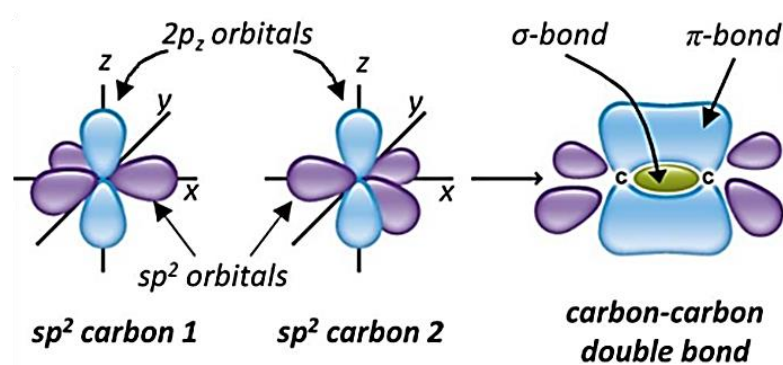


Figure 1.6. Illustration depicting the general electronic structure of double-bonded carbon atoms (top) and energy diagram of the frontier orbitals of conjugated carbon chains with increasing length (bottom). Adapted from ref. ²².

The linear combination of the non-hybridized p_z orbitals results in bonding (π) and antibonding (π^*) states that form the highest occupied molecular orbital (HOMO) and lowest unoccupied molecular orbital (LUMO), respectively (**Figure 1.6**, bottom). The energy difference between the HOMO and the LUMO can be understood as the organic equivalent of the semiconductor band gap, E_g . In ethylene, the simplest alkene, the energy between the HOMO and LUMO is 7.6 eV, which is too large for it to be considered a semiconductor (assuming around $E_g \leq 4$ eV for semiconductors). Increasing the carbon chain length to form conjugated oligomers and polymers increases the density of π and π^* energy levels,

which then approach continuous band-like energy distributions and lead to narrowing of E_g . At the limit of infinitely long conjugated polymers, a minimum energy gap persists owing to dimerization of the carbon atoms in the form of alternating single and double bonds (*i.e.*, alternating bond lengths) along the carbon chain. This occurrence can be understood as a Peierls distortion;^{23,24} dimerization changes the lattice periodicity and induces a band gap at which the energy of the HOMO is lowered and the energy of the LUMO is increased. As a result, the ground state electronic structure of conjugated polymers is semiconducting. Thus, to induce electronic conductivity in conjugated polymers, mobile charge carriers must first be formed by doping.

1.3.2. Doping conjugated polymers

Like inorganic semiconductors, polymeric (organic) semiconductors may be *p*- ("positive" charge carriers) or *n*-type ("negative" charge carriers) doped. However, unlike inorganic semiconductors in which their doping involves introducing impurity atoms in the crystal lattice to donate electrons or holes as free charge carriers, doping polymeric semiconductors typically involves redox reactions.²⁵ Such reactions only involve electrons from the non-hybridized p_z orbitals, while the sp^2 electrons maintain the structure of the polymer chain.

P-type doping of a conjugated polymer (P) involves its partial oxidation ($P^0 + A \rightarrow P^+A^-$). This may be accomplished either chemically, in the presence of a strong electron acceptor, or electrochemically, by application of a positive potential against a counter electrode in the presence of electrolytes. Similarly, *n*-type doping of a conjugated polymer involves its partial reduction ($P^0 + A \rightarrow P^-A^+$) to form a negative charge on the backbone either by chemical reaction with an electron donor or by application of a negative potential in an electrochemical cell. Charge neutrality is maintained in the doped polymer by

interactions with counterions (A^- or A^+), which may originate from the dopant molecule or supporting electrolyte. Additionally, unlike chemical doping, electrochemical doping allows precise control of intermediate doping levels in conjugated polymers depending on the voltage applied. This particular feature is exploited in OECTs and other related devices.

Doping conjugated polymers, either by oxidation (loss of an electron) or reduction (gain of an electron), results in a radical ionic species called a “polaron”.^{26,27} This may be positively or negatively charged with spin $\frac{1}{2}$. The polaron is stabilized by delocalization over a few monomer units and by polarization of the surrounding environment. Several polarons can be formed in a long polymer chain. At high dopant concentrations, or in the case of confinement due to chain defects, polarons may combine by pairing of their radicals to form a spinless charged species with twice the charge. This species is called a “bipolaron” and may be positive or negative depending on the type of doping. Such polarons and bipolarons are the charge carriers in conducting polymers. A depiction of a positive polaron and bipolaron in a polythiophene is given in **Figure 1.7**.

Polaron and bipolaron formation affect the chemistry and geometry of the backbone. For instance, in conjugated polymers with aromatic backbones such as the polythiophene illustrated in **Figure 1.7**, polaron formation induces a structural transition from a benzenoid-type to a planar quinoid-type (shaded in gray).²⁶ This impacts the electronic structure of the polymer by the formation of localized energy states within the initial bandgap as shown in **Figure 1.8**. Positive polarons and bipolarons provide holes in localized electronic states near the valence band, while negative polarons and bipolarons provide electrons in energy levels near the conduction band. As a result, lower energy electronic transitions may occur, which is reflected by measurable changes in the optoelectronic behavior of the material. This is exploited in applications of electrochromic display devices,²⁸ and can also be used to track doping of the polymer through practical methods such as spectroelectrochemistry (employed in this work, see section **3.3.2 Spectroelectrochemistry**).

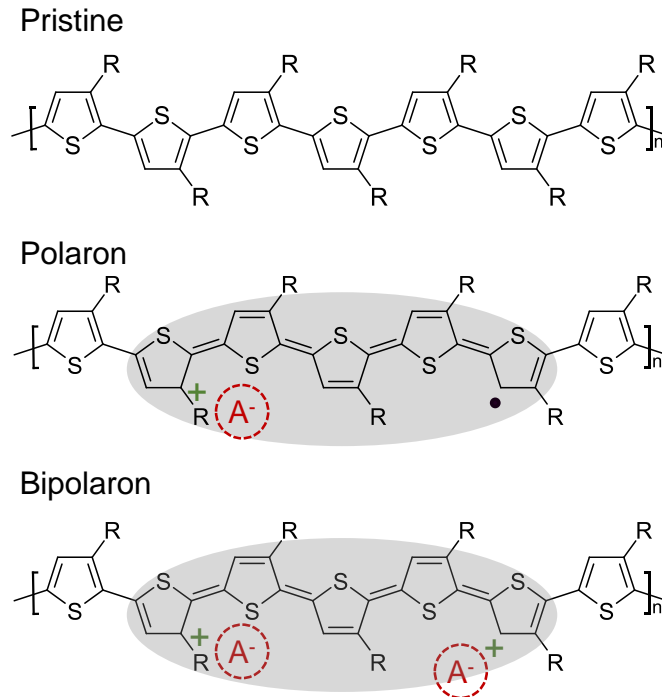


Figure 1.7. The structures of a neutral polythiophene and its polarons and bipolarons upon p-type doping. Charge neutrality is maintained by interaction with counterions (encircled by a red dashed line).

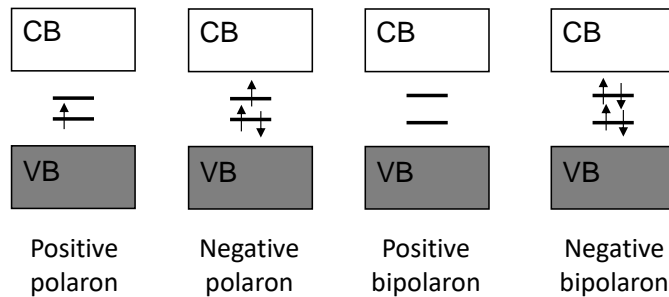


Figure 1.8. Simplified energy diagram depicting the localized energy levels within the band gap of an initially neutral polymer induced by polaron and bipolaron formation.

1.3.3. Ionic transport in mixed conducting polymers

Electrochemical doping of conjugated polymers to generate polarons necessitates counterions to maintain charge neutrality. This implies that the formation of electronic carriers is coupled with the transport of ions in these materials, which subsequently affects the performance and response speed of their electrochemical devices. For these reasons, the design of mixed conducting polymers as active materials for OECTs over recent years have involved modifying conjugated polymers to better accommodate ion transport, especially from an external electrolyte. As a starting point to understand how ionic conductivity can be enhanced in conjugated polymers, we first recall some basic notions about ion transport in polymer electrolytes.

One possible mechanism of ion transport in dry solid state polymer electrolytes involves ion motion coupled with the segmental motion of polymer chains.^{29,30} **Figure 1.9** depicts how segmental motion can facilitate ion “hopping” between different sites in a single polymer chain (intrachain ion hopping) or between sites of adjacent chains (interchain ion hopping). This implies that an amorphous rubbery polymer matrix that has more segmental motion is most favorable to support ion mobility. Substitution of ion-coordinating moieties such as nitrogen or oxygen atoms on the polymer chain can further impact ion transport.³¹ Ultimately, however, the mobility of the ions is limited by the polymer mobility.



Figure 1.9. Illustration of ion transport in polymer matrices involving intra- and interchain ion hopping assisted by segmental motions of polymer chains. Ion-coordinating moieties along the chains are represented by open circles. Image from ref. ³².

To enhance ion diffusion in polymers, attempts have been made to decouple ion motion from polymer chain motion.³³ One approach is to graft ion-coordinating moieties like polar or ion-terminated sidechains to distance the ions from the polymer backbone. For example, polymethyl methacrylates grafted with longer ethylene glycol sidechains show better ionic conductivities than their counterparts comprising shorter substituents.³⁴ Another approach is to dilute the polymer chain density surrounding the ions by solvent-induced swelling of the polymer, resulting in a gel.³⁵ This allows fast ion diffusion to occur through the mostly liquid phases.

For mixed conducting polymers that are exposed to aqueous electrolytes when operated in electrochemical devices, the swelling ability of the polymer seems to be one major factor of efficient ion injection. For instance, results from electrochemical strain microscopy (ESM) of semicrystalline P3HT operated with a DC offset bias and aqueous electrolyte (20 mM KCl), in combination with amplitude-modulation/frequency-modulation (AM-FM) viscoelastic mapping, provides some evidence of heterogeneous swelling of the polymer due to non-uniform ion penetration in the film favoring the softer amorphous phases over the stiffer ordered phases.³⁶ Crosslinking of PEDOT:PSS has also been shown to decrease the ion drift mobility extracted from electrochromic moving front experiments, which suggests that decreasing the swelling ability of the polymer results in slower ion uptake.³⁷ Furthermore, substituting conjugated polymers with hydrophilic, ion-coordinating sidechains (*e.g.*, oligo(ethylene glycol) sidechains) can induce passive (without bias) swelling and expansion of the crystal lattice of semicrystalline polymers upon exposure to aqueous electrolyte.³⁸ As a result, ions can readily access polaron sites upon application of bias leading to much faster doping kinetics than their non-substituted counterparts. In fact, chemical modification of various p-type and n-type conjugated polymers with ethylene glycol sidechains has been a successful approach to yield mixed conducting polymers exhibiting high OECT performance (discussed more in section **1.4 Progress in mixed conducting polymer design**).^{39,40}

One issue that arises due to hydration-induced swelling is excessive water uptake that can eventually degrade the mixed conducting properties and structural integrity of the film. For instance, it has been shown in electrochemical quartz crystal microbalance with dissipation (EQCM-D) measurements of P(g2T-TT), a polythiophene functionalized with ethylene glycol sidechains, that the injection of ions with large hydration spheres (high number of water molecules) can actually slow down the response speed of OECTs.⁴¹ Also, QCM and spectroelectrochemical measurements of an n-type mixed conducting polymer functionalized with ethylene glycol sidechains show that excessive swelling in polymer electrodes leads to irreversible mass changes.⁴² This results in irreproducible doping behavior and deterioration of OECT performance, as well as disintegration of the film during continuous cycling operation, illustrated in **Figure 1.10**.

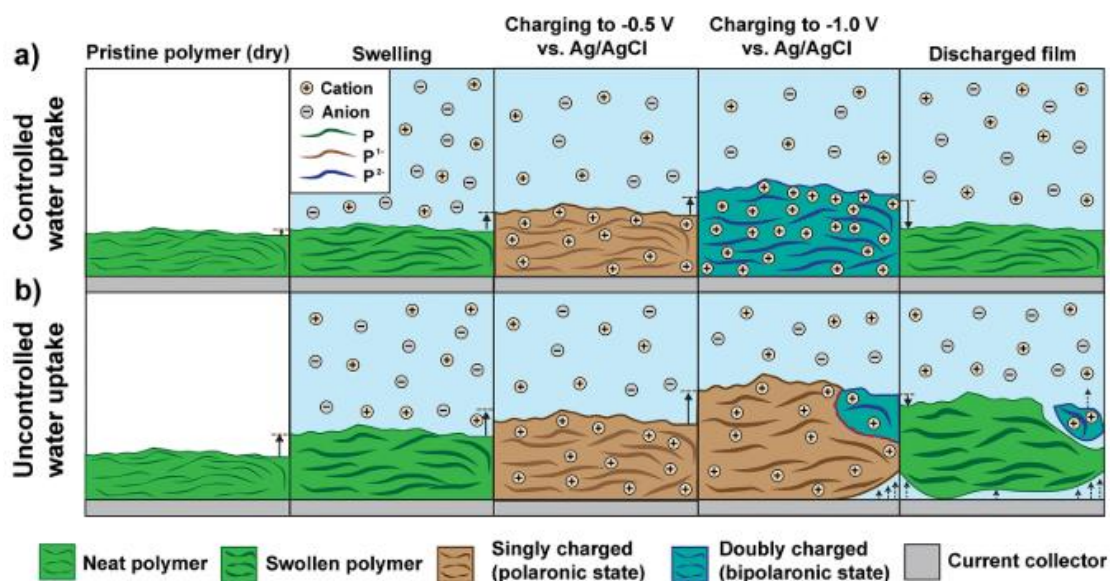


Figure 1.10. Illustration of the charging mechanism of ethylene glycol-substituted n-type mixed conducting polymer electrodes operating in aqueous electrolyte. For polymers with mixed hydrophilic and hydrophobic sidechains, water uptake is limited (“controlled”) leading to reversible swelling and charging behavior (top). For polymers that are completely functionalized with hydrophilic sidechains, excessive water uptake (“uncontrolled”) can lead to irreversible mass changes and material disintegration.

Schematic from ref. ⁴².

1.3.4. Volumetric capacitance in mixed conducting polymers

Another consequence of incorporating ions in the bulk of conjugated polymer films is that they may interact electrostatically with oppositely charged species present in the polymer material, which may either be the counterions in conducting polymer electrolytes (e.g., sulfonate anion in PEDOT:PSS upon hole extraction) or the charge carriers formed upon doping conjugated polymers. This interaction is identified as the origin of the large volumetric capacitances in mixed conducting polymers. The concept was initially introduced to explain the charging behavior of depletion-type PEDOT:PSS electrodes that exhibit ideal volume-dependent capacitance.^{6,43} Since then, C^* has been adapted as a practical indicator of ion-electron coupling in both depletion- and accumulation-type mixed conducting polymers, and can be extracted from equivalent circuit model fits to the experimental impedance spectra of films of various thicknesses (employed in this work, see section **3.3.3.1 Equivalent circuit model-fitting**), among other methods.

A simplified understanding on how C^* arises in PEDOT:PSS involves an electronic double layer (EDL) model of the interaction of injected hydrated ions with the sulfonate ions in PSS.⁴⁴ This layer forms a capacitor (C'_{DL}) with a thickness (t) defined by the distance between the center of the injected ion and the polymer chain, depicted in the left panel of **Figure 1.11**. Additionally, there exists several charged “sites” separated by a distance α at which double layers may form. The density of these sites corresponds to the charge carrier density in the polymer. This picture can be further simplified as shown in the right panel of **Figure 1.11** by depicting the charged polymer segments as parallel plates separated by a distance α throughout the film volume (with width W , length L , and thickness, d). Thus, C^* is the sum of contributions from the double layer capacitors, $C^* = C'_{DL}/\alpha$, which implies a direct correlation between C^* and maximum charge carrier density, assuming all sites are accessible to penetrating ions.

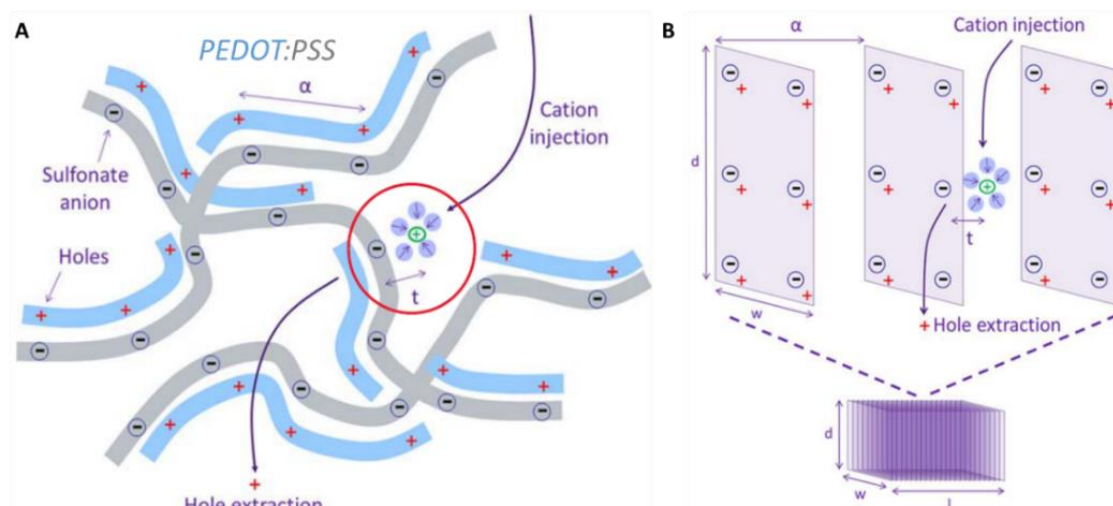


Figure 1.11. Illustration of double layers formed between injected cations and sulfonate anions in PEDOT:PSS upon hole extraction (left). Simplified illustration of double layer capacitances in PEDOT:PSS as a block of parallel plate capacitors (right).⁴⁴

1.3.5. Electronic charge transport in conjugated polymers

The performance of an OECT can be further enhanced by improving the charge carrier mobility of the mixed conducting polymer channel. However, designing polymers to improve their electronic mobilities remains a difficult task due to the complexity of charge carrier transport in these materials, which originates from their inherent disordered nature.^{45,46} Since conjugated polymers are “soft” materials bonded by weak van der Waals interactions, they have numerous degrees of conformational freedom that can result in microstructures ranging from almost completely amorphous to semicrystalline. Consequently, transport mechanisms involve multiple processes occurring at different length scales. The most efficient pathway for charge transport in polymers is by polaron delocalization along an extended conjugated segment in the backbone (intrachain transport). However, charges will eventually encounter obstacles from conformational defects, kinks and chain-ends that are associated with localized energy states and act as electronic traps. Thus, for charge transport to proceed over more practical dimensions,

charges must “hop” across a series of localized states *via* thermally assisted quantum-mechanical tunneling. This allows charges to move along close contact points (*i.e.*, stacked aggregates) between adjacent chains (interchain hopping). To demonstrate, **Figure 1.12** depicts the intra- and interchain charge transport pathways in semicrystalline polymers such as P3HT and PBTTT that typically exhibit edge-on packing motifs. The most relevant directions for charge transport are along the backbone and π -stacks, while less efficient hopping along the lamellar-stack may also occur. Compared to delocalization, hopping transport is much slower and therefore limits the macroscopic conductivity of semiconducting polymers

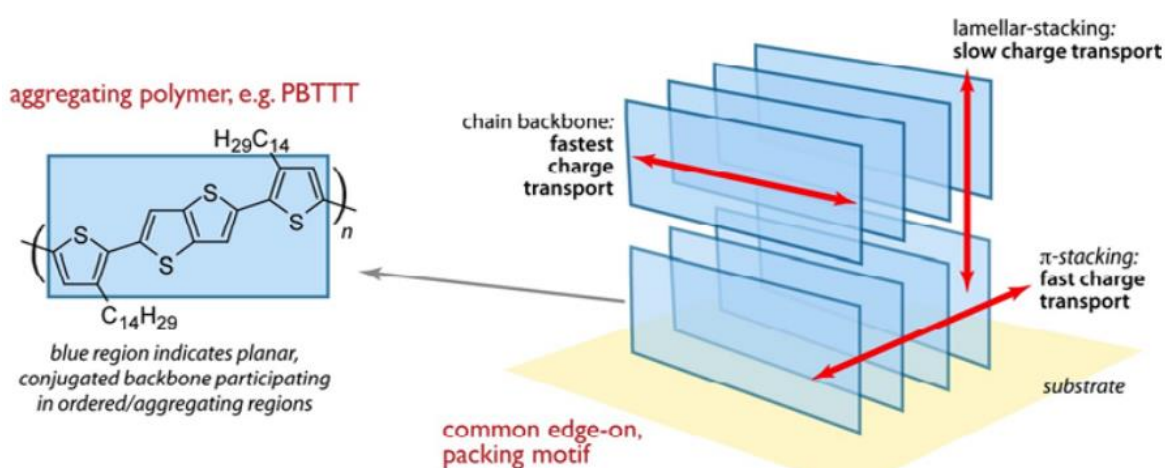


Figure 1.12. Charge transport in semicrystalline polymers (PBTTT exhibiting edge-on packing given for example) occurs along the polymer backbone (intrachain transport) and along the π -stack and lamella-stack directions (interchain transport). Image from ref. ⁴⁵.

Macroscopic charge transport in flexible chain conjugated polymers occurs through percolation pathways along crystallites interconnected by tie chains, depicted by the red highlighted line in the left panel of **Figure 1.13**.^{45,46} Charge transport remains confined within the ordered regions of the material owing to the large energy barriers that must be overcome for charges to cross between ordered and amorphous phases.⁴⁵ Also, polymer chains in the

ordered regions have longer conjugation lengths and increased intermolecular coupling that can support charge transport. Meanwhile, high activation energies are needed for charge transport to occur in fully amorphous materials that do not show molecular aggregation behavior (right panel of **Figure 1.13**), making these materials inefficient electronic conductors. Increasing the molecular weight of polymers can increase the probability of tie chains and enhance charge mobility, but only to a certain extent. For P3HT, it has been estimated that only 10^{-3} of all chains need to form tie chains to support macroscopic charge transport, above which mobility is independent of tie chain fraction.⁴⁷ Also, charge mobility has been shown to be independent of molecular weight in flexible conjugated polymers at a molecular weight greater than the critical entanglement molecular weight (M_c). For instance, the field-effect mobility of P3HT saturates to about $0.02 \text{ cm}^2 \text{ V}^{-1} \text{ s}^{-1}$ at a molecular weight greater than $M_c \approx 25\text{-}35 \text{ kg mol}^{-1}$.⁴⁸ In this case, charge mobility can be enhanced further under certain solidification conditions (e.g., high pressure or strain) that lead to chain-extended structures.

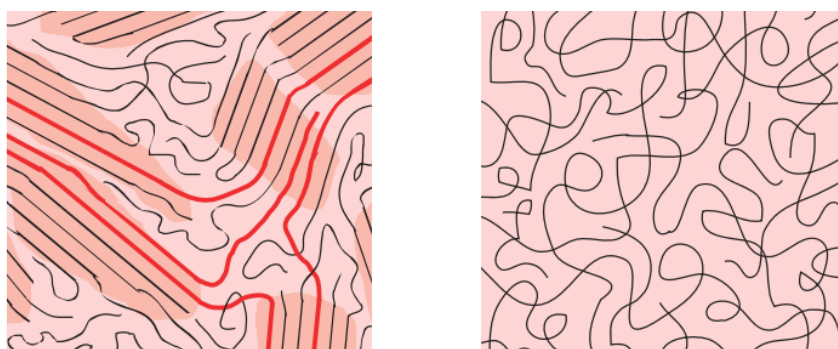


Figure 1.13. Schematics depicting the microstructures of semicrystalline (left) and completely amorphous (right) flexible chain polymers. Note coexistence of ordered (darker shade) and amorphous regions. Long polymer chains connecting ordered regions are highlighted in red.

In mixed conducting polymers operating in electrochemical devices, increasing the charge carrier concentration by doping impacts the charge transport behavior. A simplified explanation can be given according to charge transport models for disordered semiconductor materials such as conjugated polymers.⁴⁹ Charge hopping rates depend on the distances between localized carrier sites and their relative energies, which can be described by a Gaussian distribution of the electronic states (density of states, DOS) in energy space, depicted in **Figure 1.14**. At low charge carrier concentrations, the carriers only populate sparsely packed energy states, which leads to slow hopping. As the carrier concentration is increased by doping, carriers fill higher energy states that are more densely packed. Thus, hopping between sites becomes faster, resulting in higher charge-carrier mobilities. Models that incorporate carrier-concentration-dependent mobilities describe reasonably well the non-monotonic increase of the transconductance with applied gate voltage in OECTs.^{50,51}

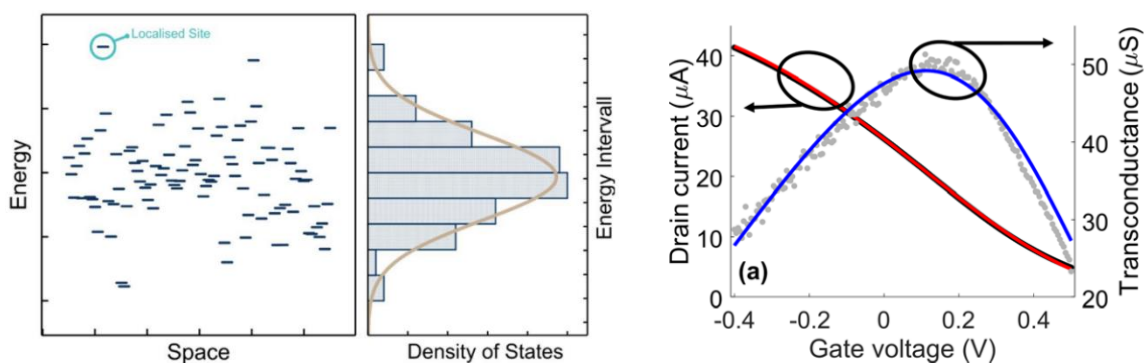


Figure 1.14. Map of the distribution of localized sites, as indicated, over space and energy according to a Gaussian distribution of the density of states (DOS) of a disordered semiconductor (left panel, from ref. ⁵²). Disorder model fit (solid blue line) to the experimental transconductance (grey scatter plot) of a P(g2T-TT)-based OECT (right panel, from ref. ⁵⁰). Predicted drain current (solid red line) from disorder model and experimental drain current (black scatter plot) also shown.

1.4. Progress in mixed conducting polymer design

Several publications over the years have already demonstrated mixed ionic-electronic conducting polymers as promising high performance materials for bioelectronics.^{2,53,54} In particular, PEDOT:PSS, a mixed conductor comprising a conjugated polymer (PEDOT) copolymerized with a polyelectrolyte (PSS), has been one of the most researched materials for such applications and for understanding OECT device physics due to its high conductivity (reaching up to 5000 S cm^{-1} with acid post-treatment),^{55,56} biocompatibility,⁵⁷ and commercial availability in aqueous solutions.⁵⁸ However, there are certain issues in using PEDOT:PSS. One is the acidity of the PSS chain, which can lead to degradation of devices,⁵⁹ incompatible interfaces with biological species at physiological pH,⁶⁰ as well as corrosion of industrial equipment like common inkjet print heads.⁶¹ The latter would negate the advantages of an aqueous polymer dispersion for roll-to-roll mass production of devices. Additionally, since PEDOT:PSS is intrinsically doped, its OECTs operate only in depletion mode. This can be impractical for several applications and would also require constant voltage input to maintain devices in the “off” state. Usually up to 0.8 V must be applied, which can risk parasitic side reactions with ambient water and oxygen.⁶² Furthermore, OECTs of PEDOT:PSS exhibit relatively poor long-term operational stability without specific additives or post-treatment of the film.⁶³ Thus, in the interest of developing tailored devices that can meet requirements such as different modes and polarity of operation, and good stability as bioelectronic implants, the demand for alternative materials persists. To this end, the past decade has seen much progress in the development of numerous mixed conducting polymers. Here, we discuss the different structural motifs of polymer families that have been studied in OECTs while highlighting some of the design rationale in engineering these materials. A summary of the OECT and mixed conductor performance indicators of some materials recently reported in literature and mentioned in this section are given in **Table 1.1**.

Table 1.1. OECT and mixed conductor performance indicators of some recent materials.

Polymer ^{ref}	W μm	L μm	d nm	V _t V	g _{m,max} mS	I _{on/off}	T _{on} ms	T _{off} ms	μ _{OECT} cm ² V ⁻¹ s ⁻¹	C* F cm ⁻³	μC* F cm ⁻¹ V ⁻¹ s ⁻¹
<i>P-type materials operating in accumulation mode</i>											
p(g2T2-g4T2) ⁶⁴	100	10	50	0.0	6.5	10 ⁵			1.7	190	5x10 ²
p(gDPP-T2) ⁶⁵	100	10	90	-0.5	6.3	10 ⁵			1.6	200	3x10 ²
p(g2T-TT) ³⁹	100	10	40	-0.2	5.4	10 ⁵	0.4	0.04	9.4x10 ⁻¹	240	3x10 ²
p(g2T-T) ¹⁶	100	10	100	0.0	7.9	10 ⁵	1.4		3x10 ⁻¹	200	2x10 ²
p(g3T2) ⁶⁴	100	10	80	0.0	8.9	10 ⁵			9x10 ⁻¹	160	2x10 ²
p(gDPP-TT) ⁶⁵	100	10	120	-0.5	3.1	10 ⁵			5.7x10 ⁻¹	180	1x10 ²
p(gDPP-MeOT2) ⁶⁵	100	10	80	-0.3	1.4	10 ⁴			2.8x10 ⁻¹	170	6x10 ¹
PDPP[T]2{TEG}3-MEET ⁶⁶			60	0.4	1.9	10 ³	1.9		1.3x10 ⁻¹	340	5x10 ¹
P3HHT ⁶⁷	100	10	140	-0.6	15	10 ⁵	2				4x10 ¹
p(gDTDPP-bis-EDOT) ⁶⁸	60	30	290	-0.1	0.4	10 ²	22	16	8.7x10 ⁻²	190	2x10 ¹
PDPP[T]2{TEG}-EDOT ⁶⁶			40	0.4	1.4	10 ³	1.4		8.4x10 ⁻²	170	1x10 ¹
P3MEEET ⁶⁹	100	10		-0.6					3.5x10 ⁻²	240	1x10 ¹
ProDOT(OE)-co-DMP ⁷⁰	50	50	280	-0.5	0.6	10 ⁵			6.3x10 ⁻²	110	1x10 ¹
P3MEEMT ⁶⁹	100	10		-0.7					7x10 ⁻²	160	10
PTHS + EG (5 vol%) ⁷¹	250	5	60	-0.8	2.0	10 ²	0.4		1.3x10 ⁻³	120	6
p(gBDT-g2T) ¹⁶	100	10	110	-0.3	0.5	10 ³			1x10 ⁻²	80	4
p(aDTDPP-bis-EDOT) ⁶⁸	60	30	190	-0.5	0.1	1	2700	200	9.5x10 ⁻²	20	2
p(gPyDPP-MeOT2) ⁷²	100	10	120	-0.5	0.2	10 ⁵	0.8	0.5	3x10 ⁻²	60	2
p(gDTDPP-aBT) ⁶⁸	60	30	120	-0.6	0.1	10 ²	2800	800	4.4x10 ⁻²	20	1
P3MEET ⁶⁹	100	10		-0.2					5x10 ⁻³	80	4x10 ⁻²
<i>P-type materials operating in depletion mode</i>											
PEDOT-S ⁷³	1125	75	20	0.2	16	10 ³	360	300			2x10 ²
<i>N-type materials operating in accumulation mode</i>											
BBL ⁷⁴	100	10	80	0.2	0.07	10 ⁴	5		2.1x10 ⁻³	730	2
pgNaN ⁷⁵	100	10	1500	0.3	0.2	10 ⁴	100		6.5x10 ⁻³	100	7x10 ⁻¹
p(gNDI-gT2) ⁷⁶	100	10	200	0.4	0.02	10 ³	5	5	3x10 ⁻⁴	400	2x10 ⁻¹
p(gNDI-T2) ^a "P-90" ^{a,77}	100	10	50		0.001	10 ²	40		2.4x10 ⁻⁴	200	5x10 ⁻²
p(gNDI-T2) ⁴²	100	10		0.3	0.001						4x10 ⁻²
pgNgN ⁷⁵	100	10	500	0.2	0.003	10 ³			1.9x10 ⁻⁴	240	4x10 ⁻²
p(gNDI-g3T2) ⁴²	100	10		0.3	0.001						1x10 ⁻²
<i>Multicomponent materials operating in accumulation mode</i>											
PTHS:PEDOT-S[(Oct ₂)NH ₂] ^{b,73}	39000 ^c	20	112	-0.4	15	10 ⁴	80	10			
PTHS:PEDOT-S[H] ^{b,73}	39000 ^c	20	102	0	14	10 ⁴	90	20			
PEDOT-S:PTEB-S (3:2) ^{b,78}	39000 ^c	20	55	0	12	10 ²	192	40			
P3HT:PEO ⁷⁹	1000	30	120	-0.3	0.08	10 ¹					6x10 ⁻¹
<i>Multicomponent materials operating in depletion mode</i>											
Crys-P ⁵⁵	80	20	200	< 0	19				4	100	5x10 ²
PEDOT:PSS / [EMIM][TCM] ⁸⁰	1000	100	200	0	14	10 ³	4		4	100	3x10 ²
PEDOT:PSS + EG, DBSA ^{6,14,81}	10	10	400	0	4		0.1		2	40	5x10 ¹

^aCopolymer p(NDI-T2)-co-p(gNDI-T2) with 90% fraction of p(gNDI-T2); All devices measured in aqueous electrolyte except for marked ^b that were measured with a polymer-in-salt electrolyte; ^cInterdigitated microelectrodes were used as source and drain, and width is calculated from the product of the number of "fingers" and the width of their overlap;

1.4.1. Early mixed conducting polymers: Ppy and PANI

Polypyrrole (Ppy) and polyaniline (PANI), shown in **Figure 1.15**, are among the earliest reported materials that have been used in OECTs. In the first OECT invented by Wrighton and colleagues in 1984, Ppy was anodically electropolymerized across gold electrodes separated by micro-scale gaps as the channel material, and the device was gated by an organic electrolyte.⁸² Although the device showed accumulation mode behavior reaching transconductances of 0.1 mS and on-off current ratios of 3000, it also displayed

slow switching speeds of around 10 s. Furthermore, Ppy displays poor oxidative stability in its undoped form, leading to irreversible autooxidation in humid environments and a tendency to crosslink. PANI, on the other hand, shows similar conductivity to Ppy while also showing reversible oxidation in aqueous conditions, high environmental stability, and ability to limit electrode fouling, all of which are advantageous for bioelectronics.⁸³ As early as 1985 it was successfully used to construct OECTs with aqueous electrolyte, showing operational stability up to 10 hours.⁸⁴ While promising, PANI exhibits acid doping behavior such that its redox states are controlled by the surrounding pH. Maximum conductivity can be achieved in its emeraldine salt state, which occurs only at pH < 5.5, above which it transforms to its non-conductive emeraldine base state, limiting its applicability in biological applications. Despite their drawbacks, reports on both Ppy and PANI as mixed conductors for applications in bioelectronics are still ongoing.⁸⁵ Ppy blends with dopants have been incorporated into hydrogel networks, resulting in adhesive, stretchable, and conducting free standing films that can be applied as electronic skins and wound dressings.⁸⁶ The high transduction ability and environmental stability of PANI-based materials have been exploited to create sensors detecting peroxides, glucose, cholesterol, and various enzymes.⁸³

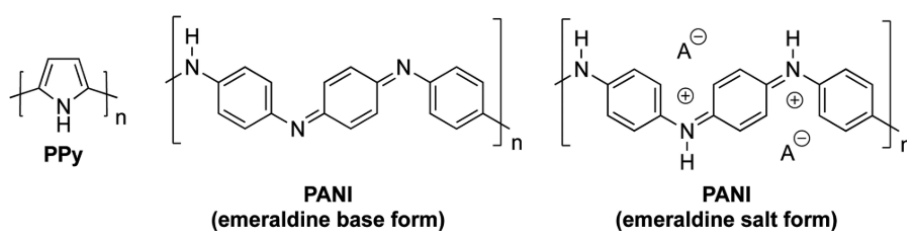


Figure 1.15. Chemical structures of early OECT channel materials.

1.4.2. Polythiophene derivatives

Polythiophenes have been extensively studied as model p-type conducting polymers to investigate hole transport in materials for OFETs, and more recently, to begin understanding mixed conductivity in channel materials for OECTs. This family of polymers generally possess better thermal, chemical, and redox stability than Ppy even against O₂ and moisture, which may be attributed to the presence of the sulfur atom which helps to stabilize positive charge on the polymer backbone.⁸⁷ Functionalization of the thiophene monomer with alkyl side chains, such as methyl (P3MT) and hexyl (P3HT) groups, promotes the solubility of their polymers in various organic solvents, allowing extensive control over the semicrystalline morphology and subsequent optoelectronic properties of the resulting films using facile solution processing techniques.⁸⁸ Furthermore, chemical synthesis of substituted polythiophenes can yield highly regioregular structures displaying head-to-tail configuration, leading to very well-oriented self-assembled solid state structures with narrowly distributed stacking distances in the crystalline domains of solution-cast films.⁸⁹ As a result, these films show high electrical conductivities upon doping with I₂ vapor, reaching >100 S cm⁻¹ in P3HT and up to 1000 S cm⁻¹ in a dodecyl-substituted polythiophene (P3DDT).⁹⁰

Substituting hydrophilic side chains consisting of short glycol $-(\text{OCH}_2\text{CH}_2)_n$ or hydroxyl end groups (-OH) onto thiophene-based polymers, shown in **Figure 1.16**, leads to bulk electrochemical doping in accumulation-mode devices operating at low potentials (< 1 V) in aqueous electrolyte. Since these semiconducting polymers are solution-processable in organic solvents only, their films do not require special treatments like cross-linking to operate in aqueous media. Polythiophenes and their derivatives consisting of fused aromatic rings such as poly(2,5-bis(3-alkylthiophen-2-yl)thieno[3,2-b]-thiophenes (PBTTT) and polybenzo[1,2-b:4,5-b']dithiophenes (PBDT) have been functionalized with glycol chains to yield materials with low electrochemical potentials and high volumetric

the conjugated backbone and the glycol side chains in the polymer P3MEEET, presented in **Figure 1.16** with the ethyl spacer highlighted in bold, has also been shown to maintain relatively low passive swelling (upon immersion in water/electrolyte) while enhancing active swelling (during electrochemical doping).⁶⁹ As a result, P3MEEET shows higher volumetric capacitance and higher μ_{OECT} than its counterpart with no ethyl spacer on the sidechain. One drawback in employing an alkyl spacer is that it distances the electron-donating side group from the polythiophene backbone, which leads to higher electrochemical oxidation potentials and about 300 mV increase of the OECT threshold voltage. Alternatively, hydroxylated polythiophenes (P3HHT) show significantly less passive and active swelling relative to the glycolated polythiophene derivatives, however at the expense of switching speed, indicated by slow sweep rates required to measure OECT characteristics, and lower μC^* performance.⁶⁷ Nonetheless, OH-functionalization does not seem to change the short- and long-range ordering relative to non-functionalized P3HT, suggesting that the hole transport may be unaffected.⁹³ Thus, polymers based on hydroxylated thiophene building blocks can serve as reliable model systems to study structure/property interrelations in mixed conducting materials without factors such as excess swelling nor additional backbone disorder induced by the sidechains.

1.4.3. Conjugated polyelectrolytes

Polythiophenes substituted with ionic moieties as shown in **Figure 1.17** have also gained attention since the presence of mobile counterions in the material leads to ionic conductivity, while anionic sidechains may induce self-doping. The pristine state of these polymers can exist either in the acidic form ($\text{R-A}^+\text{H}^+$) or conjugate base form (R-A^-) depending on the acid-base equilibria of the groups. Polythiophene functionalized with alkyl-sulfonate sidechains (PTHS) exists as a semiconducting polymer salt in its pristine state, leading to accumulation mode behavior in OECTs.⁷¹ The doping mechanism may involve

stabilization of the positive polarons by counterions from the external electrolyte, or stabilization by the sulfonate anion, possibly dissociated from the internal counterion, in a self-doping manner. Sulfonate-terminated side chains have also been substituted onto PEDOT (PEDOT-S) to yield conducting acids that yield depletion type OECTs.⁹⁴

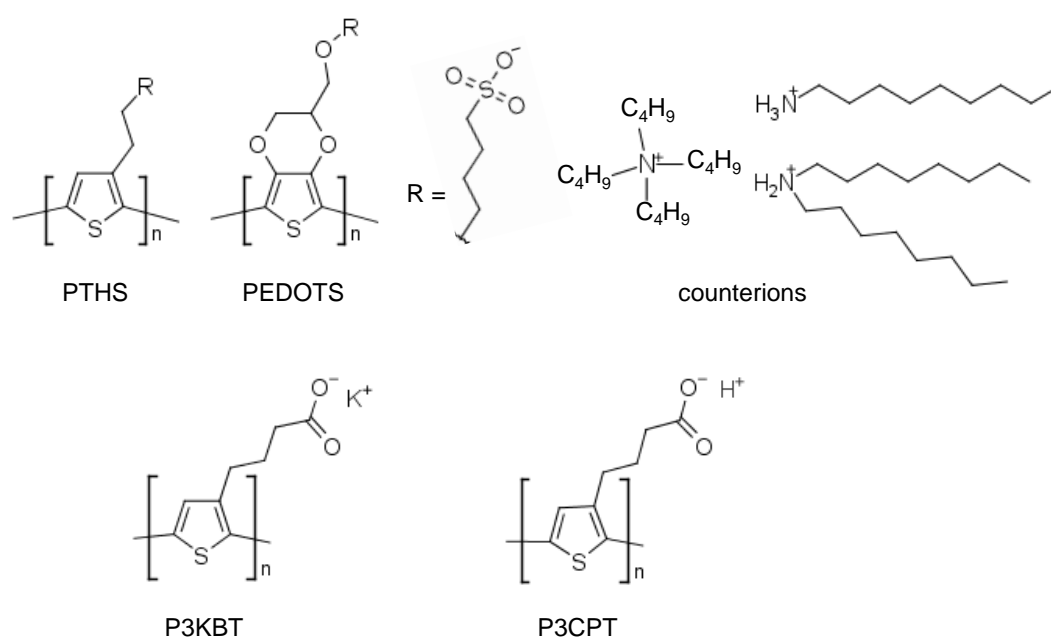


Figure 1.17. Some conjugated polyelectrolytes and their counterions used as the mixed conducting channel in OECTs.

A problem with employing conjugated polyelectrolytes such as PEDOT-S and PTHS is that they tend to be water-soluble and therefore need to be crosslinked with additives, a common one being (3-glycidyloxypropyl) trimethoxysilane (GOPS), to improve their stability in aqueous media. Alternatively, the use of bulky intrinsic counterions may yield water-insoluble salts. Protonated PEDOT-S could be converted to ammonium salt forms by ion exchange processes with either dioctylammonium chloride ($((Oct)_2NH_2Cl)$) or nonylammonium chloride ($((Nonyl)NH_3Cl)$).⁹⁴ This changes the solubility of the material from

aqueous- to organic-soluble and shifts its electrochemical potential. Consequently, OECTs of PEDOT-S[(Oct)₂NH₂] exhibit hybrid operation, being either accumulative or depletive depending on the gate bias polarity due to a threshold voltage > 0 V and saturated “on” state at more negative potentials. Also, greater steric hindrance in the counterion of PEDOT-S[(Oct)₂NH₂] offers better operational stability in its devices than those of PEDOT-S[H]. In another case, carboxylate-functionalized (-COO⁻ K⁺) polythiophene salts, poly(3-(potassium-4-butanoate)-thiophene-2,5-diyl) (P3KBT), have also been used to fabricate accumulation mode OECTs operating in 0.1 M NaCl aqueous electrolyte.⁹⁵ Although P3KBT is water-soluble, spray-cast films could be treated in an acidic organic solution of paratoluenesulfonic acid in methanol to yield solvent-resistant (water and several other organic solvents) carboxylic acid-functionalized polythiophene films, poly [3-(4-carboxypropyl)-thiophene] (P3CPT).

1.4.4. Diketopyrrolopyrrole-based conjugated polymers

One recently emerging family of mixed conducting polymers employed in OECTs are diketopyrrolopyrrole-based conjugated polymers (PDPP). These polymers have been extensively studied as high charge carrier mobility materials in OFETs whose majority charge carrier can be varied from p⁻⁹⁶ to n-type⁹⁷ and even ambipolar⁹⁸ semiconductor character upon copolymerizing with other aromatic monomers. They have also been used as acceptor units in low band gap donor-acceptor polymers for sensitizing layers in organic solar cells.⁹⁹ Like polythiophenes, PDPPs can be functionalized with solubilizing sidechains, typically branching alkyl chains, to facilitate processability. The nature of the comonomers and flanking units can also influence the polymer’s molecular geometry, optoelectronic properties, and subsequent device performance.⁹⁹ For instance, strongly electron-donating thienyl groups (T) as flanking units in PDPPs (polymers consisting of -T-DPP-T- units) leads to lower bandgap materials, coplanar structures and efficient orbital overlap leading to high

mobilities.¹⁰⁰ **Figure 1.18** presents the chemical structures of thienyl-flanked glycolated PDPPs linked with various comonomers including EDOT, triethyleneglycol-substituted thiophene (MEET), thienothiophene (TT) and methoxylated thiophene (MeOT2) units that have been investigated as p-type mixed conductors for accumulation mode OECTs.^{65,66,68}

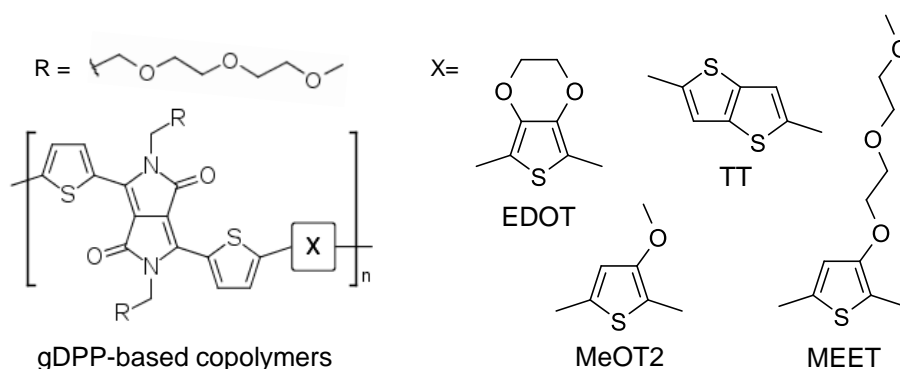


Figure 1.18. Polymers of thienyl-flanked glycolated DPP copolymerized with different aromatic monomers X have recently been tested in OECTs.

Glycol sidechains have also been incorporated onto these DPP monomers to enhance ion uptake and capacitance when operating in aqueous electrolytes. EDOT and MEET comonomers both exhibit similar hole mobilities around $0.1 \text{ cm}^2 \text{ V}^{-1} \text{ s}^{-1}$, however MEET comonomers lead to much higher capacitances, which results in better overall μC^* performance of $45 \text{ F cm}^{-1} \text{ V}^{-1} \text{ s}^{-1}$.⁶⁶ On the other hand, PDPP polymerized with EDOT comonomers exhibit slightly better operational stability, perhaps due to the electrochemical stability of EDOT.⁶⁸ PDPP copolymerized with TT (p(gDPP-TT)) and bithiophene (p(gDPP-T2)) comonomers stand out, showing impressively high μC^* performances of 125 and 342 $\text{F cm}^{-1} \text{ V}^{-1} \text{ s}^{-1}$, respectively.⁶⁵ The difference in performance is due to their mobilities of 0.6 and $1.55 \text{ cm}^2 \text{ V}^{-1} \text{ s}^{-1}$ for p(gDPP-TT) and p(gDPP-T2), respectively. On the other hand, PDPP copolymerized with MeOT2 units (p(gDPP-MeOT2)) show a lower hole mobility of 0.28 cm^2

$V^{-1} s^{-1}$ and, consequently, relatively lower μC^* performance of only $57 F cm^{-1} V^{-1} s^{-1}$. The lower mobility of p(gDPP-MeOT2) has been attributed to polaron localization owing to the large differences in energy levels between DPP and MeOT2 units. Specifically, DFT simulations suggest that charges are localized on the MeOT2 units. On the other hand, p(gDPP-TT) and p(gDPP-T2), in which the energies between the units are more closely matched, exhibit more delocalized HOMO orbitals and greater polaron charge distribution over the different segments. In terms of operational stability, however, p(gDPP-MeOT2) outperforms p(gDPP-T2) and p(gDPP-TT). This has been attributed to its lower ionization potential that could better stabilize the hole polaron. These examples clearly highlight the tunability of the mixed conducting properties of PDPP-based copolymers and their devices by molecular design.

1.4.5. N-type polymers

N-type conducting polymers whose majority charge carriers are electrons rather than holes can be very interesting in bio-transistors since their conductivity can be sensitive to cation fluxes that govern several physiological functions. Furthermore, these materials can be employed as electron acceptors for mediator-free sensing of enzymatic redox reactions¹⁰¹ and anodes in enzymatic fuel cells.¹⁰² Unfortunately, extensive practical application of n-type polymers is limited due to their scarcity and instability in air as a result of charge carrier trapping by water and oxygen.^{62,103} Despite such difficulties, a few n-type polymers showing mixed ionic and electronic conductivity, such as those given in **Figure 1.19**, have been reported.

limit detrimental swelling of the polymer, while enhancing its μC^* performance and improving its electrochemical stability at low potentials.¹⁰⁵ Alternatively, an n-type polymer based on condensed electron-deficient aryl lactam backbones has also been engineered with glycol sidechains (pgNgN) to yield high mixed conductivity.⁷⁵ These polymers exhibit highly rigid and planar conjugated backbone structures with no single linking bonds. The lack of donor-acceptor character was also intended in the synthesis of these polymers to yield highly delocalized LUMO frontier orbitals, resulting in electron mobilities in the $10^{-3} \text{ cm}^2 \text{ V}^{-1} \text{ s}^{-1}$ range. With a high volumetric capacitance of 240 F cm^{-3} , pgNgN exhibits a μC^* approaching $0.05 \text{ F cm}^{-1} \text{ V}^{-1} \text{ s}^{-1}$. This is less than the performance of its counterpart with less glycol sidechain fraction (pgNaN), which shows higher electron mobilities resulting in a μC^* of about $0.65 \text{ F cm}^{-1} \text{ V}^{-1} \text{ s}^{-1}$. This has been linked to the longer coherence length of the π -stacks estimated for pgNaN from GIWAXS measurements relative to that of the fully glycolated pgNgN, which hints at the negative effects of glycol side chains to the structural order of the films. The development of n-type mixed conducting polymers without necessitating any hydrophilic sidechains is also possible as demonstrated by reports of devices based poly(benzimid azobenzophenanthroline) (BBL) showing accumulation mode OECT behavior.⁷⁴ This polymer shows good electrochemical stability and high electron mobility owing to its ladder-type structure leading to significant order along the backbone direction and tight π -stacking. On the downside, BBL-based OECTs exhibit slower switching times relative to P(gNDI-T2) based devices. Surprisingly, BBL also shows high volumetric capacitance, early reduction onsets hinting at low energy barriers to ion penetration, and high degrees of irreversible swelling despite the absence of any hydrophilic moiety. It has been suggested that this may be the result of electrolyte penetration into void spaces of the film structure. The high capacitance of about 700 F cm^{-3} combined with high electron mobility reaching $2 \times 10^{-3} \text{ cm}^2 \text{ V}^{-1} \text{ s}^{-1}$ in BBL results in μC^* performance up to $2 \text{ F cm}^{-1} \text{ V}^{-1} \text{ s}^{-1}$, the highest reported so far for n-type mixed conducting polymers.

1.4.6. Multicomponent polymer systems

Arguably the most common multicomponent material employed in OECTs to date is PEDOT:PSS and its mixtures with other components as shown in **Figure 1.20** and mentioned in the following text. PEDOT, a polymer based on a bicyclic ring thiophene monomer, was synthesized in order to prevent steric effects and support higher conductivities.¹⁰⁶ Meanwhile, the 3,4-dialkoxy substitutions can stabilize positive charges thereby enhancing the redox stability of the material. However, PEDOT alone is insoluble. To improve material processability, EDOT is polymerized with polymeric salts in water to yield aqueous dispersions of oxidized PEDOT stabilized by a counter-polyanion. The most common one is polystyrene sulfonate (PSS). As a result of incorporating a polyelectrolyte, PEDOT:PSS also conducts ions with an ion mobility of about $10^{-3} \text{ cm}^2 \text{ V}^{-1} \text{ s}^{-1}$.¹⁰⁷

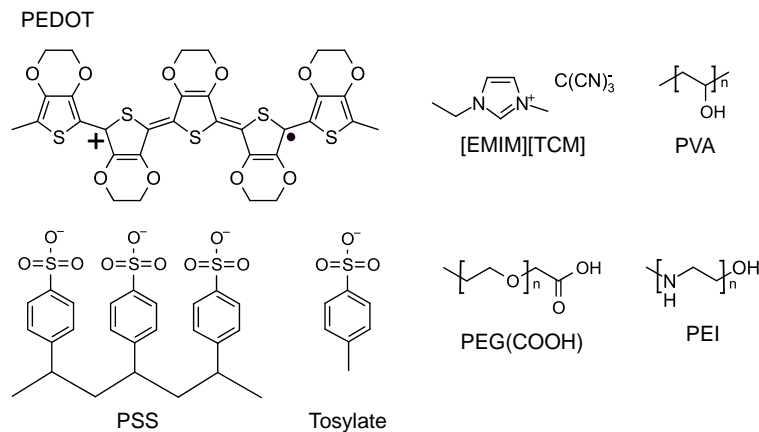


Figure 1.20. Chemical structures of PEDOT:PSS, PEDOT:Tosylate and some others that have been incorporated in multicomponent mixed conducting materials as mentioned in the main text.

One drawback of PEDOT:PSS is that, due to its water-solubility, it usually requires crosslinking agents (e.g., (3-glycidyloxypropyl)trimethoxysilane or GOPS, about 1 wt%) to

form stable films, especially against operation in aqueous media. Increasing film rigidity by crosslinking can make it more difficult for ions to flow through the material.¹⁰⁷ Another issue with incorporating PSS is that it seems to decrease the conductivity of the material, which is attributed to excess PSS preventing dense packing and interconnectivity of the electronically conducting PEDOT:PSS-rich phases. To resolve this, conductivity enhancing additives such as surfactants (dodecylbenzenesulfonic acid, DBSA) or polar and high-boiling point solvents (e.g., ethylene glycol or EG, DMSO) are usually mixed with the aqueous dispersions before casting films.⁵⁶ Films cast from a typical formulation of PEDOT:PSS (PH-1000 from Heraeus Clevis GmbH) including additives ethylene glycol (5 %v/v) and DBSA (0.2 %v/v) show hole mobilities (measured in an OECT) of about $2 \text{ cm}^2 \text{ V}^{-1} \text{ s}^{-1}$, volumetric capacitances up to 39 F cm^{-3} , and a μC^* performance of $47 \text{ F cm}^{-1} \text{ V}^{-1} \text{ s}^{-1}$ as measured from OECTs.^{6,14,81} Although such additives can tune the performance of commercially acquired dispersions, they can also make it more difficult to predict morphological changes. Alternatively, ionic liquids can also be added as “conductivity enhancers”. Films cast from PEDOT:PSS dispersions mixed with 1-ethyl-3-methylimidazolium tricyanomethanide ([EMIM][TCM]) exhibit higher μ_{OECT} (reaching $4 \text{ cm}^2 \text{ V}^{-1} \text{ s}^{-1}$), C^* (90 F cm^{-3}), and, subsequently, μC^* performance ($335 \text{ F cm}^{-1} \text{ V}^{-1} \text{ s}^{-1}$) than typical formulations with ethylene glycol.⁸⁰ It is suggested that the enhanced performance might be related to the microfibrillar morphology observed under bright-field TEM. Yet another highly successful approach to tune the mixed conducting properties of PEDOT:PSS is by sulfuric acid (H_2SO_4) post-treatment of the films (labelled as “Crys-P”).⁵⁵ This method can significantly increase the crystallinity of the PEDOT:PSS-rich phases (observed from GIWAXS) while removing excess PSS (evidenced by x-ray photoelectron spectroscopy, XPS) upon rinsing the films, both which might explain the high conductivities of resulting films (up to 5000 S cm^{-1} compared to 1 S cm^{-1} of pristine PEDOT:PSS films). Subsequently, Crys-P exhibits high μ_{OECT} ($4 \text{ cm}^2 \text{ V}^{-1} \text{ s}^{-1}$), but especially high C^* (113 F cm^{-3}) and, therefore, high μC^* ($490 \text{ F cm}^{-1} \text{ V}^{-1} \text{ s}^{-1}$). Such enhancement of performance is again attributed to a

fibrillar morphology in nano-length scales observed under combined electron microscopy techniques. In fact, for most of the methods mentioned above, it is believed that the mechanism of enhancing the conductivity involves inducing phase separation of PEDOT:PSS-rich and PSS-rich phases, which allows removal of excess PSS by rinsing. Meanwhile, it has been suggested that methods that result in microfibrillar film morphologies can support high C^* due to the high aspect ratio microstructure that leads to a large interfacial area between the electron-rich and ion-rich phases.⁸⁰

Multicomponent systems based on PEDOT have also been designed to facilitate biofunctionalization of the material towards building OECT biosensors. For instance, PEDOT:PSS dispersions mixed with polyvinyl alcohol (PVA) yields films with alcohol groups on the surface.¹⁰⁸ These react with chemical-vapor-deposited GOPS to yield silane groups that can later chemically link with various biomolecules. PEDOT-derivatives doped and stabilized by other electrolytes can also be biofunctionalized. One such derivative is the tosylate anion-doped PEDOT (PEDOT:TOS), polymerized by oxidation using Fe(III) *p*-toluenesulfonate (tosylate). PEDOT:TOS dispersions have been mixed with carboxylic acid-functionalized polyethylene glycol (PEG(COOH)), a common biocompatible material often used in tissue engineering applications.¹⁰⁹ The alcohol groups allow further biofunctionalization of the deposited films. Similarly, PEDOT:TOS has also been mixed with polyallylamine hydrochloride (PAH, a polycation) comprising of NH_2 moieties, which allow the electrostatic anchoring of enzymes such as acetylcholinesterase (AChE).¹¹⁰ An important detail is that all of these approaches allow biofunctionalization after film fabrication and treatment, which typically involves solvents and temperatures too harsh for biomolecules. Furthermore, in all the blends mentioned here, blending does not drastically change the OECT performance relative to those of the neat PEDOT:PSS or PEDOT:TOS.

Incorporating additional components to PEDOT:PSS can also yield other interesting device functionalities. For instance, mixing PEDOT:PSS with polyethylenimine (PEI) results

in an electrochemical doping mechanism that can be exploited in non-volatile memory devices.¹¹¹ Specifically, protonation of PEI during device operation induces its electrostatic interaction with PSS, effectively stabilizing the de-doped state of PEDOT. This allows multiple non-volatile conductance states without relying on slow doping or ion uptake kinetics. Another example is the addition of molecular de-dopants in the form of aliphatic amines to PEDOT:PSS dispersions to yield accumulation mode OECTs.¹¹² For instance, N-methyl-2,2'-diaminodiethylamine (DEMTA) has been mixed into PEDOT:PSS. Heating the films induces electron transfer from the amine to the PEDOT and effectively de-dopes the polymer. As a result, OECTs may operate in accumulation mode ($g_{m,max} = 74 \text{ S cm}^{-1}$, $I_{ON/OFF} = 10^3$) with high cycling stability, while the threshold voltages can be tuned further by careful design of the molecular additive.

Several examples of multicomponent mixed conductors can be named based on PEDOT:PSS alone, however other polymers have also been modified by blending. Blends of the conjugated polyelectrolytes PTHS, PEDOT-S[H], and PEDOT-S[(Oct₂)NH₂] (bulky counterion) allow manipulation of their OECT threshold voltages at values between those of the neat materials.⁷³ It is suggested that this control is driven by the difference in the solubility of PEDOT-S[H] (soluble in water) and PEDOT-S[(Oct₂)NH₂] (soluble in methanol). Thus, blending PTHS with PEDOT-S[H] in water shifts the V_t from -0.2 V to 0 V, while blending PTHS with PEDOT-S[(Oct₂)NH₂] in methanol shifts the V_t to -0.4 V. Meanwhile, although the OECT transconductances and $I_{ON/OFF}$ of the different blends are quite similar to that of PTHS, the blends do exhibit faster response speeds than the neat PTHS. In another case, PEDOT-S has also been blended with poly(2-(3-thienyl)ethoxy-4-butylsulfonate) (PTEB-S) to yield a single OECT that can exhibit electrochromic behavior over multiple colors (red, green, and blue, in order, with increasing applied voltage).⁷⁸ While PTEB-S is responsible for most of the electrochromic behavior, it is a poor conductor and has poor redox stability. Blending it with PEDOT-S increases the OECT transconductance and cycling stability, while also increasing the device response speed. The issue with these

polyelectrolyte blends, however, is that they tend to be water soluble (even with the bulky hydrophobic counterion). Thus, a polymer-in-salt electrolyte (poly-2-hydroxyethyl methacrylate, PHEMA, network in BMIMBF₄ ionic liquid) is used in the devices.

Instead of polyelectrolytes, non-ionic semiconducting polymers may also be blended with ion-conducting polymers to develop mixed conductors. To enhance the volumetric doping of P3HT in aqueous electrolyte, one attempt is to blend it with PEO.⁷⁹ Encouragingly, EQCM-D suggests that addition of PEO does enhance hydrated ion uptake in the material relative to the neat P3HT, which shows no signs of mass changes. Meanwhile, the cyclic voltammograms of the films in aqueous electrolyte do show oxidations onsets for the blends (0.55 to 0.65 V) within the investigated potential window (-0.6 to 0.8 V), unlike neat P3HT. Consequently, the P3HT blend with PEO does exhibit higher μC^* (0.6 F cm⁻¹ V⁻¹ s⁻¹) than the neat P3HT (0.02 F cm⁻¹ V⁻¹ s⁻¹), however the performance is very poor compared to current state-of-the-art p-type mixed conducting polymers (μC^* reaching 500 F cm⁻¹ V⁻¹ s⁻¹). Thus, the opportunity currently exists to explore non-ionic mixed conducting polymer blends in OECTs and establish their design criteria.

1.5. Summary and research direction

Several key features of mixed conducting polymers can be identified from the performance of their electrochemical transistors. For instance, the mode and polarity of device operation, as well as the potential window of the device, will be determined by the redox properties of the active channel material. Also, since the electrochemical response of the polymer relies on counterions to maintain charge neutrality, electronic charge injection is coupled with the ionic transport properties of the material. Consequently, the response speed of devices may be limited by the mobility of ions. Furthermore, the OECT transconductance, g_m , which measures the performance of the device according to the

change in drain current with applied gate voltage, will depend on how well ions can penetrate the active material to support changes in the bulk conductance. One parameter that can reflect this is the volumetric capacitance, C^* . Finally, the conductivity of the channel will also depend on the electronic mobility, μ , of the active material. Thus, the design of high-performance mixed conductors typically aims at increasing electronic mobility and ionic transport, while minimizing the redox potentials to allow operation at low bias. The latter is especially important for applications interfacing with water, which gives a narrow potential window beyond which parasitic side reactions may occur, and for applications with sensitive biological species.

Recent efforts to develop mixed conducting polymers usually involves engineering polar sidechains onto high-mobility conjugated polymer backbones, previously designed for other applications such as OFETs and organic solar cells, to increase their ionic conductivities. A commonly employed functional group substituted onto various p- and n-type conjugated polymers is ethylene glycol. Indeed, this approach has yielded some of the best performing mixed conducting materials in terms of the μC^* parameter. One issue that may arise from this method is that it can lead to excessive swelling of the conducting material with water molecules, either from the external aqueous electrolyte or even from a humid environment. Excessive water uptake has been shown to be detrimental to the response time of devices and can also lead to irreversible mass changes in the active polymer. Consequently, this disturbs the structural order of the semiconductor and effectively degrades its electronic properties. Eventually, the structural integrity of the films may also be compromised and lead to detachment from underlying electrodes. As a result, such systems can have poor operational stability. Fortunately, despite initial impressions that hydration-induced swelling is necessary for more efficient ion uptake from an external electrolyte, results from low-swelling polymers such as P3HHT and the remarkable n-type BBL ladder polymer indicate that good mixed conducting performance can be achieved without excessive water uptake in the material. Meanwhile, most efforts to control water

uptake involve the tedious synthesis of a series of polymers with various sidechain distributions and lengths.

Alternatively, we propose blending modification of mixed conducting polymers with hydrophilic, ion-conducting co-components as a simple strategy to enhance ionic transport in these materials. This method avoids the direct modification of the active semiconducting backbone to prevent inducing further conformational disorder that can decrease its electronic performance. Specifically, we blend P3HT-*co*-P3HHT (a random copolymer comprising 50% -3HT or -3HHT monomer composition) with P3HT-*b*-PEO (a block copolymer of P3HT and PEO) using a straightforward solution-based method (detailed in the appendix section **A.1 Materials and film deposition**) without involving any further chemical synthetic steps nor specific post-deposition film treatment (*e.g.*, crosslinking or annealing). We choose P3HT-*co*-P3HHT as the active mixed conducting component according to previous work showing that copolymerization of hexylthiophene and hydroxyhexylthiophene with up to 50% comonomer composition does not change the short- and long-range order of resulting films.⁹³ This is an initial indicator that the material might maintain its electronic properties, linked to its solid state structure, even after functionalization. Furthermore, preliminary GIWAXS investigations given in **Figure 1.21** reveal that the structure of P3HT-*co*-P3HHT is less affected upon exposure to humidity than the P3HHT homopolymer, which is a promising indication of low degrees of hydration-induced swelling. Consequently, we expect high operational stability from the random copolymer.

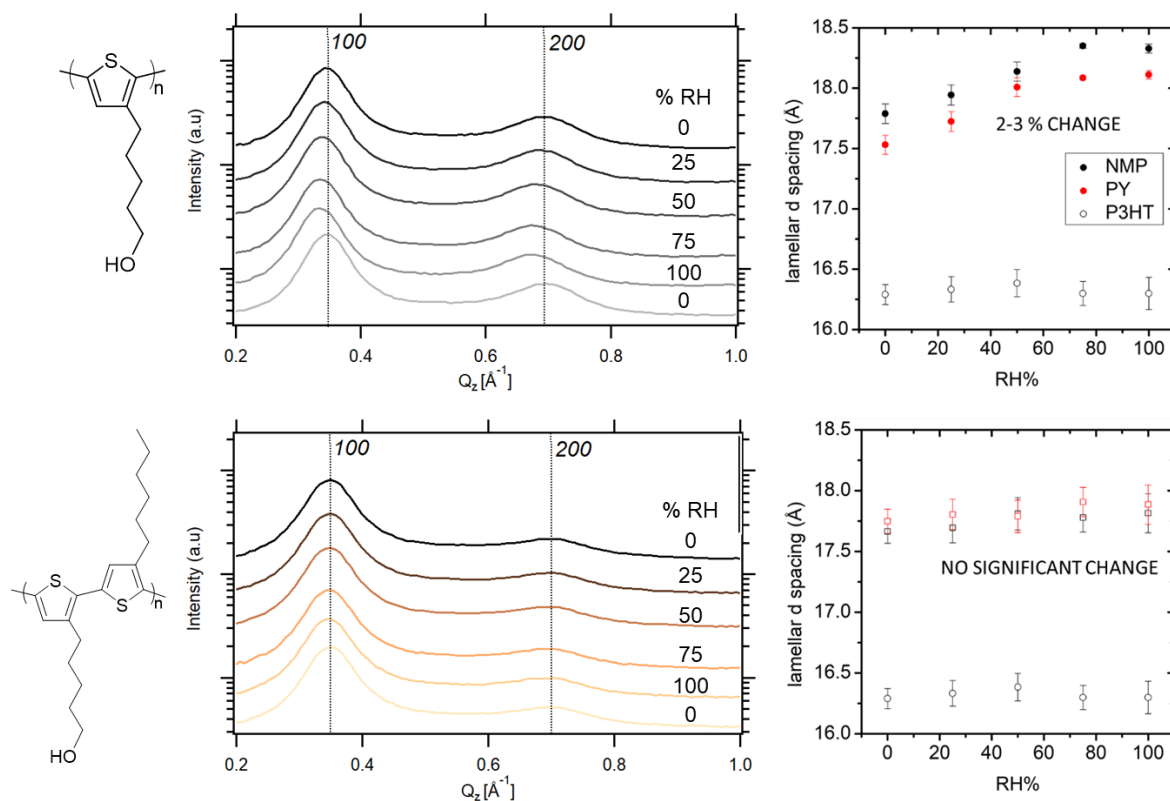


Figure 1.21. In-situ GIWAXS analysis of humidity-induced swelling in P3HHT and the random copolymer P3HT-co-P3HHT. Shift of peak positions in P3HHT to lower Q_z values with increasing relative humidity (RH%) indicates swelling of the material (top-left). Up to 2-3% increase in the lamellar stacking distance is observed in P3HHT at 100 %RH (top-right). No apparent change can be observed for P3HT-co-P3HHT (bottom). Note that the swelling is reversible upon changing the environment from 100 to 0 %RH.

As the “additive”, we choose the amphiphilic block copolymer of P3HT and PEO (P3HT-*b*-PEO). This has been previously reported to exhibit phase separation and simultaneous electronic and ionic conductivity.¹¹³ Thus, the block copolymer potentially offers bicontinuous pathways for electronic and ionic conduction, which can be exploited in blends with the mixed conducting P3HT-co-P3HHT. The block copolymer might also maintain the structural stability of the blend since phase separation should be limited to small scales due to the chemical linkage between each block. Additionally, the P3HT moiety might also act as a compatibilizing unit that can further limit large scale phase separation in

the blend. This might contribute to preserving the electronic properties of the material and would be beneficial for the long-term operational stability of the resulting devices.

Overall, our method combines both chemical and blending modification of the archetypal conjugated polymer P3HT with an ionically conducting PEO moiety to increase its ionic transport properties while potentially maintaining its electrical properties. Indeed, the results discussed in the following chapters indicate the viability and compatibility of this combined approach to develop high-performance mixed conducting materials. Similar techniques can be easily applied to other semiconducting polymers to expand their functionality and enhance their electrochemical performance.

1.6. References

1. Rivnay, J., Owens, R. M. & Malliaras, G. G. The rise of organic bioelectronics. *Chem. Mater.* **26**, 679–685 (2014).
2. Inal, S., Rivnay, J., Suiu, A. O., Malliaras, G. G. & McCulloch, I. Conjugated Polymers in Bioelectronics. *Acc. Chem. Res.* **51**, 1368–1376 (2018).
3. Rivnay, J. *et al.* Organic electrochemical transistors. *Nat. Rev. Mater.* **3**, 17086 (2018).
4. Angione, M. D. *et al.* Interfacial electronic effects in functional bilayers integrated into organic field-effect transistors. *Proc. Natl. Acad. Sci.* **109**, 6429–6434 (2012).
5. Ranganathan, S. & McCreery, R. L. Electroanalytical Performance of Carbon Films with Near-Atomic Flatness. *Anal. Chem.* **73**, 893–900 (2001).
6. Rivnay, J. *et al.* High-performance transistors for bioelectronics through tuning of channel thickness. *Sci. Adv.* **1**, e1400251–e1400251 (2015).
7. Hengda Sun, Jennifer Gerasimov, Magnus Berggren & Simone Fabiano. n-Type organic electrochemical transistors: materials and challenges. *J. Mater. Chem. C* **6**, 11778–11784 (2018).
8. Bernards, D. A. & Malliaras, G. G. Steady-state and transient behavior of organic electrochemical transistors. *Adv. Funct. Mater.* **17**, 3538–3544 (2007).
9. Sze, S. M. & Ng, K. K. MOSFETs. in *Physics of Semiconductor Devices* 293–373 (John Wiley & Sons, Inc., 2006).

10. Faria, G. C., Duong, D. T. & Salleo, A. On the transient response of organic electrochemical transistors. *Org. Electron. physics, Mater. Appl.* **45**, 215–221 (2017).
11. Friedlein, J. T., Donahue, M. J., Shaheen, S. E., Malliaras, G. G. & McLeod, R. R. Microsecond Response in Organic Electrochemical Transistors: Exceeding the Ionic Speed Limit. *Adv. Mater.* **28**, 8398–8404 (2016).
12. Tu, D., Kergoat, L., Crispin, X., Berggren, M. & Forchheimer, R. Transient analysis of electrolyte-gated organic field-effect transistors. in *Organic Field-Effect Transistors XI* (eds. Bao, Z. & McCulloch, I.) **8478**, 84780L (International Society for Optics and Photonics, 2012).
13. Xie, W., Menke, S. M., Frisbie, C. D. & Holmes, R. J. Experimental Characterization of Charge and Exciton Transport in Organic Semiconductors. in *The WSPC Reference on Organic Electronics: Organic Semiconductors 1*, 231–291 (WORLD SCIENTIFIC, 2016).
14. Rivnay, J. *et al.* Structural control of mixed ionic and electronic transport in conducting polymers. *Nat. Commun.* **7**, (2016).
15. Tsai, T. C., Chang, H. C., Chen, C. H. & Whang, W. T. Widely variable Seebeck coefficient and enhanced thermoelectric power of PEDOT:PSS films by blending thermal decomposable ammonium formate. *Org. Electron.* **12**, 2159–2164 (2011).
16. Nielsen, C. B. *et al.* Molecular Design of Semiconducting Polymers for High-Performance Organic Electrochemical Transistors. *J. Am. Chem. Soc.* **138**, 10252–10259 (2016).
17. Inal, S., Malliaras, G. G. & Rivnay, J. Benchmarking organic mixed conductors for transistors. *Nat. Commun.* **8**, 1767 (2017).
18. Koutsouras, D. A. *et al.* Impedance Spectroscopy of Spin-Cast and Electrochemically Deposited PEDOT:PSS Films on Microfabricated Electrodes with Various Areas. *ChemElectroChem* **4**, 2321–2327 (2017).
19. Polyravas, A. G. *et al.* Impact of contact overlap on transconductance and noise in organic electrochemical transistors. *Flex. Print. Electron.* **4**, 044003 (2019).
20. Hoffmann, R., Janiak, C. & Kollmar, C. A Chemical Approach to the Orbitals of Organic Polymers. *Macromolecules* **24**, 3725–3746 (1991).
21. Geoghegan, M. & Hadziioannou, G. *Polymer electronics*. (Oxford University Press, 2013).
22. Griffith, M. J., Cottam, S., Stamenkovic, J., Posar, J. A. & Petasecca, M. Printable Organic Semiconductors for Radiation Detection: From Fundamentals to Fabrication and Functionality. *Front. Phys.* **8**, (2020).
23. Peierls, R. *More Surprises in Theoretical Physics. Princeton series in physics*

- (Princeton University Press, 2020).
24. Castiglioni, C., Zerbi, G. & Gussoni, M. Peierls distortion in trans polyacetylene: Evidence from infrared intensities. *Solid State Commun.* **56**, 863–866 (1985).
 25. Heeger, A. J. Semiconducting and Metallic Polymers: The Fourth Generation of Polymeric Materials (Nobel Lecture). *Angew. Chemie Int. Ed.* **40**, 2591–2611 (2001).
 26. Bredas, J. L., Themans, B., Andre, J. M., Chance, R. R. & Silbey, R. The role of mobile organic radicals and ions (solitons, polarons and bipolarons) in the transport properties of doped conjugated polymers. *Synth. Met.* **9**, 265–274 (1984).
 27. Salaneck, W. R., Friend, R. H. & Brédas, J. L. Electronic structure of conjugated polymers: Consequences of electron-lattice coupling. *Physics Report* **319**, 231–251 (1999).
 28. Howard, E. L. *et al.* Cost-Effective, Flexible, and Colorful Dynamic Displays: Removing Underlying Conducting Layers from Polymer-Based Electrochromic Devices. *ACS Appl. Mater. Interfaces* **13**, 16732–16743 (2021).
 29. Aziz, S. B., Woo, T. J., Kadir, M. F. Z. & Ahmed, H. M. A conceptual review on polymer electrolytes and ion transport models. *J. Sci. Adv. Mater. Devices* **3**, 1–17 (2018).
 30. Kuo, P. L., Liang, W. J. & Chen, T. Y. Solid polymer electrolytes V: Microstructure and ionic conductivity of epoxide-crosslinked polyether networks doped with LiClO₄. *Polymer (Guildf)*. **44**, 2957–2964 (2003).
 31. Sai, R. *et al.* Role of polar side chains in Li⁺ coordination and transport properties of polyoxetane-based polymer electrolytes. *Phys. Chem. Chem. Phys.* **19**, 5185–5194 (2017).
 32. Xue, Z., He, D. & Xie, X. Poly(ethylene oxide)-based electrolytes for lithium-ion batteries. *Journal of Materials Chemistry A* **3**, 19218–19253 (2015).
 33. Bresser, D., Lyonnard, S., Iojoiu, C., Picard, L. & Passerini, S. Decoupling segmental relaxation and ionic conductivity for lithium-ion polymer electrolytes. *Mol. Syst. Des. Eng.* **4**, 779–792 (2019).
 34. Bennington, P. *et al.* Role of solvation site segmental dynamics on ion transport in ethylene-oxide based side-chain polymer electrolytes. *J. Mater. Chem. A* **9**, 9937–9951 (2021).
 35. Baskoro, F., Wong, H. Q. & Yen, H.-J. Strategic Structural Design of a Gel Polymer Electrolyte toward a High Efficiency Lithium-Ion Battery. *ACS Appl. Energy Mater.* **2**, 3937–3971 (2019).
 36. Giridharagopal, R. *et al.* Electrochemical strain microscopy probes morphology-induced variations in ion uptake and performance in organic electrochemical

- transistors. *Nat. Mater.* **16**, 1–6 (2017).
37. Stavrinidou, E. *et al.* Direct measurement of ion mobility in a conducting polymer. *Adv. Mater.* **25**, 4488–4493 (2013).
 38. Flagg, L. Q. *et al.* Polymer Crystallinity Controls Water Uptake in Glycol Side-Chain Polymer Organic Electrochemical Transistors. *J. Am. Chem. Soc.* **21**, 54 (2019).
 39. Giovannitti, A. *et al.* Controlling the mode of operation of organic transistors through side-chain engineering. *Proc. Natl. Acad. Sci.* **113**, 12017–12022 (2016).
 40. Giovannitti, A. *et al.* N-type organic electrochemical transistors with stability in water. *Nat. Commun.* **7**, 1–10 (2016).
 41. Savva, A. *et al.* Influence of Water on the Performance of Organic Electrochemical Transistors. *Chem. Mater.* **31**, 927–937 (2019).
 42. Szumska, A. A. *et al.* Reversible Electrochemical Charging of n-Type Conjugated Polymer Electrodes in Aqueous Electrolytes. *J. Am. Chem. Soc.* **143**, 14795–14805 (2021).
 43. Volkov, A. V. *et al.* Understanding the Capacitance of PEDOT:PSS. *Adv. Funct. Mater.* **27**, 1700329 (2017).
 44. Proctor, C. M., Rivnay, J. & Malliaras, G. G. Understanding volumetric capacitance in conducting polymers. *J. Polym. Sci. Part B Polym. Phys.* **54**, 1433–1436 (2016).
 45. Noriega, R. *et al.* A general relationship between disorder, aggregation and charge transport in conjugated polymers. *Nat. Mater.* **12**, 1038–1044 (2013).
 46. Fratini, S., Nikolka, M., Salleo, A., Schweicher, G. & Sringhaus, H. Charge transport in high-mobility conjugated polymers and molecular semiconductors. *Nat. Mater.* **19**, 491–502 (2020).
 47. Gu, K. *et al.* Assessing the Huang–Brown Description of Tie Chains for Charge Transport in Conjugated Polymers. *ACS Macro Lett.* **7**, 1333–1338 (2018).
 48. Koch, F. P. V. *et al.* The impact of molecular weight on microstructure and charge transport in semicrystalline polymer semiconductors—poly(3-hexylthiophene), a model study. *Prog. Polym. Sci.* **38**, 1978–1989 (2013).
 49. Baranovskii, S. D. Theoretical description of charge transport in disordered organic semiconductors. *Phys. status solidi* **251**, 487–525 (2014).
 50. Friedlein, J. T. *et al.* Influence of disorder on transfer characteristics of organic electrochemical transistors. *Appl. Phys. Lett.* **111**, 023301 (2017).
 51. Friedlein, J. T., McLeod, R. R. & Rivnay, J. Device physics of organic electrochemical transistors. *Org. Electron.* **63**, 398–414 (2018).
 52. Abdalla, H. Charge and Energy Transport in Disordered Organic Semiconductors. (Linköping University, 2018).

53. Berggren, M. *et al.* Ion Electron–Coupled Functionality in Materials and Devices Based on Conjugated Polymers. *Adv. Mater.* **31**, 1805813 (2019).
54. Berggren, M. & Richter-Dahlfors, A. Organic Bioelectronics. *Adv. Mater.* **19**, 3201–3213 (2007).
55. Kim, N. *et al.* Highly Conductive PEDOT:PSS Nanofibrils Induced by Solution-Processed Crystallization. *Adv. Mater.* **26**, 2268–2272 (2014).
56. Shi, H., Liu, C., Jiang, Q. & Xu, J. Effective Approaches to Improve the Electrical Conductivity of PEDOT:PSS: A Review. *Adv. Electron. Mater.* **1**, 1–16 (2015).
57. Stříteský, S. *et al.* Printing inks of electroactive polymer PEDOT:PSS: The study of biocompatibility, stability, and electrical properties. *J. Biomed. Mater. Res. - Part A* **106**, 1121–1128 (2018).
58. Merck. Poly(3,4-ethylenedioxythiophene)-poly(styrenesulfonate). (2021). Available at:
<https://www.sigmaaldrich.com/FR/fr/substance/poly34ethylenedioxythiophenepolystyrenesulfonate1234598765?context=product>. (Accessed: 30th October 2021)
59. Cameron, J. & Skabara, P. J. The damaging effects of the acidity in PEDOT:PSS on semiconductor device performance and solutions based on non-acidic alternatives. *Mater. Horizons* **7**, 1759–1772 (2020).
60. Mantione, D. *et al.* Poly(3,4-ethylenedioxythiophene):GlycosAminoGlycan Aqueous Dispersions: Toward Electrically Conductive Bioactive Materials for Neural Interfaces. *Macromol. Biosci.* **16**, 1227–1238 (2016).
61. Nitta, K., Tsumaki, M., Kawano, T., Terashima, K. & Ito, T. Printing PEDOT from EDOT via plasma-assisted inkjet printing. *J. Phys. D. Appl. Phys.* **52**, 315202 (2019).
62. De Leeuw, D. M., Simenon, M. M. J., Brown, A. R. & Einerhand, R. E. F. Stability of n-type doped conducting polymers and consequences for polymeric microelectronic devices. *Synth. Met.* **87**, 53–59 (1997).
63. Kim, S.-M. *et al.* Influence of PEDOT:PSS crystallinity and composition on electrochemical transistor performance and long-term stability. *Nat. Commun.* **2018** *9*, 1–9 (2018).
64. Moser, M. *et al.* Side Chain Redistribution as a Strategy to Boost Organic Electrochemical Transistor Performance and Stability. *Adv. Mater.* **32**, 2002748 (2020).
65. Moser, M. *et al.* Polaron Delocalization in Donor–Acceptor Polymers and its Impact on Organic Electrochemical Transistor Performance. *Angew. Chemie Int. Ed.* **60**, 7777–7785 (2021).
66. Krauss, G. *et al.* Polydiketopyrrolopyrroles Carrying Ethylene Glycol Substituents as

- Efficient Mixed Ion-Electron Conductors for Biocompatible Organic Electrochemical Transistors. *Adv. Funct. Mater.* **31**, (2021).
67. Nicolini, T. *et al.* A Low-Swelling Polymeric Mixed Conductor Operating in Aqueous Electrolytes. *Adv. Mater.* **33**, 1–7 (2021).
68. Wang, N. *et al.* Ethylenedioxythiophene incorporated diketopyrrolopyrrole conjugated polymers for high-performance organic electrochemical transistors. *J. Mater. Chem. C* **9**, 4260–4266 (2021).
69. Schmode, P. *et al.* The Key Role of Side Chain Linkage in Structure Formation and Mixed Conduction of Ethylene Glycol Substituted Polythiophenes. *ACS Appl. Mater. Interfaces* **12**, 13029–13039 (2020).
70. Reynolds, J. R. *et al.* Balancing Charge Storage and Mobility in an Oligo(Ether) Functionalized Dioxothiophene Copolymer for Organic- and Aqueous- Based Electrochemical Devices and Transistors. *Adv. Mater.* **30**, 1804647 (2018).
71. Inal, S. *et al.* A high transconductance accumulation mode electrochemical transistor. *Adv. Mater.* **26**, 7450–7455 (2014).
72. Giovannitti, A. *et al.* Energetic Control of Redox-Active Polymers toward Safe Organic Bioelectronic Materials. *Adv. Mater.* **32**, 1908047 (2020).
73. Zeglio, E. *et al.* Conjugated Polyelectrolyte Blends for Highly Stable Accumulation-Mode Electrochemical Transistors. *Chem. Mater.* **29**, 4293–4300 (2017).
74. Surgailis, J. *et al.* Mixed Conduction in an N-Type Organic Semiconductor in the Absence of Hydrophilic Side-Chains. *Adv. Funct. Mater.* **2010165**, 1–12 (2021).
75. Chen, X. *et al.* n-Type Rigid Semiconducting Polymers Bearing Oligo(Ethylene Glycol) Side Chains for High-Performance Organic Electrochemical Transistors. *Angew. Chemie Int. Ed.* **60**, 9368–9373 (2021).
76. Giovannitti, A. *et al.* N-type organic electrochemical transistors with stability in water. *Nat. Commun.* **7**, 1–9 (2016).
77. Giovannitti, A. *et al.* The Role of the Side Chain on the Performance of N-type Conjugated Polymers in Aqueous Electrolytes. *Chem. Mater.* **30**, 2945–2953 (2018).
78. Zeglio, E. *et al.* Conjugated Polyelectrolyte Blends for Electrochromic and Electrochemical Transistor Devices. *Chem. Mater.* **27**, 6385–6393 (2015).
79. Frankenstein, H. *et al.* Blends of polymer semiconductor and polymer electrolyte for mixed ionic and electronic conductivity. *J. Mater. Chem. C* **9**, 7765–7777 (2021).
80. Wu, X. *et al.* Ionic-Liquid Doping Enables High Transconductance, Fast Response Time, and High Ion Sensitivity in Organic Electrochemical Transistors. *Adv. Mater.* **31**, 1805544 (2019).
81. Khodagholy, D. *et al.* High transconductance organic electrochemical transistors.

- Nat. Commun.* **4**, 1–6 (2013).
82. White, H. S., Kittlese, G. P. & Wrighton, M. S. Chemical Derivatization of an Array of Three Gold Microelectrodes with Polypyrrole: Fabrication of a Molecule-Based Transistor. *J. Am. Chem. Soc.* **106**, 5375–5377 (1984).
 83. Dhand, C., Das, M., Datta, M. & Malhotra, B. D. Recent advances in polyaniline based biosensors. *Biosensors and Bioelectronics* **26**, 2811–2821 (2011).
 84. Paul, E. W., Ricco, A. J. & Wrighton, M. S. Resistance of polyaniline films as a function of electrochemical potential and the fabrication of polyaniline-based microelectronic devices. *J. Phys. Chem.* **89**, 1441–1447 (1985).
 85. Chujia Li. Towards conductive hydrogels in e-skins: a review on rational design and recent developments. *RSC Adv.* **11**, 33835–33848 (2021).
 86. Han, L. *et al.* Transparent, Adhesive, and Conductive Hydrogel for Soft Bioelectronics Based on Light-Transmitting Polydopamine-Doped Polypyrrole Nanofibrils. *Chem. Mater.* **30**, 5561–5572 (2018).
 87. Arya, P. S., Pandya, D. K., Chopra, K. L., Tourillon, G. & Garnier, F. Stability of Conducting Polythiophene and Derivatives. *Thin Solid Films* **2**, 349 (1980).
 88. Hotta, S., Soga, M. & Sonoda, N. Novel organosynthetic routes to polythiophene and its derivatives. *Synth. Met.* **26**, 267–279 (1988).
 89. Osaka, I. & McCullough, R. D. Advances in molecular design and synthesis of regioregular polythiophenes. *Acc. Chem. Res.* **41**, 1202–1214 (2008).
 90. McCullough, R. D., Williams, S. P., Lowe, R. D., Jayaraman, M. & Tristram-Nagle, S. Self-Orienting Head-to-Tail Poly(3-alkylthiophenes): New Insights on Structure-Property Relationships in Conducting Polymers. *J. Am. Chem. Soc.* **115**, 4910–4911 (1993).
 91. Nielsen, C. B. *et al.* Molecular Design of Semiconducting Polymers for High-Performance Organic Electrochemical Transistors. *J. Am. Chem. Soc.* **138**, 10252 (2016).
 92. Dyson, M. J. *et al.* Managing Local Order in Conjugated Polymer Blends via Polarity Contrast. *Chem. Mater.* **31**, 6540–6547 (2019).
 93. Pacheco-Moreno, C. M. *et al.* The Importance of Materials Design to Make Ions Flow: Toward Novel Materials Platforms for Bioelectronics Applications. *Adv. Mater.* **29**, 1604446 (2017).
 94. Zeglio, E., Eriksson, J., Gabrielsson, R., Solin, N. & Inganäs, O. Highly Stable Conjugated Polyelectrolytes for Water-Based Hybrid Mode Electrochemical Transistors. *Adv. Mater.* **29**, 6–11 (2017).
 95. Khau, B. V. *et al.* Carboxylic Acid Functionalization Yields Solvent-Resistant Organic

- Electrochemical Transistors. *ACS Mater. Lett.* **1**, 599–605 (2019).
96. Li, Y., Singh, S. P. & Sonar, P. A high mobility P-type DPP-thieno[3,2-b]thiophene copolymer for organic thin-film transistors. *Adv. Mater.* **22**, 4862–4866 (2010).
 97. Jeong, M. K., Suh, E. H., Lee, K., Jang, J. & Jung, I. H. Acceptor–acceptor-type conjugated polymer for use in n-type organic thin-film transistors and thermoelectric devices. *Org. Electron.* **86**, 105921 (2020).
 98. Sonar, P., Singh, S. P., Li, Y., Soh, M. S. & Dodabalapur, A. A low-bandgap diketopyrrolopyrrole-benzothiadiazole-based copolymer for high-mobility ambipolar organic thin-film transistors. *Adv. Mater.* **22**, 5409–5413 (2010).
 99. Li, W., Hendriks, K. H., Wienk, M. M. & Janssen, R. A. J. Diketopyrrolopyrrole Polymers for Organic Solar Cells. *Acc. Chem. Res.* **49**, 78–85 (2016).
 100. Nielsen, C. B., Turbiez, M. & McCulloch, I. Recent advances in the development of semiconducting DPP-containing polymers for transistor applications. *Advanced Materials* **25**, 1859–1880 (2013).
 101. Pappa, A. M. *et al.* Direct metabolite detection with an n-type accumulation mode organic electrochemical transistor. *Sci. Adv.* **4**, (2018).
 102. Ohayon, D. *et al.* Biofuel powered glucose detection in bodily fluids with an n-type conjugated polymer. *Nat. Mater.* 2019 194 **19**, 456–463 (2019).
 103. Griggs, S., Marks, A., Bristow, H. & McCulloch, I. n-Type organic semiconducting polymers: stability limitations, design considerations and applications. *Journal of Materials Chemistry C* **9**, 8099–8128 (2021).
 104. Paterson, A. F. *et al.* Water stable molecular n-doping produces organic electrochemical transistors with high transconductance and record stability. *Nat. Commun.* 2020 111 **11**, 1–11 (2020).
 105. Maria, I. P. *et al.* The Effect of Alkyl Spacers on the Mixed Ionic-Electronic Conduction Properties of N-Type Polymers. *Adv. Funct. Mater.* **31**, 2008718 (2021).
 106. Heywang, G. & Jonas, F. Poly(alkylenedioxythiophene)s—new, very stable conducting polymers. *Adv. Mater.* **4**, 116–118 (1992).
 107. Stavrinidou, E. *et al.* Direct Measurement of Ion Mobility in a Conducting Polymer. *Adv. Mater.* **25**, 4488–4493 (2013).
 108. Strakosas, X. *et al.* A facile biofunctionalisation route for solution processable conducting polymer devices. *J. Mater. Chem. B* **2**, 2537–2545 (2014).
 109. Jimison, L. H. *et al.* PEDOT:TOS with PEG: a biofunctional surface with improved electronic characteristics. *J. Mater. Chem.* **22**, 19498–19505 (2012).
 110. Fenoy, G. E., von Bilderling, C., Knoll, W., Azzaroni, O. & Marmisollé, W. A. PEDOT:Tosylate-Polyamine-Based Organic Electrochemical Transistors for High-

- Performance Bioelectronics. *Adv. Electron. Mater.* **7**, 2100059 (2021).
111. van de Burgt, Y. *et al.* A non-volatile organic electrochemical device as a low-voltage artificial synapse for neuromorphic computing. *Nat. Mater.* **16**, 414–418 (2017).
 112. Keene, S. T. *et al.* Enhancement-Mode PEDOT:PSS Organic Electrochemical Transistors Using Molecular De-Doping. *Adv. Mater.* **32**, 2000270 (2020).
 113. Javier, A. E., Patel, S. N., Hallinan, D. T., Srinivasan, V. & Balsara, N. P. Simultaneous Electronic and Ionic Conduction in a Block Copolymer: Application in Lithium Battery Electrodes. *Angew. Chemie Int. Ed.* **50**, 9848–9851 (2011).

CHAPTER 2:

Mixed conducting polymer blends for faster organic electrochemical transistors

2.1. Introduction	77
2.2. OECT characteristics at various operating rates	77
2.2.1. P3HT-co-P3HHT	79
2.2.2. Blends with P3HT- <i>b</i> -PEO	81
2.2.3. OECT performance indicators, g_m and ΔV_t	83
2.3. Performance across different channel dimensions	86
2.3.1. Channel material performance indicator, μC^*	89
2.3.2. Influence of channel dimensions on current hysteresis.....	91
2.4. Performance across blend composition.....	93
2.5. Transient response	98
2.5.1. Response to a V_g pulse	98
2.5.2. Response to various V_g waveforms	100
2.6. Summary	101
2.7. References.....	102

2.1. Introduction

Much of the operating mechanisms of emerging organic electrochemical devices relies on the unique properties of mixed ionic and electronic conductors. One factor that can limit the performance of these devices is slow ionic transport processes occurring in the active material, typically a polymeric semiconductor. Thus, we propose blending modification of mixed conducting polymers with hydrophilic, ion-conducting co-components as a simple strategy to enhance ionic transport in these materials and subsequently improve the performance of their electrochemical devices. Specifically, we blend P3HT-*co*-P3HHT (provided by Dr. Olivier Dautel, Institut Charles Gerhardt Montpellier) with P3HT-*b*-PEO (provided by Dr. Cyril Brochon, Laboratoire de Chimie des Polymères Organiques) using a straightforward, solution-based method without involving any further chemical synthetic steps nor specific post-deposition film treatment (*e.g.*, cross-linking or annealing). To evaluate the impact of blending on the mixed conductivity of the material and the performance of its devices, we fabricate and characterize organic electrochemical transistors (OECTs). We also investigate the influence of varying operating speed and channel dimensions on the OECT characteristics. Results indicate that blending primarily affects the transient performance of the OECTs, which demonstrates the viability of our initial materials design strategy. Additionally, we find that the behavior of devices exhibiting slow response can rely heavily on the operating speed employed. This should therefore be considered when evaluating the performance of various mixed conductor channel materials for practical applications.

2.2. OECT characteristics at various operating rates

To begin investigating the mixed conductivity of P3HT-*co*-P3HHT (number-average molecular weight $M_n = 30 \text{ kg mol}^{-1}$, dispersity $\mathcal{D} = 1.9$) and its blends with P3HT-*b*-PEO (M_n ,

$P_{3HT} = 5 \text{ kg mol}^{-1}$, $D_{P3HT} = 1.2$, $M_{n,PEO} = 20 \text{ kg mol}^{-1}$, $D_{PEO} \leq 1.2$), we evaluate the performance of their OECTs built on the general architecture illustrated in **Figure 2.1**.

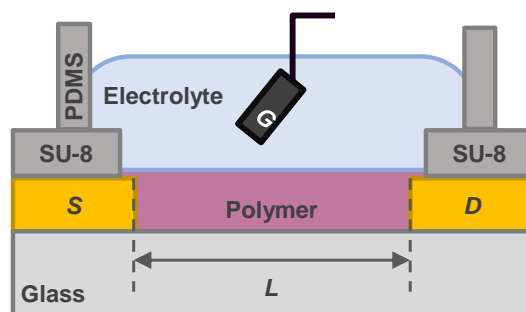


Figure 2.1. Schematic diagram of the OECTs used in this work. An Ag/AgCl pellet electrode was used as the gate (G) while patterned gold electrodes were used as the source (S) and drain (D), which were partially insulated from the electrolyte (0.1 M KCl aqueous solution) by a negative photoresist (SU-8).

The blends are processed from solution (15 mg mL^{-1} THF:NMP) and spun-cast, without specific post-deposition treatment, onto photolithographically patterned substrates (courtesy of Dr. Guillaume Wantz and Dr. Damien Thuau, *Laboratoire de l'Intégration du Matériau au Système*) consisting of gold source and drain electrodes that have been partially insulated with an epoxy resin to expose only the active channel region. The dimensions are about 90 and 20 μm for the channel width, W , and length, L , respectively, measured by optical microscopy (see appendix section **A.2.2 OECT device architecture, Figure A.2**), and the channel thickness is given by the polymer film thickness, about $100 \pm 10 \text{ nm}$, measured by mechanical profilometry. A PDMS well positioned over the active channel contains the aqueous electrolyte (0.1 M KCl) in which an Ag/AgCl pellet electrode is submerged to serve as the gate electrode. To operate the devices, potential bias is applied across the source and gate electrodes, V_g , and further bias is applied across the source and drain electrodes, V_d . This induces an ionic current through the electrolyte and

charges the transistor channel, effectively doping the semiconducting polymer and inducing an electronic current across the source and drain electrodes. The standard OECT output characteristics are obtained by measuring the drain current, I_d , during a V_d sweep at increments of constant V_g , and the transfer characteristics are obtained by measuring I_d during a V_g sweep at a constant V_d . The ranges of V_g and V_d investigated throughout this work are chosen such that the maximum performance ability of the devices could be measured while minimizing the risk of electrically degrading the polymer and side-reactions with water. Further details on film deposition, device fabrication, and characterization are given in the appendix.

2.2.1. P3HT-co-P3HHT

In measuring the output curves of devices comprising neat P3HT-co-P3HHT as the active channel material plotted in **Figure 2.2**, we immediately observe accumulation-mode behavior indicated by the increase of I_d with V_d above a certain threshold V_g . This confirms ion and hole injection leading to electrochemical doping of the initially neutral channel material during OECT operation. Additionally, we notice that the V_d limit after which I_d begins to saturate seems to depend on the operating speed employed. For instance, at a constant V_g of -0.7 V and a V_d sweep rate of 0.5 V s⁻¹ we almost only see Ohmic behavior of I_d within the V_d range investigated here (refer to **Figure 2.2**, left). On the other hand, when measuring the same device at the same V_g but at a slower V_d sweep rate of 0.25 V s⁻¹, we clearly observe I_d saturation at $|V_d| > 0.6$ V (**Figure 2.2**, right). This suggests that operating devices of P3HT-co-P3HHT in the saturation regime, where the output I_d approaches its maximum value, requires either higher potentials or much slower device operation, both of which can be impractical for real-life applications.

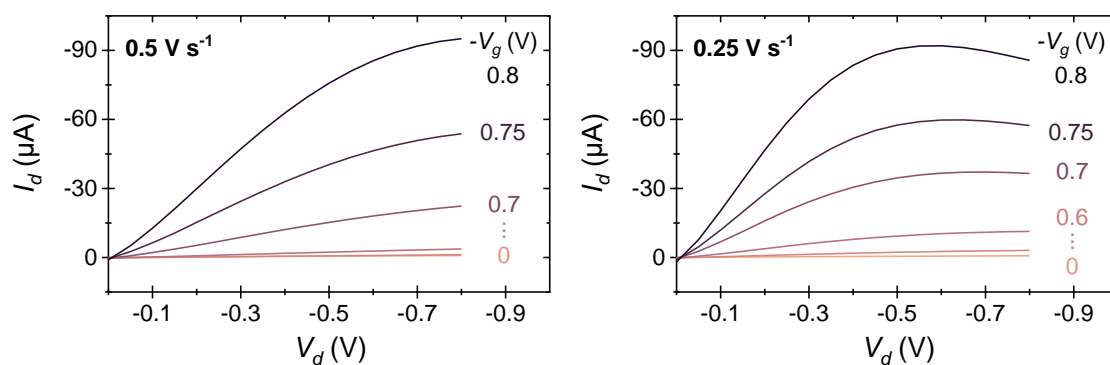


Figure 2.2. Output characteristics of an OECT with P3HT-co-P3HHT as the active channel material measured at a V_d sweep rate of 0.5 (left) and 0.25 $V s^{-1}$ (right) to show shift of onset of I_d saturation.

We obtain further evidence of slow response in devices of the neat P3HT-co-P3HHT from their transfer curves measured at various V_g sweep rates, plotted in **Figure 2.3**. At a constant V_d of -0.6 V and a cyclic sweep of V_g at a rate of 0.5 $V s^{-1}$, the measured I_d curves form large loops, indicating current hysteresis between the forward and reverse scans. Additionally, the maximum $|I_d|$ ($\approx 1 \mu A$) measured in these conditions appears to be even less than the maximum gate current, $|I_g|$ ($\approx 10 \mu A$), implying failed amplification. To remedy this, we operate the devices more slowly by decreasing the sweep rate to give enough time for the polymer to be doped with increasing bias. This results in steeper rise of I_d at distinct V_g onsets, marking the threshold gate voltages, V_t , at which devices transition from the “off” (low I_d , $V_g < V_t$) to “on” (high I_d , $V_g > V_t$) state. The device reaches up to 60 μA maximum I_d and “on” to “off” current ratios ($I_{ON/OFF}$) over two orders of magnitude for a V_g sweep rate of 0.01 $V s^{-1}$ at 50 mV increments, from which we estimate a response time of at least 5 seconds. However, even at these slow conditions, we observe in the logarithmic plot of the transfer curve (left panel of **Figure 2.3**) that the current hysteresis persists, which implies that the performance can still be improved with longer device operation. These results provide initial indications of inefficient mixed conductivity in P3HT-co-P3HHT involving slow

uptake of chloride ions, which are necessary to counterbalance the formation of charge bearing polarons and induce electronic conductivity across the device channel.

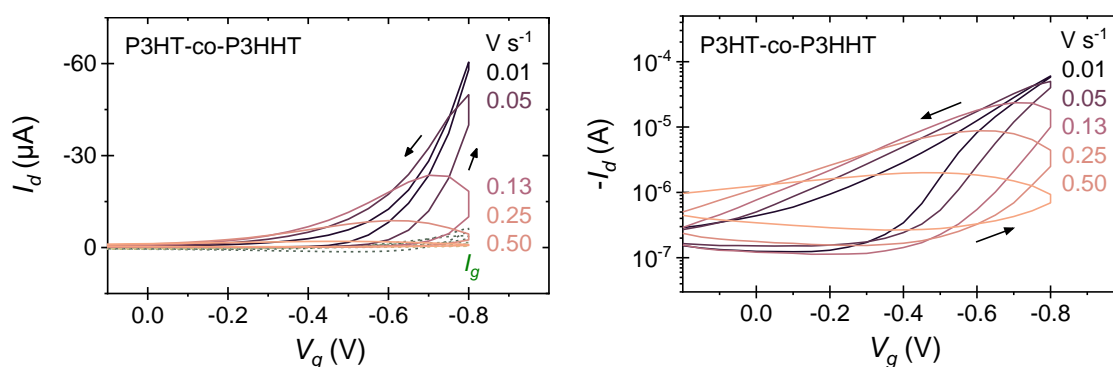


Figure 2.3. Transfer characteristics of an OECT with P3HT-co-P3HHT as channel material plotted linearly (left) and logarithmically (right), showing large I_d hysteresis and variation of $I_{ON/OFF}$ across various V_g sweep rates ($V s^{-1}$). Linearly plotted I_g is shown in dashed green lines.

2.2.2. Blends with P3HT-*b*-PEO

Next, we measure OECTs fabricated with a blend of P3HT-co-P3HHT and P3HT-*b*-PEO (25 wt%) as the active channel material. We observe that the devices exhibit electrical performance similar to those of the neat P3HT-co-P3HHT despite the addition of an electronically insulating PEO component into the channel. Plots of the OECT output and transfer characteristics of the blend given in **Figure 2.4** indicate that, like the neat material, the blend shows accumulation mode behavior in their devices, which is not surprising since the active semiconductor is the same. Additionally, the maximum I_d in devices of the blend approaches a value similar to that measured for the neat material, about 60 μA , which suggests that blending modification of the material does not really affect its electronic conductivity during device operation. However, unlike devices of the neat P3HT-co-P3HHT, OECTs of the blend could be operated at much faster speeds and yield high output currents.

For instance, the output curves of the blend measured at a V_g of -0.7 V and at a V_d sweep rate of 0.5 V s^{-1} (top panel, **Figure 2.4**) clearly show I_d saturation at V_d as low as -0.3 V in contrast with the Ohmic behavior observed in devices of P3HT-co-P3HHT at similar operating parameters. Likewise, better reproducibility of the currents is observed in the transfer curves of the blend compared to those of the neat material when operated over a wide range of V_g sweep rates. Devices of the blend show minimal hysteresis in the I_d loops and relatively consistent $I_{ON/OFF}$ even at sweep rates up to 10 V s^{-1} (see bottom-right panel of **Figure 2.4**).

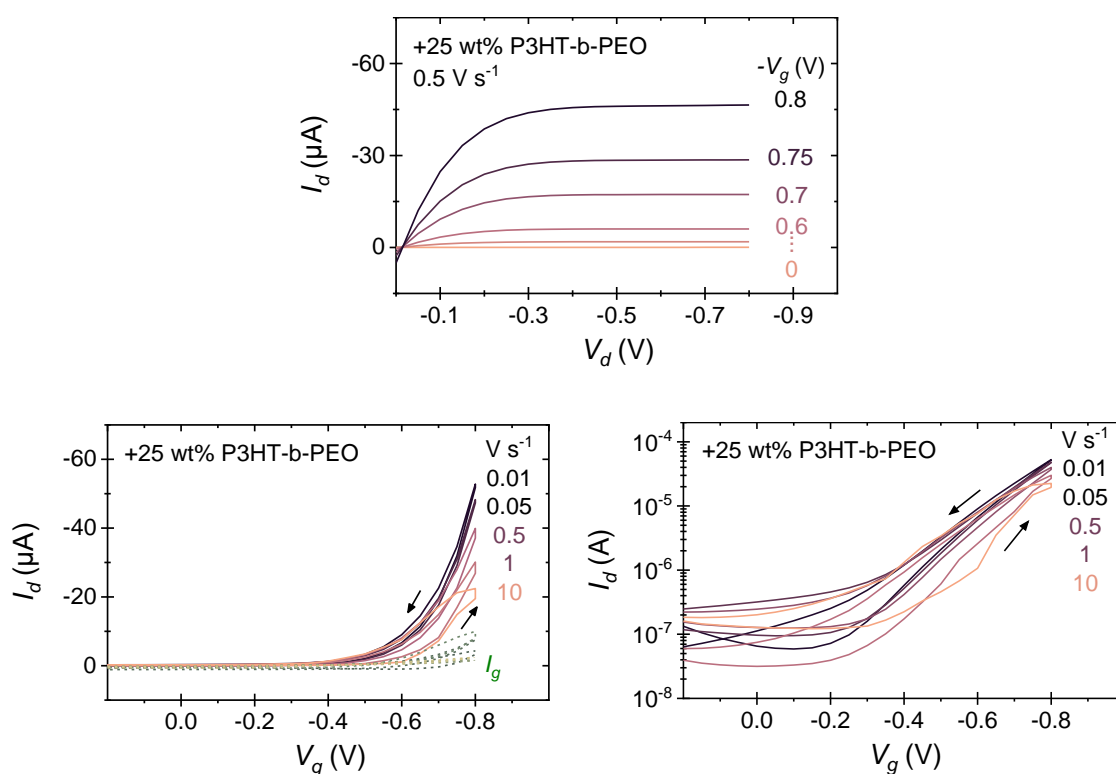


Figure 2.4. OECT output (top) and transfer characteristics (bottom) plotted linearly (left) and logarithmically (right) for a blend of P3HT-co-P3HHT with 25 wt% P3HT-b-PEO as active channel material measured at various V_g sweep rates (V s^{-1}), showing minimal hysteresis in the I_d loops and relatively similar $I_{ON/OFF}$.

2.2.3. OECT performance indicators, g_m and ΔV_t

The effects of operating speed and blending modification of the active mixed conductor on the OECT performance is highlighted further by carefully inspecting the quantities that indicate the magnitude of ion-to-electron signal transduction and I_d hysteresis observed in the transfer curves.

The transconductance, g_m , used as the figure-of-merit for OECTs, describes the transduction performance as the amount of change in I_d with change in V_g . This is obtained by differentiating the transfer curve, $\frac{\delta I_d}{\delta V_g}$.¹ **Figure 2.5** plots g_m obtained from the first derivative of the forward scan of the transfer curves measured at a sweep rate of 0.06 V s^{-1} for devices of P3HT-co-P3HHT and its blend with P3HT-*b*-PEO. At similar channel dimensions and relatively slow biasing conditions, we observe that the maximum transconductance, $g_{m,max}$, does not greatly differ between OECTs of the neat P3HT-co-P3HHT ($g_{m,max} \approx 0.3 \text{ mS}$) and its blend with P3HT-*b*-PEO ($g_{m,max} \approx 0.4 \text{ mS}$).

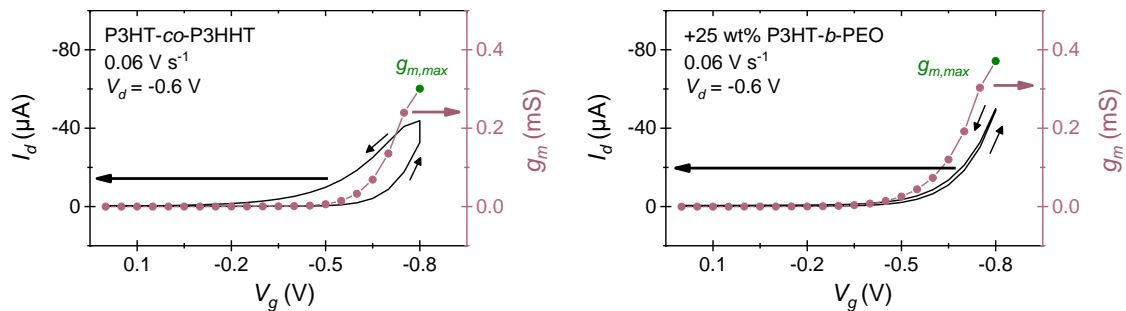


Figure 2.5. First derivatives (pink line-and-symbol plots, right axis) of OECT transfer curves (black lines, left axis) yielding the transconductance plots (g_m) for neat P3HT-co-P3HHT (right) and its blend with 25 wt% P3HT-*b*-PEO (left), showing almost similar $g_{m,max}$.

We note that $g_{m,max}$ occurs at a V_g of -0.8 V in both devices, the highest magnitude of the biasing range chosen here. This is unlike devices of other mixed conductors like PEDOT:PSS² and p(g2T-TT)³ that show non-monotonic growth of g_m with V_g , which has been attributed to be the result of the intrinsic charge transport properties of disordered polymeric semiconductors.⁴ In our case, the “real” peak g_m may occur at higher V_g , however performing measurements at these conditions risks device degradation. Thus, for practical reasons, we consider the g_m at the maximum V_g of our biasing range as the $g_{m,max}$ for these devices.

To quantify the current hysteresis observed in the transfer curves, we use the difference between the threshold voltages in the forward and reverse scan, ΔV_t . The values of V_t are estimated by extrapolating the intercept of the line in plots of $|I_d|$ over V_g . This is in accordance with the definition of the OECT I_d in the saturation regime, $I_{d,sat}$, given in **Equation 2.1**.⁵

$$I_{d,sat} = \frac{Wd}{2L} \mu C^* (V_t - V_g)^2 \quad \mathbf{2.1}$$

Where μ and C^* is the hole mobility and volumetric capacitance of the channel material, respectively. As demonstrated in **Figure 2.6**, larger values of ΔV_t are measured for the device of P3HT-co-P3HHT, reflecting the lag of I_d due to slower rate of conductance change in the material relative to the V_g sweep rate. It follows that devices of the blend exhibiting less I_d lag show less ΔV_t .

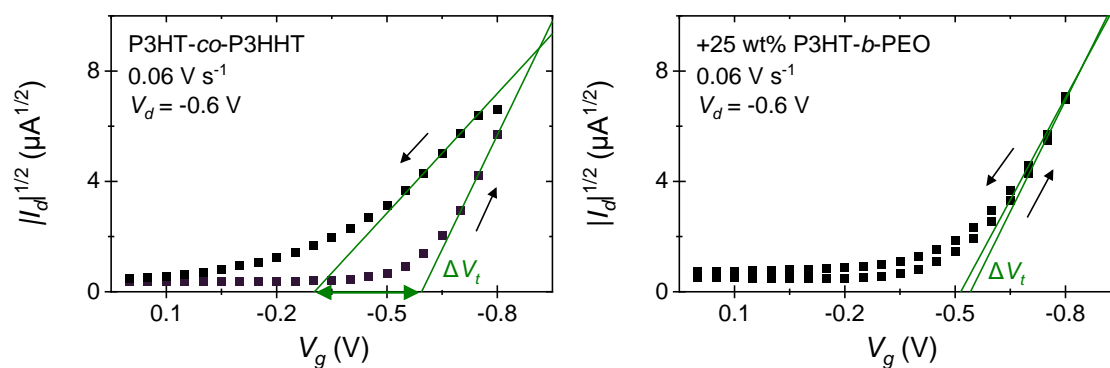


Figure 2.6. Extraction of the threshold voltage differences between the forward and reverse scans (ΔV_t) of transfer curves of neat P3HT-co-P3HHT (left) and its blend with 25 wt% P3HT-b-PEO (right), showing significantly less ΔV_t in the latter given similar biasing conditions.

All values of g_m and ΔV_t extracted from the transfer curves of each device measured at various sweep rates are plotted in **Figure 2.7** to show a comprehensive picture of how operating speed affects the device performance. Immediately apparent in these plots of g_m and ΔV_t over sweep rate is that the OECT of the blended material shows significantly better stability in performance over a wider range of operating speeds than the device of the neat material. At a gate voltage sweep rate of 0.01 V s^{-1} , the slowest speed employed in our range of measurements, the values of ΔV_t and $g_{m,max}$ extracted for P3HT-co-P3HHT and its blend with 25 wt% P3HT-b-PEO are similar, at about 30 mV and 0.4 mS, respectively. This suggests that blending modification does not actually change the steady state transduction performance of P3HT-co-P3HHT, possibly sustaining its electronic conductivity. Increasing the speed to around 0.1 V s^{-1} in devices of the neat material leads to an increase of the ΔV_t by an order of magnitude and a decrease in the $g_{m,max}$. When operating devices of the neat material at even faster sweep rates, between 0.1 to 1 V s^{-1} , the extrapolated ΔV_t approaches 1 V and $g_{m,max}$ significantly decreases by up to two orders of magnitude. This is a clear demonstration of how lagging I_d due to the slow reactivity of the mixed conductor significantly jeopardizes the transduction performance of OECTs. On the other hand, in

devices of the blend operated at sweep rates up to 1 V s^{-1} , low ΔV_t is maintained at about 60 mV and only a small decrease of the $g_{m,max}$ from 0.4 to 0.25 mS is observed. Even after increasing the speed to an unreasonably fast rate of 10 V s^{-1} the increase of ΔV_t and decrease of $g_{m,max}$ in devices of the blend are less than that observed for devices of the neat material when operated at a slower rate of 1 V s^{-1} . These results imply that blending modification of P3HT-co-P3HHT by adding the P3HT-*b*-PEO component significantly enhances the electrochemical reactivity of the mixed conductor to application of bias without altering its bulk electronic properties. Therefore, blending improves the stability of the OECT performance to varying operating speeds over a wide range of sweep rates while maintaining the magnitude of its transduction performance.

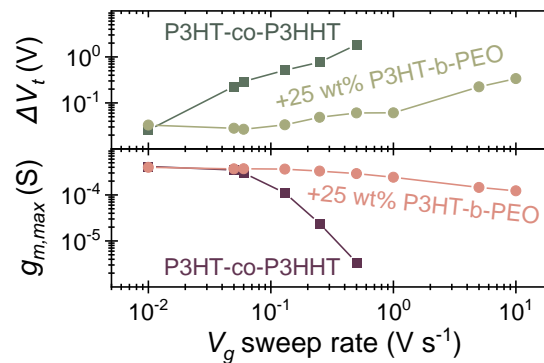


Figure 2.7. ΔV_t and $g_{m,max}$ plotted against V_g sweep rate for devices of P3HT-co-P3HHT and its blend with 25 wt% P3HT-*b*-PEO, showing more stable performance of the blend over a wider range of sweep rates.

2.3. Performance across different channel dimensions

We continue our investigation of OECTs based on P3HT-co-P3HHT and its blends with P3HT-*b*-PEO by testing devices with larger channel dimensions ($W = 2500 \mu\text{m}$, $L = 50, 110, 180, \text{ and } 360 \mu\text{m}$) to elucidate the factors of OECT behavior strongly influenced by

device geometry and to assess whether blending modification of the active channel material offers further control over the device performance independent of its size. We note that, for practical reasons, fabrication of the larger devices used in this work do not include deposition of an epoxy layer to insulate the source and drain contacts from the polymer film and electrolyte, resulting in a simpler architecture than that of the micro-scale devices. The OECT transfer curves of P3HT-co-P3HHT and its blends with P3HT-*b*-PEO at various $Wd L^{-1}$ measured at a V_d of -0.6 V are presented in **Figure 2.8**.

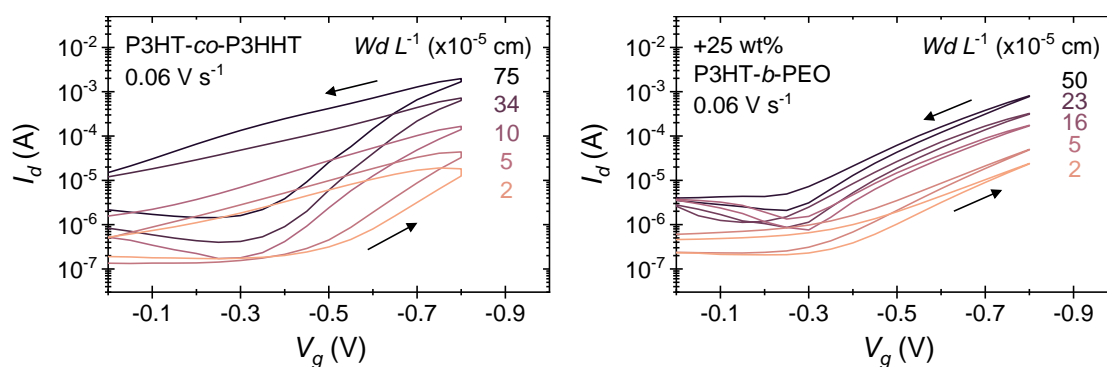


Figure 2.8. OECT transfer curves measured for devices of neat P3HT-co-P3HHT (left) and its blend with 25 wt% P3HT-*b*-PEO (right) at various channel dimensions (units given in cm for consistency with standard units of C^* , $F\text{ cm}^{-3}$).

Both materials show higher “on” currents in their devices with larger $Wd L^{-1}$, as expected for OECTs and predicted in **Equation 2.1**. We also note that the large-scale devices fabricated without insulated source and drain electrodes ($Wd L^{-1} > 5 \times 10^{-5}$ cm) show higher I_d in the “off” state, which might be the result of some leak currents. Nonetheless, $I_{ON/OFF}$ of at least two orders of magnitude are maintained. Furthermore, we consistently observe less hysteresis in the OECT transfer curves of the blends than in those of the neat material. Thus, while tuning the channel geometry effectively modulates the current magnitudes, it appears that only by modifying the active channel material itself can

the response speed of the devices be significantly manipulated. It follows then that higher values of g_m are measured in larger devices of both materials, while devices of the blends all show less ΔV_t than those of the neat P3HT-co-P3HHT, plotted in **Figure 2.9**.

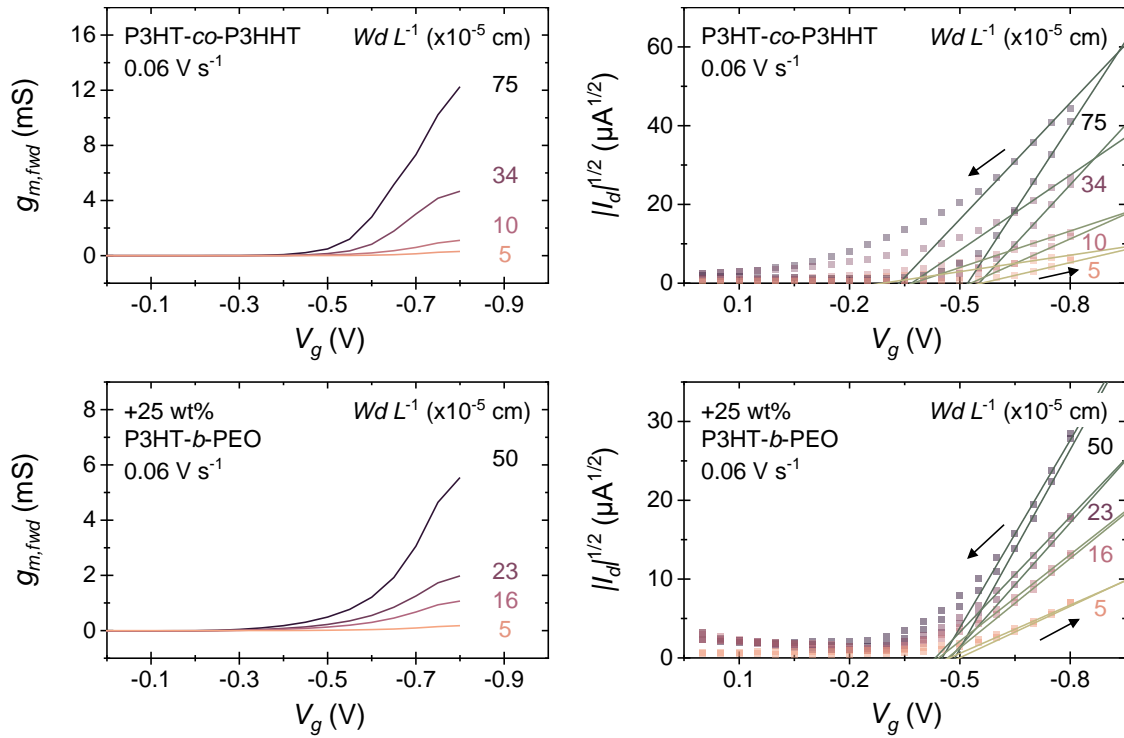


Figure 2.9. Plots of g_m (left) and $|I_d|^{1/2}$ to extrapolate threshold voltages (right) for OEECTs of neat P3HT-co-P3HHT (top) and its blend with 25 wt% P3HT-b-PEO (bottom) at various channel dimensions.

Although we do see modulation of the g_m with channel dimensions, we continue to observe its maximum value only at the highest V_g . This is unlike the reported behavior of PEDOT:PSS OEECTs, where the V_g at which devices exhibit maximum transconductance, $V_g(g_{m, max})$, can be shifted to lower potentials by as much as -0.3 V through decreasing channel thickness, from 640 to 25 nm, or by decreasing the width to length ratio, WL^{-1} , from 10 to 0.1.⁶ In our devices, the thicknesses only range from 80 to 160 nm, and the WL^{-1} from

2 to 50, thus it might be possible to more effectively tune $V_g(g_{m,max})$ by fabricating even smaller channel size scales. This would however result in lower magnitudes of g_m and was therefore not explored further in this work. Likewise, the values of V_t do not change significantly in devices of similar channel material, and a difference of only 0.1 V in the $V_{t, fwd}$ is observed between OECTs of P3HT-co-P3HHT and its blend with P3HT-*b*-PEO, likely caused by the difference in I_d lag. This might suggest that the energetics required to electrochemically dope the conjugated polymer and operate the OECTs is not largely sensitive to channel size and blending modification of the material.

2.3.1. Channel material performance indicator, μC^*

Figure 2.10 shows that the values of g_m measured from several devices of the neat P3HT-co-P3HHT and its blend with P3HT-*b*-PEO at various sweep rates scale with the product of WdL^{-1} for a similar gate bias, $|V_t - V_g|$, of about 0.2 V.

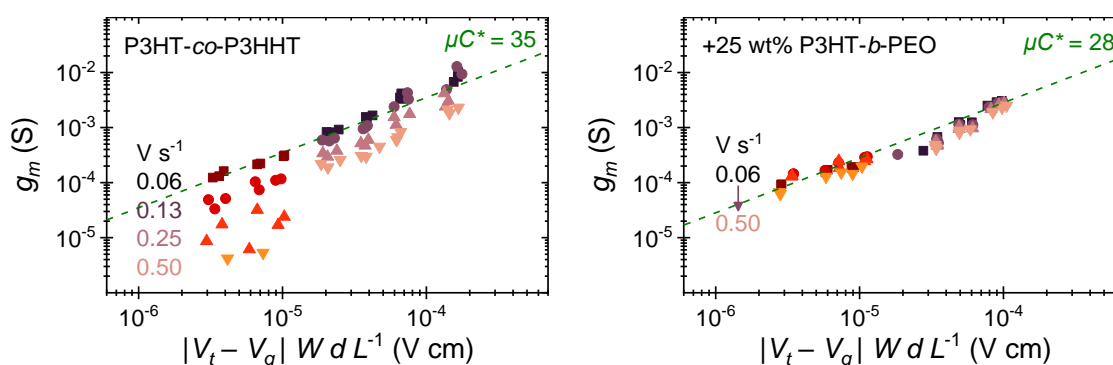


Figure 2.10. Scaling of g_m with $|V_t - V_g| W d L^{-1}$ for OECTs of neat P3HT-co-P3HHT (left) and its blend with 25 wt% P3HT-*b*-PEO (right) at various V_g sweep rates. Data for micro-OECTs are plotted in red gradient while the rest correspond to large-scale OECTs. μC^* extracted from model fits (dashed green line) is shown.

This is in accordance with the transconductance equation for OECTs described in literature and given in **Equation 2.2**.

$$g_m = \mu C^* (|V_t - V_g|) (Wd/L) \quad 2.2$$

Note that this is derived from solving the first derivative of $I_{d,sat}$ in **Equation 2.1** with respect to V_g .⁵ It is therefore interesting to extract the μC^* product, often used as the materials-system figure-of-merit for OECTs independent of device geometry and bias, from the slope of g_m plotted against $|V_t - V_g| WdL^{-1}$.⁷ However, due to the lagging current response in devices of the neat P3HT-co-P3HHT, we obtain largely dispersed values of g_m across sweep rates (**Figure 2.10**, left). As a result, the extracted slopes significantly deviate depending on the operating speed used, from 10 to 55 F cm⁻¹ V⁻¹ s⁻¹, averaging at about 35 F cm⁻¹ V⁻¹ s⁻¹. We note that this matches the performance of the P3HHT homopolymer measured in previous work using similar OECT architecture,⁸ which implies that only a fraction of polar sidechain substitution is necessary to maximize the mixed conducting performance of the polythiophene operating in aqueous electrolyte. However, although these results imply that the neat P3HT-co-P3HHT can potentially exhibit higher gain with slower device operation, these conditions are not necessarily practical for certain target applications requiring sharp off-to-on current response. This also highlights the importance of measurement speed when evaluating mixed conductor performance. Contrastingly, significantly less dispersed g_m is obtained from devices of the blend (**Figure 2.10**, right) due to better stability of its performance over a wider range of sweep rates. Consequently, an average slope of 28 F cm⁻¹ V⁻¹ s⁻¹ is calculated, well within the range of that of the neat material.

2.3.2. Influence of channel dimensions on current hysteresis

The Bernard's model depicts the OECT transient behavior as a charging capacitor with an RC time constant, τ , proportional to $d(WL)^{1/2}$,^{9,10} suggesting that smaller channel width and thickness should improve the device response speed. However, upon closer inspection of the ΔV_t , which we assume is proportional to the device response time, measured in several devices of P3HT-*co*-P3HHT and its blend with P3HT-*b*-PEO, we find it difficult to observe any significant scaling when plotted over each channel dimension in

Figure 2.11.

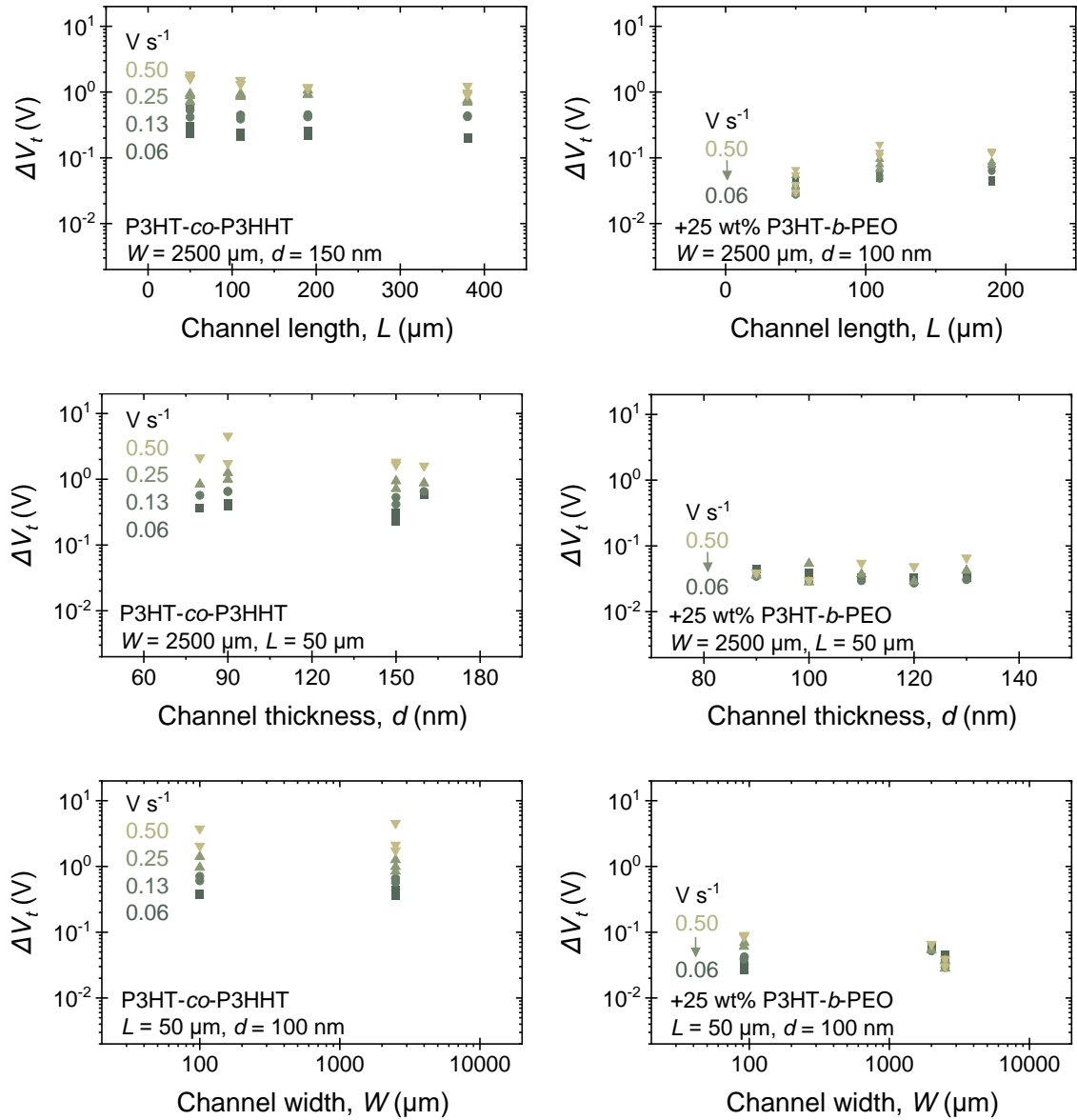


Figure 2.11. ΔV_t measured for various devices of neat P3HT-co-P3HHT plotted against the OECT channel length (top), thickness (middle), and width (bottom), showing no significant variation across each dimension at a given V_g sweep rate.

This shows that tuning the channel geometry within the range investigated here is not a highly effective method to minimize the I_d hysteresis observed in devices of the neat material. On the other hand, we could decrease the sweep rates from 0.5 to 0.06 V s^{-1} to reduce the I_d lag in all devices of P3HT-co-P3HHT and lower ΔV_t from 2 V to about 0.2 V, but this value is still quite large considering that OECTs typically operate at $V_g < 1 \text{ V}$.

Fortunately, despite the limited effects of tuning the device parameters, we can further minimize ΔV_t to values even less than 0.1 V simply by adding P3HT-*b*-PEO to the channel. Since we observe no significant influence of the channel dimensions on ΔV_t , we quantify the general hysteresis measured in devices of each material by calculating the average value over channel volume. **Figure 2.12** plots ΔV_t over channel volume, the data yielding average $\Delta V_t \approx 0.3 - 1.5$ V for devices of the neat P3HT-*co*-P3HHT and average $\Delta V_t \approx 0.04 - 0.08$ V for that of its blend with P3HT-*b*-PEO across V_g sweep rates of 0.06 – 0.5 V s⁻¹.

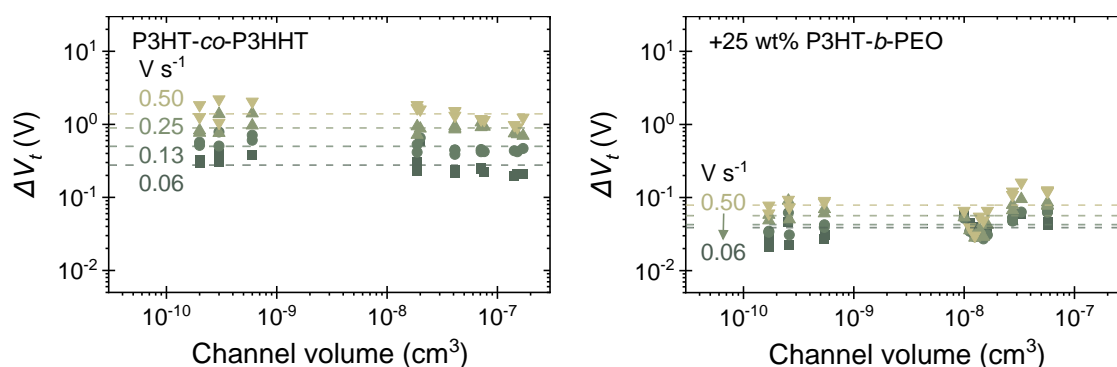


Figure 2.12. ΔV_t plotted against the OECT channel volume for various devices of neat P3HT-*co*-P3HHT (left) and its blend with 25 wt% P3HT-*b*-PEO (right).

2.4. Performance across blend composition

We further investigate the extent at which blending effectively tunes the performance of the OECTs by varying the “additive” content. **Figure 2.13** shows the transfer characteristics, $g_{m, fwd}$ and ΔV_t of OECTs of blends with various P3HT-*b*-PEO content.

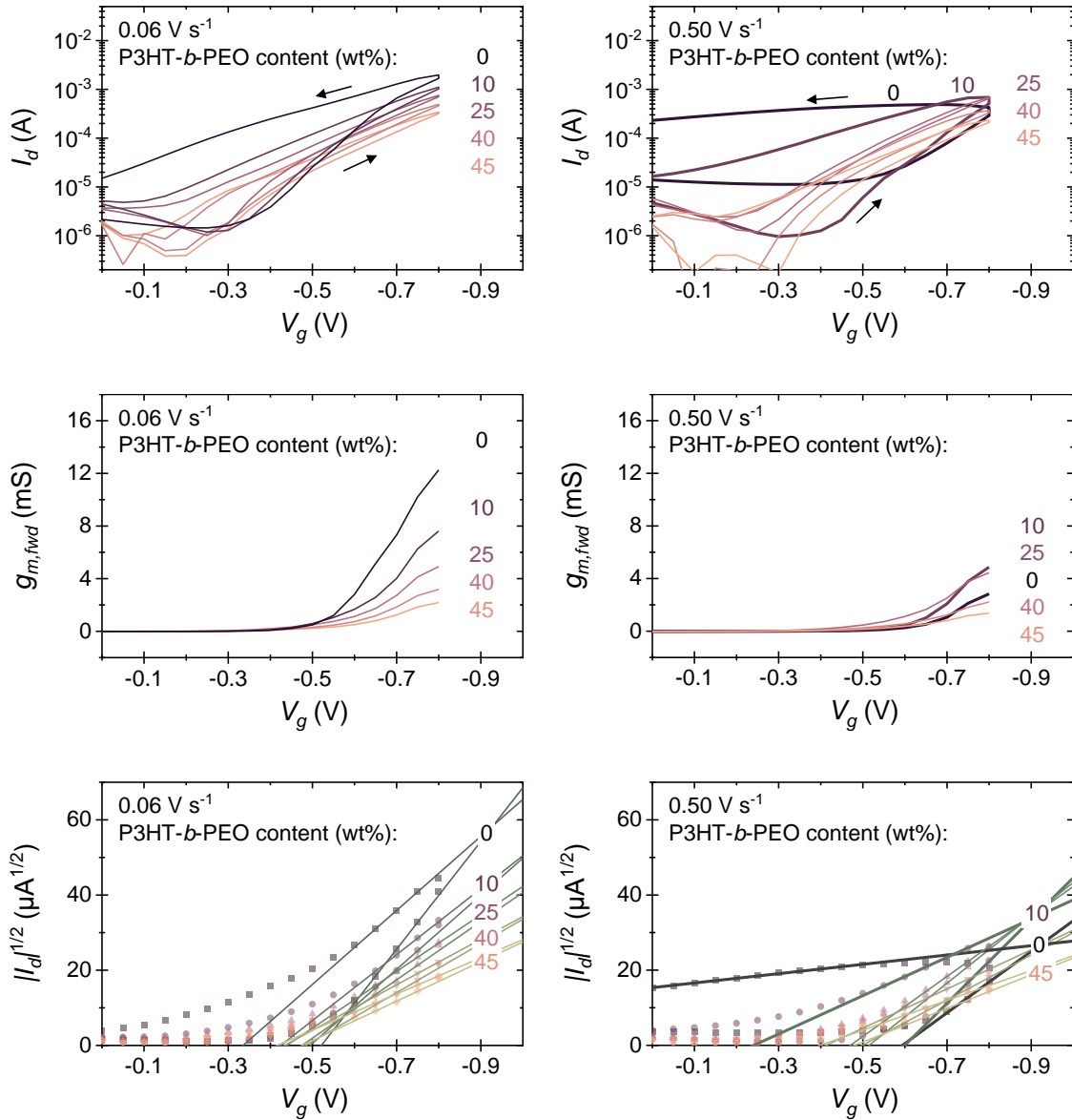


Figure 2.13. Transfer curves (top), plots of g_m (middle), and $|I_d|^{1/2}$ to extrapolate V_t (bottom) for OECTs of P3HT-co-P3HHT and its blends with P3HT-b-PEO at various indicated compositions, operated at sweep rates of 0.06 V s^{-1} (left) and 0.50 V s^{-1} (right). Behavior of the neat material and the 10 wt% blend significantly changes at higher sweep rates (bold lines). All devices compared hold similar channel dimensions ($W = 2500 \mu\text{m}$, $L = 50 \mu\text{m}$, $d = 120 \pm 20 \text{ nm}$).

At a slow sweep rate of 0.06 V s^{-1} , we see that increasing the P3HT-b-PEO content from 0 to 45 wt% leads to progressively lower $I_{d,max}$ and, subsequently, $g_{m,max}$, while also reducing the ΔV_t . Meanwhile, $V_{t,fwd}$ does not seem to change significantly, verifying that

blending does not affect the energy needed for hole and/or ion injection even at higher compositions. Upon increasing the sweep rate to 0.50 V s^{-1} , both the neat material and its blend at 10 wt% P3HT-*b*-PEO show larger hysteresis in the transfer curves, yielding lower $g_{m, fwd}$ and larger ΔV_t , while the behavior of the blends at higher block copolymer content do not change significantly, maintaining I_d and g_m magnitudes comparable to that of the neat material. This confirms that the electronic properties of the neat material are not lost even after blending. Similar trends are observed upon extracting the μC^* product and average ΔV_t for several devices of different channel dimensions and blend composition, shown in **Figure 2.14** and **Figure 2.15**.

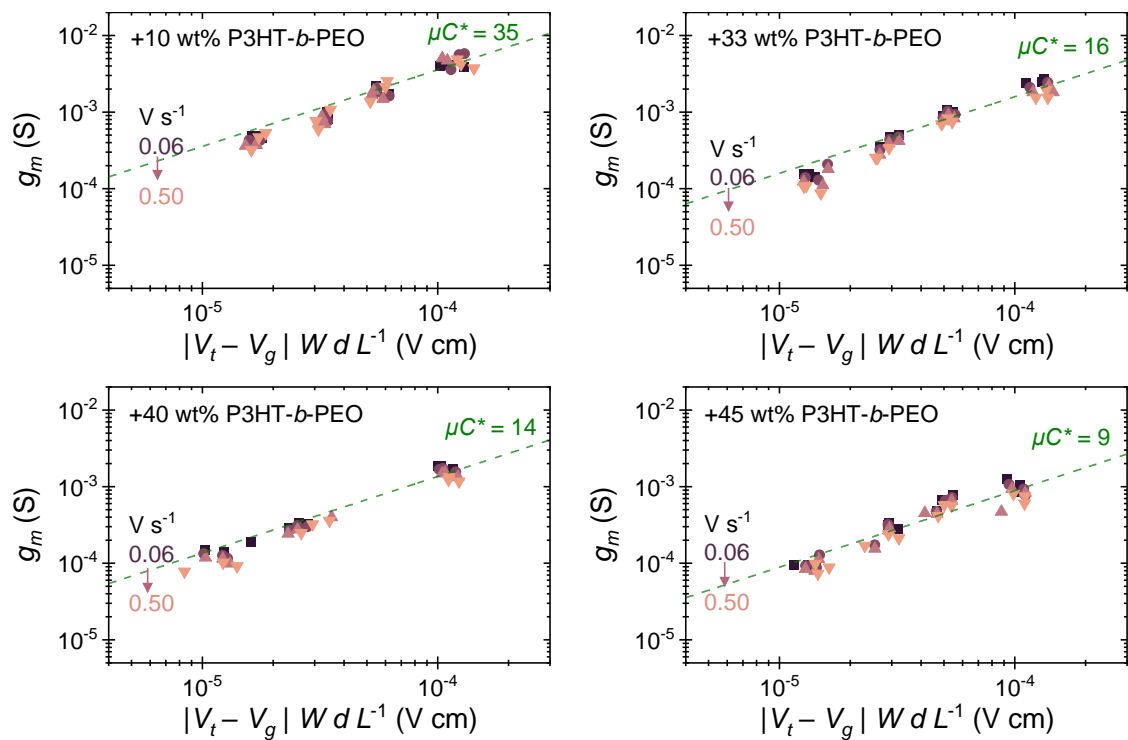


Figure 2.14. Scaling of g_m with $|V_t - V_g| W d L^{-1}$ for OECTs of blends of P3HT-co-P3HHT and P3HT-*b*-PEO at various indicated compositions and V_g sweep rates. Average μC^* extracted from model fits (dashed green line) is labelled.

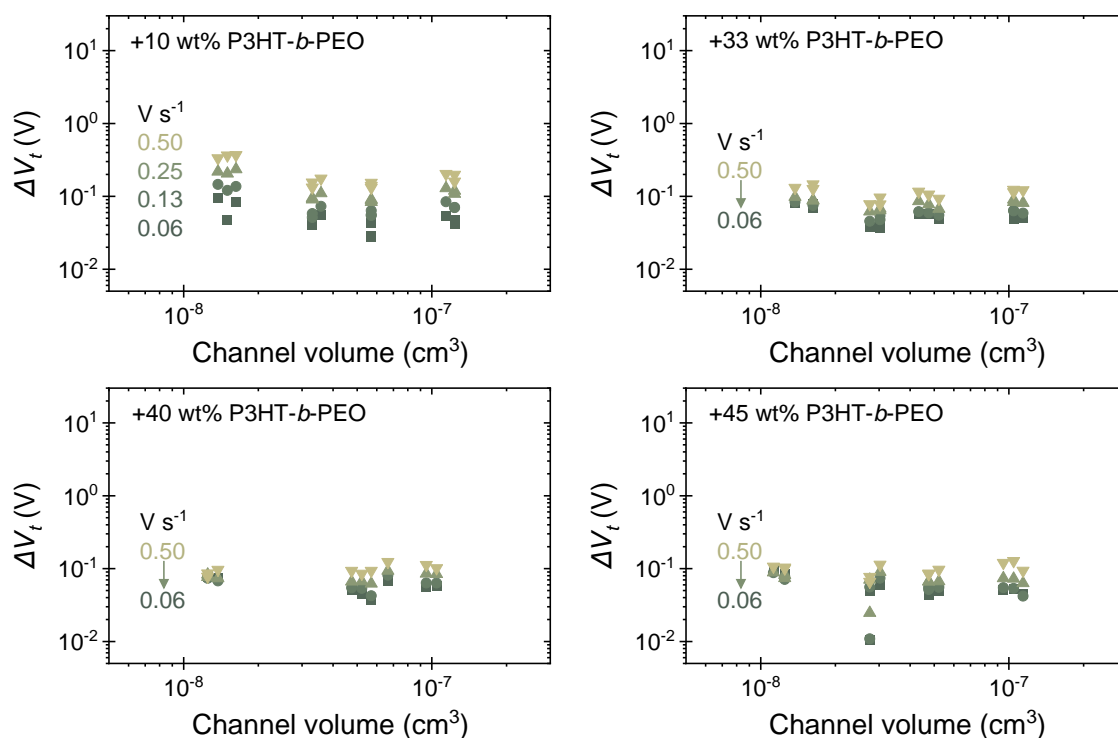


Figure 2.15. ΔV_t plotted against the OECT channel volume for various devices of blends of P3HT-*co*-P3HHT and P3HT-*b*-PEO at the indicated compositions.

The lower g_m generally observed in higher blend compositions is also reflected in their μC^* values, showing 35, 16, 14, and 9 F cm⁻¹ V⁻¹ s⁻¹ for 10, 33, 40 and 45 wt% P3HT-*b*-PEO content, respectively. Nonetheless, only small variation of the μC^* across V_g sweep rates is observed in the blends due to the enhanced response speed of their devices, and even at the highest blend composition of 45 wt% P3HT-*b*-PEO, the magnitude of transduction is still close to that of the neat material measured at high speed. The ΔV_t data shows that at compositions greater than 25 wt% P3HT-*b*-PEO, the hystereses in the transfer curves are not further reduced, yielding a minimum $\Delta V_t \approx 0.05$ V that can be achieved by both blending and decreasing device operating speed. These results are compiled in **Figure 2.16**, which plots the average values of μC^* and ΔV_t measured for devices of each blend composition at given sweep rates.

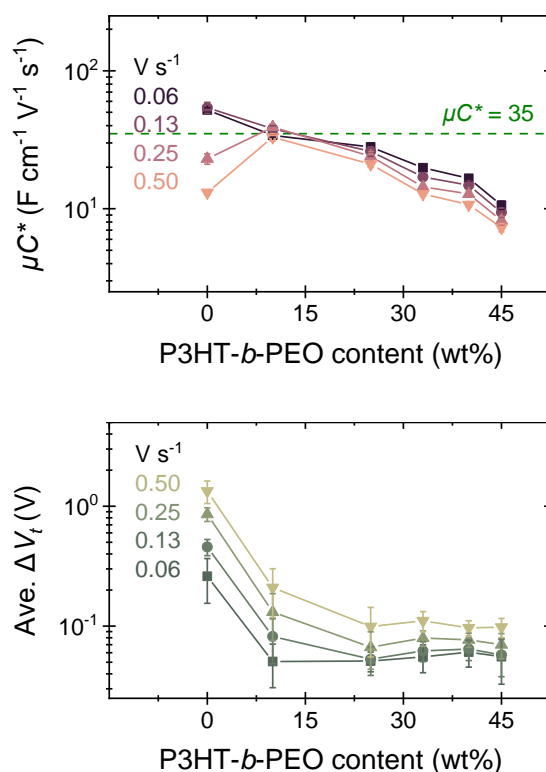


Figure 2.16. Summary of μC^* (top) and average gate threshold voltage difference (ave. ΔV_t) (bottom) extracted for various blend compositions at indicated scan rates. Average μC^* extracted for neat P3HT-co-P3HHT is labelled (dashed green line) for reference.

This summary offers a sample guideline to how tuning the blend composition can effectively tailor the overall performance of the OECT to meet conditions of specific applications. In cases where slightly enhanced response speed is desired but maximizing the current magnitude of devices is still prioritized, as little as 10 wt% P3HT-*b*-PEO can be added to reduce the I_d lag while maintaining the average μC^* parameter of the neat material, $35\ F\ cm^{-1}\ V^{-1}\ s^{-1}$. Otherwise, blends of 25 wt% P3HT-*b*-PEO can be prepared to minimize the response time as low as possible while still showing high μC^* of $28\ F\ cm^{-1}\ V^{-1}\ s^{-1}$. To economize the quantity of active mixed conductor used, we can choose to employ blends with P3HT-*b*-PEO content up to 40 wt% and still achieve better transduction performance than the neat material at faster operating speeds.

2.5. Transient response

We've shown so far that blending P3HT-*co*-P3HHT with P3HT-*b*-PEO can effectively reduce the drain current lag observed in the transfer curves of their OECTs while fairly sustaining their transconductances, and thus assumed that these devices should also show faster response times with high on-to-off current ratios. The results presented in this section confirm that we do indeed obtain shorter time constants in the transient drain currents of these devices upon application of a gate potential. Our micro-scale OECTs ($W = 100 \mu\text{m}$ and $L = 10 \mu\text{m}$) were chosen for these measurements to conform with the prediction that $\tau \sim d(WL)^{1/2}$, while the presence of the insulating layer might help minimize additional resistive elements that could affect the transient behavior. We limit our investigation to the performances of the neat material and its blend with 25 wt% P3HT-*b*-PEO, which appears to be the optimum composition to maximize μC^* and minimize ΔV_t .

2.5.1. Response to a V_g pulse

The transient drain currents in response to a V_g step are measured in devices of the neat P3HT-*co*-P3HHT and its blend with P3HT-*b*-PEO, plotted in Figure **Figure 2.17**. V_d is limited to -0.4 V and V_g is limited to -0.6 V (-1 V total potential) to prevent rapid degradation of the devices during longer periods of biasing.

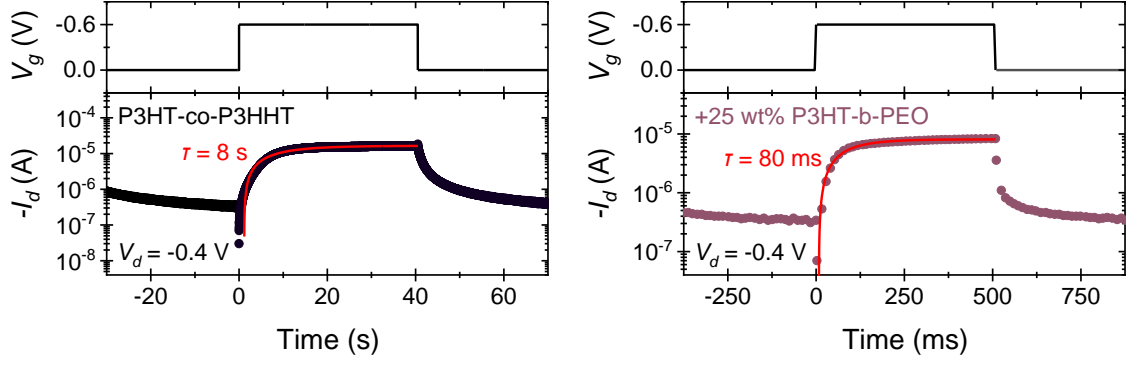


Figure 2.17. I_d over time upon applying a V_g pulse measured for OECTs of neat P3HT-co-P3HHT (left) and its blend with 25 wt% P3HT-b-PEO (right) of similar channel dimensions ($W = 100 \mu\text{m}$, $L = 10 \mu\text{m}$, $d = 100 \pm 10 \text{ nm}$). Time constants extracted from exponential fits (red solid line) are labeled.

The data is fitted with an exponential model to extract the ionic time constants, τ , in accordance with the definition of the OECT transient current under constant gate voltage, given in **Equation 2.3**.^{9,11}

$$I_d(t, V_g) = I_{SS}(V_g) + \Delta I_{SS} \left(1 - f \frac{\tau_e}{\tau_i} \right) e^{-\left(\frac{t}{\tau}\right)} \quad \mathbf{2.3}$$

Where I_{SS} refers to steady state drain current measured at saturation during a V_g step, ΔI_{SS} is the total change in current between that at zero V_g and that at the step potential, τ_e is the electronic time constant, and f is a geometric factor that accounts for the complex, non-uniform distribution of I_d at the source and drain electrodes depending on V_g and V_d . In both devices the values of I_{SS} are relatively equal at about $10 \mu\text{A}$ given similar biasing conditions and channel dimensions, confirming once again that blending does not change the conductivity of the material. Meanwhile, we determine $\tau \approx 8 \text{ s}$ for devices of the neat material and $\tau \approx 80 \text{ ms}$ for that of its blend, which approximately translates to cut-off frequencies, $f_c = (2\pi\tau)^{-1}$, around 0.02 Hz and 2 Hz , respectively. We note that, even after blending, the f_c we predict is low compared to that measured for the homopolymer P3HHT, with $f_c = 75 \text{ Hz}$,⁸ and even lower relative to state-of-the-art OECTs of accumulation-mode p(g2T-TT) ($f_c \approx 1$

kHz)³ and depletion-mode PEDOT:PSS (f_c reaching as high as 10 kHz).¹² We could possibly increase f_c further by modifying device parameters such as the applied drain bias¹³ or changing the transistor architecture itself,^{12,14,15} however this is beyond the scope of this work. What our results do show is the decrease of the response time by two orders of magnitude upon blending, which indicates that adding P3HT-*b*-PEO to P3HT-*co*-P3HHT enhances its ionic mobility.

2.5.2. Response to various V_g waveforms

We further demonstrate the enhanced transient performance in OECTs of the blend by measuring their I_d response to square, saw, and asymmetric triangle V_g inputs. Each measurement plotted in **Figure 2.18** clearly demonstrates superior signal detection in OECTs of the blend over those of the neat material. Owing to its faster response speed, the drain currents in devices of the blend can almost replicate the different waveforms with significantly less distortion than that of the neat material and at higher I_d magnitudes. The I_d transient in response to a symmetric triangle wave (top-right in **Figure 2.18**) shows the best quality of reproduced signal owing to the gradual rise and fall of the input V_g , in contrast with the sharp steps of the square wave input (top-left in **Figure 2.18**). We also observe that application of a sawtooth-type asymmetric triangle wave (bottom-left in **Figure 2.18**), where V_g is ramped up and then stepped back down to the initial value, yields sharper I_d peaks than those resulting from application of an inverse sawtooth triangle wave (bottom-right in **Figure 2.18**). This highlights faster discharging of the OECTs, which further implies easily reversible doping behavior in the channel material. Overall, these results provide a proof-of-concept on how a simple blending technique can drastically enhance the response speed of initially “slow” polymer mixed conductors, rendering them more suitable for applications requiring fast operation, for example, in biosensing¹⁶ or neuromorphic memory devices.¹⁷

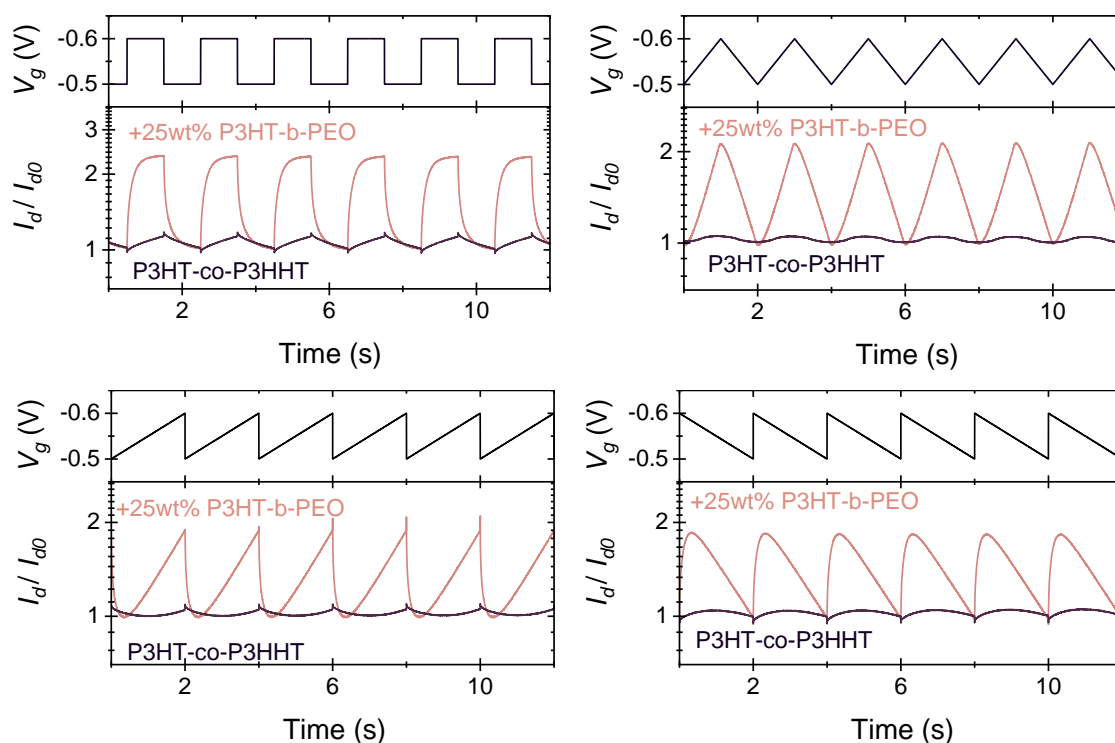


Figure 2.18. Normalized I_d over time upon applying various V_g waveforms (square, saw, and asymmetric triangle waves) measured for OECTs of neat P3HT-co-P3HHT and its blend with 25 wt% P3HT-b-PEO at similar channel dimensions ($W = 100 \mu\text{m}$, $L = 10 \mu\text{m}$, $d = 100 \pm 10 \text{ nm}$).

2.6. Summary

We characterize OECTs of P3HT-co-P3HHT and its blends with P3HT-b-PEO to evaluate the impact of blending modification of the mixed conductor on the performance of its electrochemical devices. Devices of neat P3HT-co-P3HHT exhibit slow response speeds indicated by the large I_d hysteresis in their transfer curves (I_d vs V_g) and long response time ($\tau = 8 \text{ s}$) extracted from the I_d transients (I_d vs t) upon application of a step potential. As a result, the transduction performance of the OECTs of P3HT-co-P3HHT, indicated by g_m , is highly sensitive to operating speed within the range of parameters investigated here, decreasing by over two orders of magnitude when the V_g sweep rate is increased from 0.1 to 1 V s^{-1} . Similar behavior is also observed in devices of various channel dimensions, which

implies that the slow device response is intrinsic to the channel material. Consequently, the μC^* parameter, used as the material-specific figure-of-merit to describe the performance of the OECT channel material and is obtained from characterizing several devices of different channel sizes, varies greatly within the range of sweep rates employed here. The values of μC^* extracted for P3HT-co-P3HHT range from 10 to 55 F cm⁻¹ V⁻¹ s⁻¹ (measured at sweep rates of 0.5 to 0.06 V s⁻¹), averaging at about 35 F cm⁻¹ V⁻¹ s⁻¹. These results suggest that the charge injection kinetics involved in electrochemically doping P3HT-co-P3HHT during device operation is slow. This also highlights the importance to consider temporal resolution when evaluating the performance of particularly “slow” mixed conductors. On the other hand, upon blending P3HT-co-P3HHT with 25 wt% P3HT-*b*-PEO, the devices exhibit faster response speeds indicated by the minimized I_d hysteresis in their transfer curves and relatively short response time ($\tau = 80$ ms). It follows that the g_m values of the devices of the blend are stable over a wide range of V_g sweep rates, even up to 10 V s⁻¹. Upon investigating blends of various compositions, we found that only 25 wt% P3HT-*b*-PEO is needed to effectively minimize the hysteresis in the transfer curves while maintain a high μC^* of 28 F cm⁻¹ V⁻¹ s⁻¹. However, even up to 40 wt% P3HT-*b*-PEO could be added to the material and still achieve a μC^* of 14 F cm⁻¹ V⁻¹ s⁻¹, still greater than that of the neat P3HT-co-P3HHT when operated at a fast sweep rate of 0.5 V s⁻¹. Overall, the results of this chapter show that blending P3HT-co-P3HHT with P3HT-*b*-PEO can effectively enhance the response speed of its OECTs without greatly affecting its steady state performance.

2.7. References

1. Rivnay, J. *et al.* Organic electrochemical transistors. *Nat. Rev. Mater.* **3**, 17086 (2018).
2. Khodagholy, D. *et al.* High transconductance organic electrochemical transistors. *Nat. Commun.* **4**, 1–6 (2013).
3. Giovannitti, A. *et al.* Controlling the mode of operation of organic transistors through

- side-chain engineering. *Proc. Natl. Acad. Sci.* **113**, 12017–12022 (2016).
4. Friedlein, J. T. *et al.* Influence of disorder on transfer characteristics of organic electrochemical transistors. *Appl. Phys. Lett.* **111**, 023301 (2017).
 5. Rivnay, J. *et al.* High-performance transistors for bioelectronics through tuning of channel thickness. *Sci. Adv.* **1**, e1400251–e1400251 (2015).
 6. Rivnay, J. *et al.* Organic Electrochemical Transistors with Maximum Transconductance at Zero Gate Bias. *Adv. Mater.* **25**, 7010–7014 (2013).
 7. Inal, S., Malliaras, G. G. & Rivnay, J. Benchmarking organic mixed conductors for transistors. *Nat. Commun.* **8**, 1767 (2017).
 8. Nicolini, T. *et al.* A Low-Swelling Polymeric Mixed Conductor Operating in Aqueous Electrolytes. *Adv. Mater.* **33**, 1–7 (2021).
 9. Bernards, D. A. & Malliaras, G. G. Steady-state and transient behavior of organic electrochemical transistors. *Adv. Funct. Mater.* **17**, 3538–3544 (2007).
 10. Friedlein, J. T., McLeod, R. R. & Rivnay, J. Device physics of organic electrochemical transistors. *Org. Electron.* **63**, 398–414 (2018).
 11. Faria, G. C., Duong, D. T. & Salleo, A. On the transient response of organic electrochemical transistors. *Org. Electron. physics, Mater. Appl.* **45**, 215–221 (2017).
 12. Donahue, M. J. *et al.* High-Performance Vertical Organic Electrochemical Transistors. *Adv. Mater.* **30**, 1705031 (2017).
 13. Friedlein, J. T., Donahue, M. J., Shaheen, S. E., Malliaras, G. G. & McLeod, R. R. Microsecond Response in Organic Electrochemical Transistors: Exceeding the Ionic Speed Limit. *Adv. Mater.* **28**, 8398–8404 (2016).
 14. Spyropoulos, G. D., Gelinas, J. N. & Khodagholy, D. Internal ion-gated organic electrochemical transistor: A building block for integrated bioelectronics. *Sci. Adv.* **5**, eaau7378 (2019).
 15. Polyravas, A. G. *et al.* Effect of channel thickness on noise in organic electrochemical transistors. *Appl. Phys. Lett.* **117**, 073302 (2020).
 16. Gualandi, I. *et al.* Selective detection of dopamine with an all PEDOT:PSS Organic Electrochemical Transistor. *Sci. Rep.* **6**, 1–10 (2016).
 17. Yamamoto, S. & Malliaras, G. G. Controlling the Neuromorphic Behavior of Organic Electrochemical Transistors by Blending Mixed and Ion Conductors. *ACS Appl. Electron. Mater.* **2**, 2224–2228 (2020).

CHAPTER 3:

Modulation of electrochemical doping kinetics *via* blending

3.1. Introduction	109
3.2. Physical properties of P3HT- <i>co</i> -P3HHT blended with P3HT- <i>b</i> -PEO.....	109
3.2.1. Solid-state structure	109
3.2.2. Thermal properties	112
3.2.3. Surface polarity	117
3.3. Electrochemical properties	118
3.3.1. Cyclic Voltammetry.....	118
3.3.2. Spectroelectrochemistry	122
3.3.2.1. Electrochemical bleaching	123
3.3.2.2. Electrochemical doping rates.....	125
3.3.2.3. Monophasic exponential kinetic model	127
3.3.2.4. Biphasic exponential kinetic model	128
3.3.3. Impedance behavior.....	130
3.3.3.1. Equivalent circuit model-fitting	133
3.3.3.2. Volumetric capacitance, C^*	136
3.4. Summary	137
3.5. References.....	138

3.1. Introduction

Blending-modification of P3HT-co-P3HHT with P3HT-*b*-PEO can significantly enhance the response speed of its OECTs without compromising its steady state characteristics and μC^* parameter. We suspect that the improved transient performance of the OECT is due to the increased hydrophilicity of the channel material upon adding PEO, which would support more efficient interdiffusion of ions between the polymer film and the external aqueous electrolyte. We also suspect that the P3HT-block chemically linked to the PEO will limit phase separation to microscales and lead to macroscopically uniform distribution of the components. This might help maintain the bulk electrical properties of the material, which would explain the relatively sustained transconductances of the OECTs even after blending. To explore these notions further, we investigate how blending, using the same methodology as that employed in OECT fabrication (detailed in appendix section **A.1 Materials and film deposition**), affects the physical and electrochemical properties of the material. Results provide some evidence of compatibility in the blends with the block copolymer despite phase separation. Also, it appears that our blending strategy primarily influences ionic transport in the mixed conductor leading to modulation of its electrochemical doping kinetics. On the other hand, blending does not seem to change the steady state electrochemical properties of the material relative to that of the neat P3HT-co-P3HHT. These findings agree with the trends observed in the performance of the OECTs.

3.2. Physical properties of P3HT-co-P3HHT blended with P3HT-*b*-PEO

3.2.1. Solid-state structure

We begin by examining how incorporation of P3HT-*b*-PEO influences the solid-state structure of P3HT-co-P3HHT since this can have consequences on its electronic properties. Inspection of the UV-Vis absorbance spectra of the films in **Figure 3.1** gives insight into the

impact of blending on the local molecular order of the conjugated polythiophene segments. We observe distinct features attributed to the 0-0 and 0-1 vibronic transitions (A_{0-0} and A_{0-1}) associated with exciton coupling between locally ordered π -stacks (interchain coupling) and between conjugated segments along the polymer backbone (intrachain coupling), which indicate short-range order in conjugated polymers in the form of molecular aggregates.¹⁻³ Blending with different P3HT-*b*-PEO compositions (0-45 wt%) results in identical absorbance maxima at $\lambda \approx 560$ nm and only slight differences in the 0-1/0-0 vibronic peak ratios (A_{0-0}/A_{0-1}). This suggests that the aggregation behavior and related optoelectronic properties of P3HT-*co*-P3HHT do not change with addition of P3HT-*b*-PEO. This may be attributed to phase-separation of the components, which minimizes interaction of the PEO segments with the polythiophene backbone, rendering the optoelectronic properties of the latter virtually unaffected.²

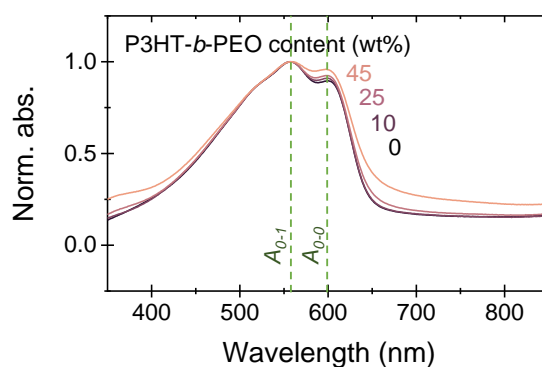


Figure 3.1. UV-Vis absorption spectra of P3HT-*co*-P3HHT and its blends with P3HT-*b*-PEO. No significant change in the A_{0-0}/A_{0-1} ratio implies that blending does not strongly influence the short-range aggregation behavior of P3HT-*co*-P3HHT.

Results from GIWAXS analysis (measurements and data processing performed by Dr. Tommaso Nicolini) corroborate the picture of phase separation in the blend. The diffraction features of a neat film of P3HT-*co*-P3HHT spun-cast from solution (15 mg mL^{-1}

THF:NMP) shown in the top-left panel of **Figure 3.2** exhibits distinct (100), (200), and (300) peaks along the out-of-plane direction attributed to diffractions from edge-on oriented lamellar stacks, and a (010) peak along the in-plane direction attributed to diffraction from the π - π stacks, typically observed in semicrystalline P3HT.

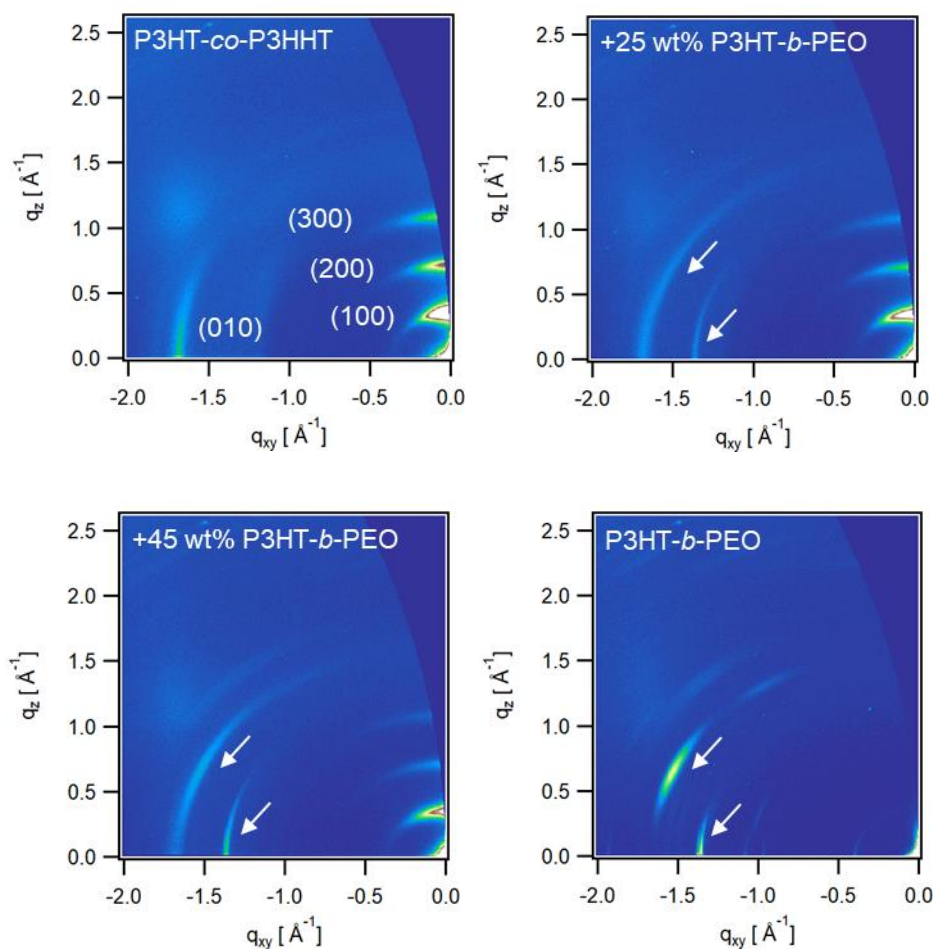


Figure 3.2. GIWAXS patterns of P3HT-co-P3HHT, P3HT-b-PEO, and their blends, as labelled. Distinct diffraction features corresponding to the ordered crystallites of each component can be observed in the blends, implying that blending does not disrupt the long-range ordering of each component.

Indeed, previous work has shown that copolymerization of P3HT with hydroxyhexyl-functionalized thiophene comonomers does not drastically change the long-range order of

its films.⁴ Upon blending with P3HT-*b*-PEO, the diffraction peaks of the P3HT lamella and π stacks do not seem to change considerably, while we observe additional features attributed to PEO-rich crystallites matching those in films of the neat block copolymer (bottom-left, **Figure 3.2**), marked by the arrows. This indicates an almost completely phase-separated blend, wherein the long-range order of each phase appears undisrupted and essentially equivalent to that of their neat film counterparts.

3.2.2. Thermal properties

Results from DSC analysis further indicate phase separation in the blends with evidence of some compatibility between the two components. Samples were prepared by drop-casting films from solution onto cleaned glass slides, following the same solution composition and casting temperatures used for OECT fabrication to ensure that the DSC samples are as similar to the OECT films as possible (see methods in appendix section **A.3.2 Differential scanning calorimetry** for more details). The films were then scraped and shred into fine pieces to be loaded into aluminum crucibles. First heating traces were recorded to investigate the thermal properties of the as-cast films, while second heating traces were recorded after slowly cooling the samples from the melt for comparison. **Figure 3.3** gives the thermograms of the first heating, cooling, and second heating traces for samples of neat P3HT-*co*-P3HHT, neat P3HT-*b*-PEO, and their blends at different compositions. The values of various thermal properties extracted from the thermograms are tabulated in **Table 3.1**.

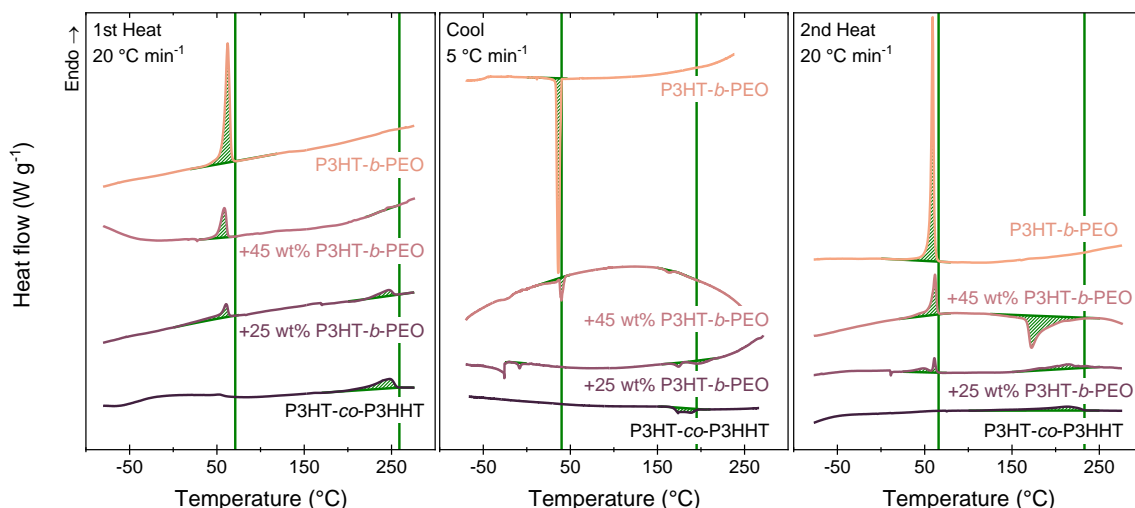


Figure 3.3. Thermograms of solution-cast P3HT-co-P3HHT and its blends with P3HT-b-PEO from the first heat (left-most), cool (middle), and second heat (right-most). The presence of melting peaks corresponding to each component in the first heating scan of the blends suggests a phase separated structure.

Table 3.1. Transition temperatures and enthalpies extracted from thermograms of blends of P3HT-co-P3HHT and P3HT-b-PEO.

P3HT-b-PEO content (wt%)	Mass (mg)	1 st Heat				Cool				2 nd Heat			
		$T_{m1,end}$ (°C)	ΔH_1^a (J g ⁻¹)	$T_{m2,end}$ (°C)	ΔH_2^b (J g ⁻¹)	$T_{c1,on}$ (°C)	ΔH_1^a (J g ⁻¹)	$T_{c2,on}$ (°C)	ΔH_2^b (J g ⁻¹)	$T_{m1,end}$ (°C)	ΔH_1^a (J g ⁻¹)	$T_{m2,end}$ (°C)	ΔH_2^b (J g ⁻¹)
0	1.6	--	--	259	40	--	--	195	-17	--	--	233	26
25	1.4	66	102	255	21	-6	-14	179	-6	66	69	223	7
45	1.1	67	98	257	4	45	-50	168	-4	71	98	158 ^c	-109 ^d
100	1.3	71	154	--	--	40	-141	--	--	66	146	--	--

^aNormalized to weight fraction of PEO block; ^bNormalized to weight fraction of P3HT + P3HHT moieties; ^cOnset temperature and ^denthalpy of cold crystallization exotherm;

As-cast P3HT-co-P3HHT exhibits a broad melting peak that ends at $T_{m2,end} = 259$ °C, which is close to that of solution-cast P3HT homopolymer of similar molecular weight (≈ 250 °C),⁵ while as-cast P3HT-b-PEO shows a single sharp peak and $T_{m1,end} = 71$ °C attributed to PEO melting. The absence of a melting peak corresponding to the P3HT moiety in the block copolymer might be due to its low molecular weight ($M_n, P3HT = 5$ kg mol⁻¹) relative

to the PEO block ($M_{n, PEO} = 20 \text{ kg mol}^{-1}$) and the strong tendency of PEO of this molecular weight to crystallize. After melting at $300 \text{ }^\circ\text{C}$, neat P3HT-co-P3HHT exhibits a melting temperature ($T_{m,end} = 233 \text{ }^\circ\text{C}$) significantly lower than that of the as-cast material measured in the first scan. This is likely due to an increased entanglement density where melt processing leads to a smaller lamellae thickness, which is directly related to the melting temperature.⁶ Indeed, the molecular weight of P3HT-co-P3HHT ($M_{n,P3HT-co-P3HHT} = 30 \text{ kg mol}^{-1}$) used here is around the critical molecular weight of entanglement for P3HT ($M_{c,P3HT} = 25\text{-}35 \text{ kg mol}^{-1}$).⁵ Similarly, the molecular weight of the PEO moiety is well above the reported molecular weight between entanglements ($M_{e,PEO} \approx 1.6\text{-}2.5 \text{ kg mol}^{-1}$),⁷ thus, its melting during the second heat trace occurs at a temperature less than that from the first heat (*i.e.*, a solution-processed sample). This supports the view that the polymers are thermally stable within the temperature range employed here.

The thermograms of the as-cast blends (1st heat) display distinct melting peaks attributed to the polythiophene and PEO moieties, which indicates phase separation and aligns with results from GIWAXS analysis. However, closer inspection of the thermal transitions of each moiety also provides evidence of compatibility of the blend. Increasing the P3HT-*b*-PEO content in the blend clearly leads to lowering of the melting enthalpy of the P3HT-rich phase (refer to **Table 3.1**; note that the values are estimated by normalizing the integrated endothermic peak area to the combined weight fraction of the P3HT-co-P3HHT component and the P3HT-block, assuming the latter might also contribute to the P3HT-rich phase). Likewise, the melting enthalpy attributed to PEO decreases with increasing P3HT-co-P3HHT content. Thus, the crystallization of both phases is, to an extent, suppressed in the blends, which implies sufficient interaction between the components. This is highlighted in the left panel of **Figure 3.4**, which plots the enthalpies extracted from integrating the areas under the thermogram peaks from the first heat scan of different blend compositions. Points below the “ideal” trend expected for completely phase separated components (dashed lines) indicate some compatibility of the blend.

Accordingly, we also observe depression of the melting point of both moieties upon blending, indicating smaller crystals.⁶

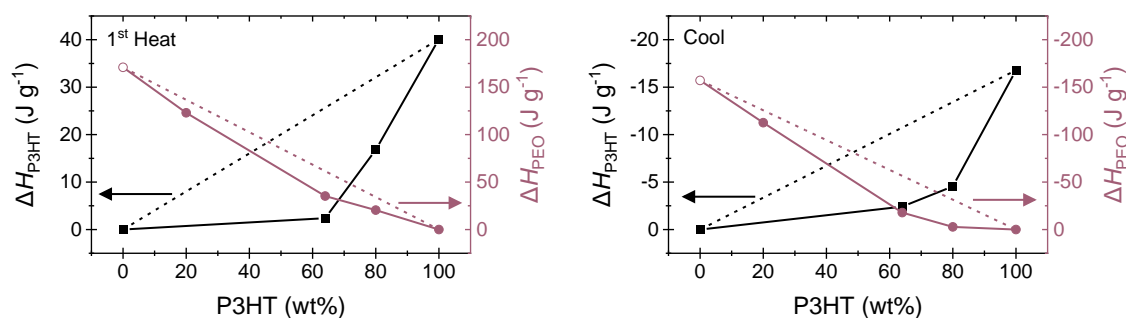


Figure 3.4. Enthalpies of the P3HT (black, left axis) and PEO (pink, right axis) moieties in blends of P3HT-co-P3HHT and P3HT-*b*-PEO cast from solution (left) and cooled from the melt (right), extracted from thermograms. The dashed lines indicate “ideal” values for completely phase-separated components. Data at 0 wt% P3HT extracted from measurements of a PEO homopolymer (open symbol) with the same molecular weight as the PEO moiety in the block copolymer ($M_{n,PEO} = 20 \text{ kg mol}^{-1}$). Enthalpies below the ideal line indicates suppressed crystallization of the component in the blend relative to neat films.

Signs of compatibility can also be observed in the cooling traces of the blends, as implied by the right panel of **Figure 3.4**. The normalized crystallization enthalpies of the P3HT and PEO moieties are notably lowered with increasing co-component content in the blend (see **Table 3.1**). The blend with a composition of 25 wt% P3HT-*b*-PEO, in particular, exhibits a massively suppressed crystallization exotherm of the PEO block ($\Delta H_1(\text{cool}) = -14 \text{ J g}^{-1}$), also indicated by the larger supercooling ($\Delta T = T_{m1, \text{end}}(2^{\text{nd}} \text{ heat}) - T_{c1} = 72 \text{ }^\circ\text{C}$) relative to that of the neat P3HT-*b*-PEO ($\Delta T = 26 \text{ }^\circ\text{C}$). Similarly, the blend comprising 45 wt% P3HT-*b*-PEO shows significantly reduced crystallization enthalpy of the P3HT-rich phase ($\Delta H_2(\text{cool}) = -4 \text{ J g}^{-1}$) and a cold crystallization exotherm in the 2nd heat trace, which gives further indication of notable interaction between the phases. Compatibility between the

polythiophene and PEO segments might be facilitated by the P3HT moiety in the block copolymer, as well as by possible interactions between PEO and the polar -OH substituents of the P3HT-co-P3HHT component. Consequently, no large-scale phase separation is apparent in the microscopy images of the blends presented in **Figure 3.5** even under cross-polarization to observe birefringence like that in films of neat P3HT-*b*-PEO. According to these results, we deduce that the blends are comprised of at least three phases at very fine length scales; the P3HT-rich, PEO-rich, and intermixed P3HT-PEO phases.

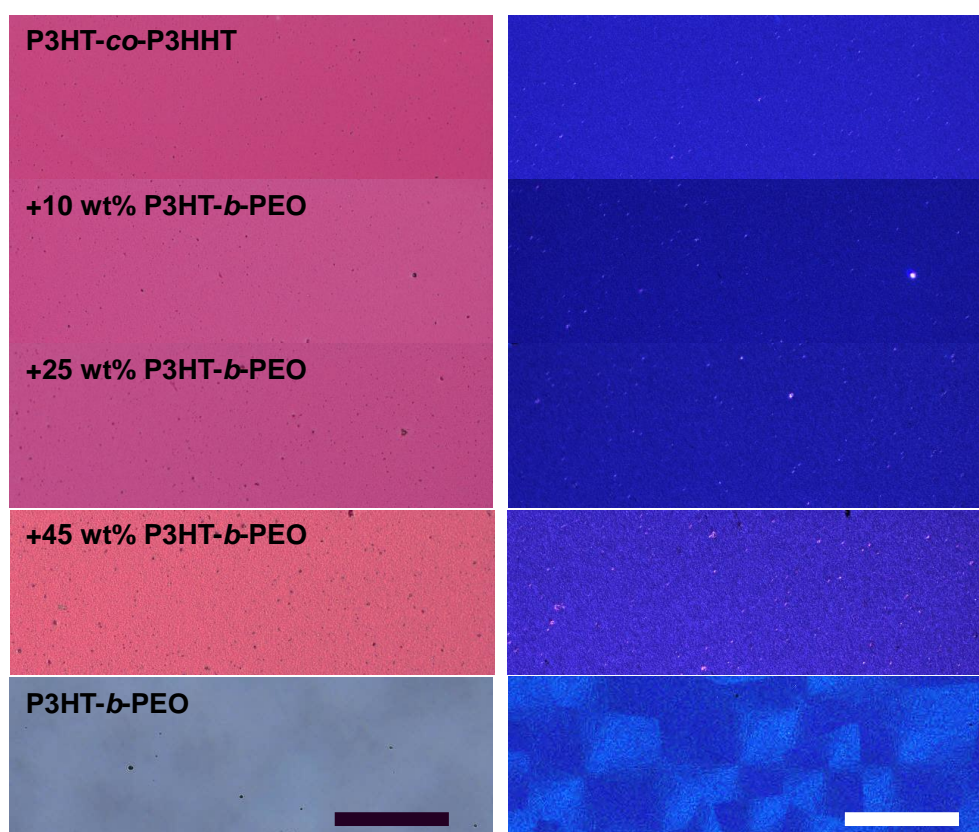


Figure 3.5. Optical microscopy images of P3HT-co-P3HHT and its blends with P3HT-*b*-PEO in transmittance mode (left) and corresponding cross-polarized mode (right), showing no distinct large-scale domains in the blends. Scale bar measures 200 μm .

3.2.3. Surface polarity

Owing to a certain degree of microphase separation, the short- and long-range order of P3HT-co-P3HHT is not drastically changed upon blending, as we've observed from the UV-Vis absorption and GIWAXS, respectively. On the other hand, addition of the block copolymer does have a strong impact on the water contact angles of the films, plotted in **Figure 3.6**. Angles were measured immediately after the water droplet was in contact with the surface and 30 seconds after contact to inspect for the possibility of droplet uptake in the film, of which none was largely apparent. Results show that increasing the block copolymer content decreases the water contact angle of the film surface. As little as 25 wt% block copolymer content can be added to efficiently reduce the contact angle from about 90° down to 70°, with no significant further decrease observed at higher compositions. This demonstrates efficient enhancement of the surface hydrophilicity, which may be pertinent to applications interfacing with water-rich media. We also assume that this reflects bulk material hydrophilicity, which may be more relevant for mixed conductors operating by bulk electrochemical mechanisms, since the blends appear to be compatible and may therefore exhibit relatively uniform macroscopic properties.

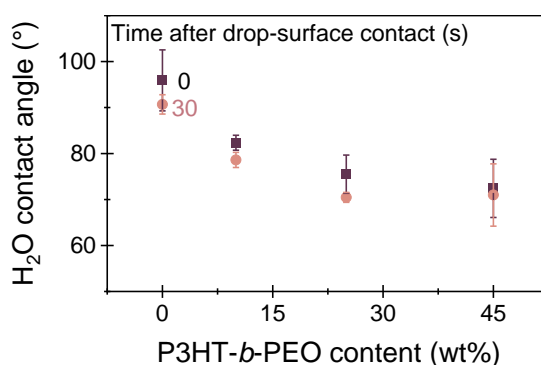


Figure 3.6. Water contact angles of P3HT-co-P3HHT and its blends with P3HT-b-PEO, suggesting increased hydrophilicity with higher block copolymer content.

3.3. Electrochemical properties

We suspect that the increased hydrophilicity of the material upon blending explains the enhanced transient behavior observed in the OECTs, since this could facilitate interdiffusion of ions from aqueous electrolytes through the material and support bulk electrochemical operation. In order to assess this further, we tested the electrochemical behavior of P3HT-*co*-P3HT and its blends with P3HT-*b*-PEO. The polymer electrodes were fabricated by depositing films onto cleaned ITO substrates, following the same blending and deposition protocols as that used to make the OECTs. The details of the instrumentation and methodology of the various experiments are outlined under the electrochemical characterization section of the appendix (**A.4 Electrochemical characterization**).

3.3.1. Cyclic Voltammetry

We start by comparing the cyclic voltammograms of the blends measured in different media. **Figure 3.7** plots the voltammograms of P3HT-*co*-P3HHT and its blends with P3HT-*b*-PEO of various compositions (0-45 wt%) measured in organic (left) and aqueous electrolyte (right). Slow scan rates were used after observing that it was more difficult to identify peak anodic currents with faster cycling (see appendix section **A.4.1 Cyclic voltammetry**, **Figure A.5**). Quick inspection of the graphs gives the impression that blending does not drastically change the oxidation behavior of the material for a given electrolyte, electrode area, and scan rate. This implies that similar potentials can be applied to probe the electrochemical response of the different blends and obtain comparable behavior.

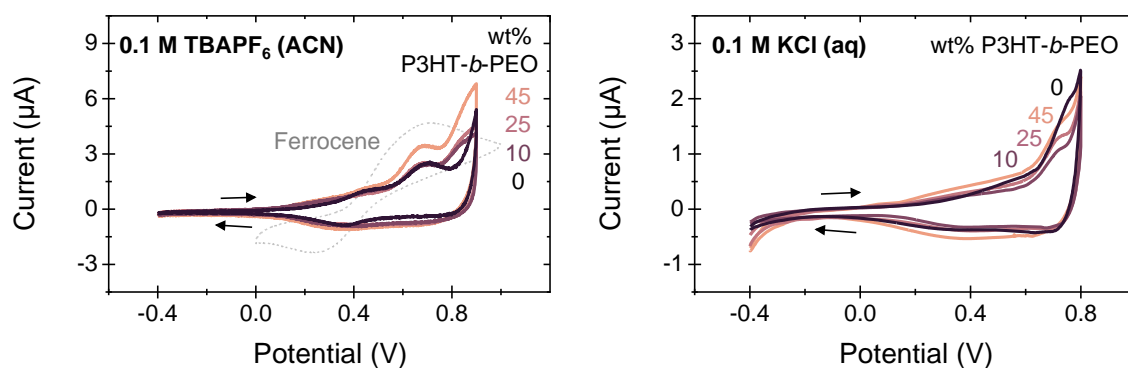


Figure 3.7. Cyclic voltammograms of P3HT-co-P3HHT and its blends with P3HT-b-PEO of different compositions as indicated (wt%) measured at 2 mV s^{-1} against Ag/AgCl in organic (left) and aqueous (right) electrolyte. Ferrocene in organic electrolyte is also shown for reference ($E_{1/2} = 0.48 \text{ V}$).

However, upon closer examination of the anodic (charging) currents plotted in **Figure 3.8**, we notice subtle differences between the neat material and its blends when measured in organic or aqueous electrolyte, which could hint towards enhanced ion uptake efficiency in the blends. For instance, the oxidation onset potentials identified for the blends are generally less than that of the neat material, by about 100 to 200 mV depending on the composition and electrolyte, as outlined in **Table 3.2**. Also, operating the neat P3HT-co-P3HHT in aqueous electrolyte appears to result in higher onsets ($E_{ox,on}(aq) = 0.22 \text{ V}$) and peak anodic potentials ($E_{pa}(aq) = 0.75 \text{ V}$) relative to those measured with organic electrolyte ($E_{ox,on}(ACN) = 0.14 \text{ V}$, $E_{pa}(aq) = 0.70 \text{ V}$). In contrast, the onsets and peak potentials extracted for the blends measured in the different media are practically in agreement (<50 mV difference). This might suggest that blending effectively lowers the energy barriers associated with electrochemical oxidation of the semiconducting P3HT-co-P3HHT in aqueous electrolyte, potentially due to the PEO moiety facilitating hydrated ion uptake and transport throughout the material.

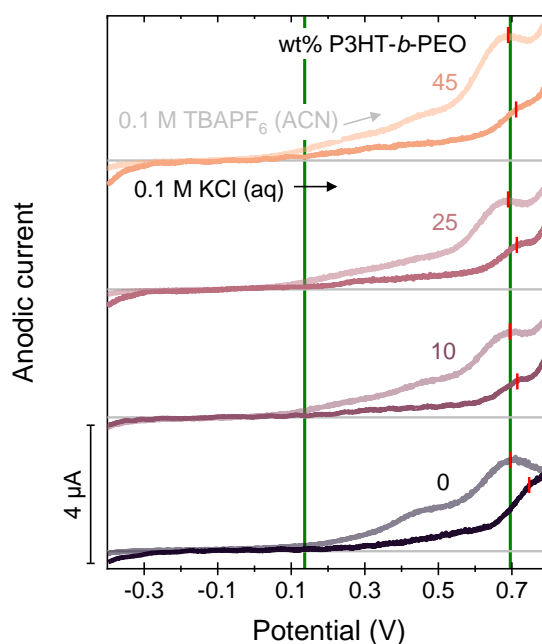


Figure 3.8. Anodic currents extracted from cyclic voltammetry sweeps of P3HT-co-P3HHT and its blends with P3HT-*b*-PEO measured in organic (transparent lines) and aqueous (opaque lines) electrolyte. Solid green lines indicate oxidation onset and peak anodic potential of neat P3HT-co-P3HHT measured in 0.1 M TBAPF₆ for reference. Peak anodic currents indicated by red ticks.

Table 3.2. Oxidation onsets ($E_{ox,on}$) and anodic peak potentials (E_{pa}) extracted from voltammograms measured against Ag/AgCl as reference at 2 mV s^{-1} .

Polymer	0.1 M TBAPF ₆ (ACN)		0.1 M KCl (aq)	
	$E_{ox,on}$ (V)	E_{pa} (V)	$E_{ox,on}$ (V)	E_{pa} (V)
P3HT-co-P3HHT	0.14	0.70	0.22	0.75
+ 10 wt% P3HT- <i>b</i> -PEO	0.06	0.69	0.05	0.71
+ 25 wt% P3HT- <i>b</i> -PEO	0.04	0.69	0.00	0.71
+ 45 wt% P3HT- <i>b</i> -PEO	0.03	0.69	0.00	0.71
Ferrocene	0.48 [†]		--	

[†]Half-wave potential ($E_{1/2}$)

These findings lead us to wonder whether blending modification with an ion-conducting component can enhance the oxidation behavior of hydrophobic conjugated

polymers when operating in aqueous media, without engineering substituents on the active semiconducting component. To test this, we characterized blends of P3HT-*b*-PEO with a non-hydroxyhexyl substituted P3HT of molecular weight similar to that of the P3HT-*co*-P3HHT ($M_n = 30 \text{ kg mol}^{-1}$). **Figure 3.9** plots the voltammograms measured for P3HT-*co*-P3HHT, P3HT, and blends of P3HT with 25 wt% P3HT-*b*-PEO in organic (left) and aqueous (right) electrolyte. The values of the oxidation onsets and peak anodic currents are tabulated in **Table 3.3**.

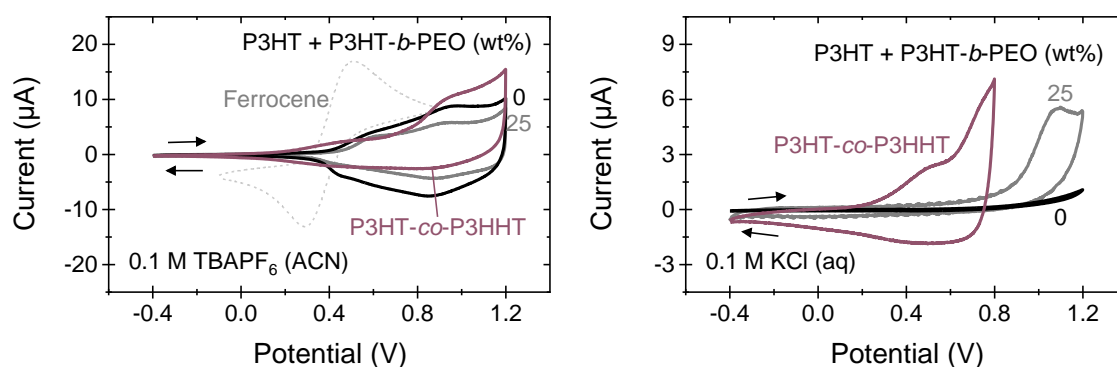


Figure 3.9. Cyclic voltammograms of P3HT, its blend with 25 wt% P3HT-*b*-PEO, and P3HT-*co*-P3HHT measured against Ag/AgCl as reference at 10 mV s^{-1} in organic (left) and aqueous (right) electrolyte. Ferrocene in organic electrolyte is also shown for reference ($E_{1/2} = 0.4 \text{ V}$).

Table 3.3. Oxidation onsets extracted from voltammograms of polymers measured against Ag/AgCl as reference at 10 mV s^{-1} .

	0.1 M TBAPF ₆ (ACN)	0.1 M KCl (aq)
Polymer	$E_{ox,on}$ (V)	$E_{ox,on}$ (V)
P3HT- <i>co</i> -P3HHT	0.18	0.26
P3HT	0.40	--
P3HT + 25 wt% P3HT- <i>b</i> -PEO	0.46	0.88
Ferrocene	0.40 [†]	--

[†]Half-wave potential ($E_{1/2}$)

We determine from the voltammograms measured in organic media that hydroxyhexyl substitution of P3HT lowers its oxidation onset by about 200 mV, which we attribute to the improvement of ion uptake efficiency facilitated by the polar sidechains. Conversely, blending P3HT with P3HT-*b*-PEO increases the oxidation onset slightly by about 60 mV. When operating in aqueous electrolyte, no significant oxidation behavior is observed for P3HT within the potential window investigated here, likely the result of the hydrophobic material being impenetrable to the hydrated ions. Blending this with the block copolymer does seem to enhance its electrochemical activity in aqueous media, indicated by a steep increase of the anodic current. However, the potential range at which this occurs is too high for practical applications and risks side reactions with water. This highlights the importance of engineering substituents on the active semiconductor in combination with blending modification when developing new polymeric mixed conducting materials.

3.3.2. Spectroelectrochemistry

We obtain more evidence supporting that blending P3HT-*co*-P3HHT with P3HT-*b*-PEO enhances the efficiency of ion uptake in the material leading to faster electrochemical device operation by probing the electrochemical doping kinetics of the films *via* spectroelectrochemistry. The experimental design is illustrated in **Figure 3.10** and involves measuring the evolution of the absorbance spectra of the film over time during application of a potential step in the presence of an electrolyte. Oxidation (doping) of the p-type semiconducting polymer changes the structure of the backbone from benzenoid- to quinoid-like as positively charged polarons and bipolarons are created. This is accompanied by the formation of corresponding electronic states within the energy gap of the initially neutral material, thereby allowing lower energy transitions. Practically, this can be observed as bleaching of the film involving a decrease of absorbance corresponding to the initial $\pi\text{-}\pi^*$ transition and an increase of absorbance at higher wavelengths.⁸ Thus, this phenomenon

provides a simple way to directly probe the electrochemical doping behavior of the polymer semiconductor *via* its optical properties.

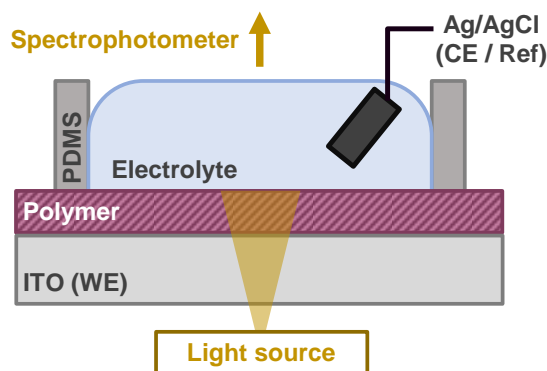


Figure 3.10. Schematic diagram of experimental setup used for spectroelectrochemical measurements.

3.3.2.1. Electrochemical bleaching

The evolution of the absorbance spectra in P3HT-*co*-P3HHT and its blends with P3HT-*b*-PEO of different compositions (0-45 wt%) during electrochemical oxidation in aqueous electrolyte (0.1 M KCl; the same as that employed in the OECTs) is presented in **Figure 3.11**. The left panel shows that, at a potential of 0 V ($t = 0$ s), the neutral materials exhibit similar maxima at $\lambda = 560$ nm. Application of a potential step from 0 to 0.75 V, chosen as the doping bias based on the anodic peak potentials observed from cyclic voltammetry, leads to a decrease of the absorbance intensity at 560 nm followed by an increase of a broad absorbance centered at around 800 nm. This behavior matches that of P3HT reported in literature, in which the increase of absorbance at around 800 nm with bias up to 0.9 V vs Ag/AgCl in organic electrolyte (0.1 M TBAPF₆ in acetonitrile) corresponds to sub-gap electronic transitions (≈ 1.7 eV) associated with polaronic states.⁸ Mapping the change of the normalized absorbance over time during application of the doping bias given in the

right panel of **Figure 3.11** shows that the blends approach steady state conditions much faster than the neat material.

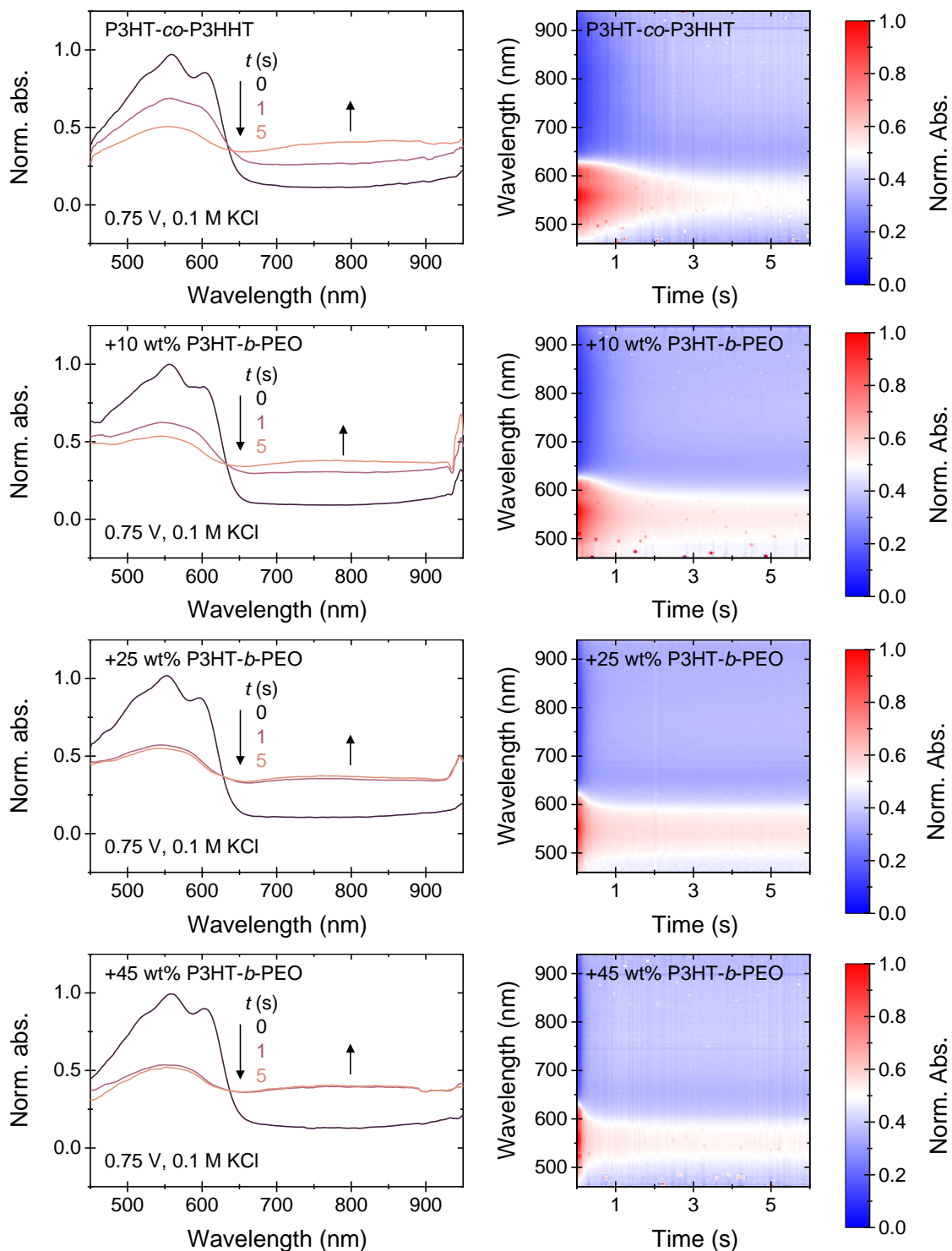


Figure 3.11. Normalized UV-Vis absorbance spectra of P3HT-co-P3HHT and its blends with P3HT-b-PEO measured upon application of a step potential (left). Color map showing evolution of spectra over time (right).

We also observe in **Figure 3.12**, which plots the normalized peak absorbance (560 nm) over time under constant doping bias, that all the materials investigated here display similar relative decrease of the absorbance intensity at steady state (*norm. abs. ($t = ss$)* \approx 0.5 at 0.75 V). This suggests that incorporation of the PEO moiety does not seem to largely affect the steady state spectroelectrochemical response of the polythiophene-rich phases, which we can attribute again to phase separation in the blend. Additionally, recovery of the initial absorption upon application of zero to negative bias indicates that the films can be easily de-doped, which assures that the electrochemical behavior is highly reversible within the potential range investigated here.

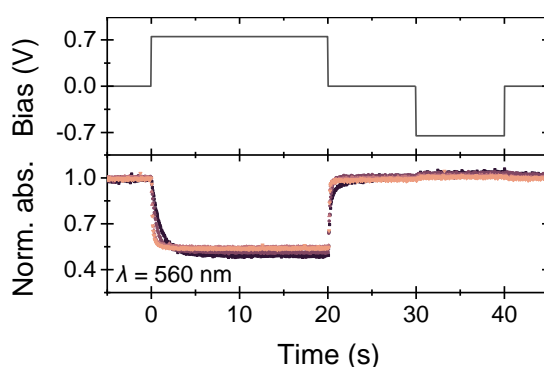


Figure 3.12. Normalized peak absorbance of P3HT-co-P3HHT and its blends with P3HT-b-PEO plotted over time at various indicated biasing conditions. Data are for films of similar thickness ($d = 110 \pm 10$ nm) to facilitate comparisons.

3.3.2.2. Electrochemical doping rates

The influence of blending on the absorbance transients of P3HT-co-P3HHT is emphasized in **Figure 3.13**, which focuses on the normalized peak absorbance rescaled from 0-1 (*norm. rel. abs.*) measured within the first few seconds of applying bias. Blends with higher block copolymer content exhibit significantly faster absorbance transients (top

panel of **Figure 3.13**). This trend correlates with the greater hydrophilicity of the films, which might contribute to decreasing the energy barriers associated with the injection of hydrated ions into the bulk necessary to electrochemically dope the polymer. Faster absorbance change is also measured in thinner films of P3HT-co-P3HHT (bottom-left panel of **Figure 3.13**), which suggests that doping occurs throughout the bulk of the film even in the relatively more hydrophobic material. However, the blends generally show faster absorbance transients in thicker films (210 nm), approaching steady state within a second of applying bias (bottom-right panel of **Figure 3.13**), than the thinnest films of the neat material (110 nm), only approaching steady state after 3 seconds. This behavior demonstrates the efficacy of blending to tune the electrochemical doping kinetics of the material.

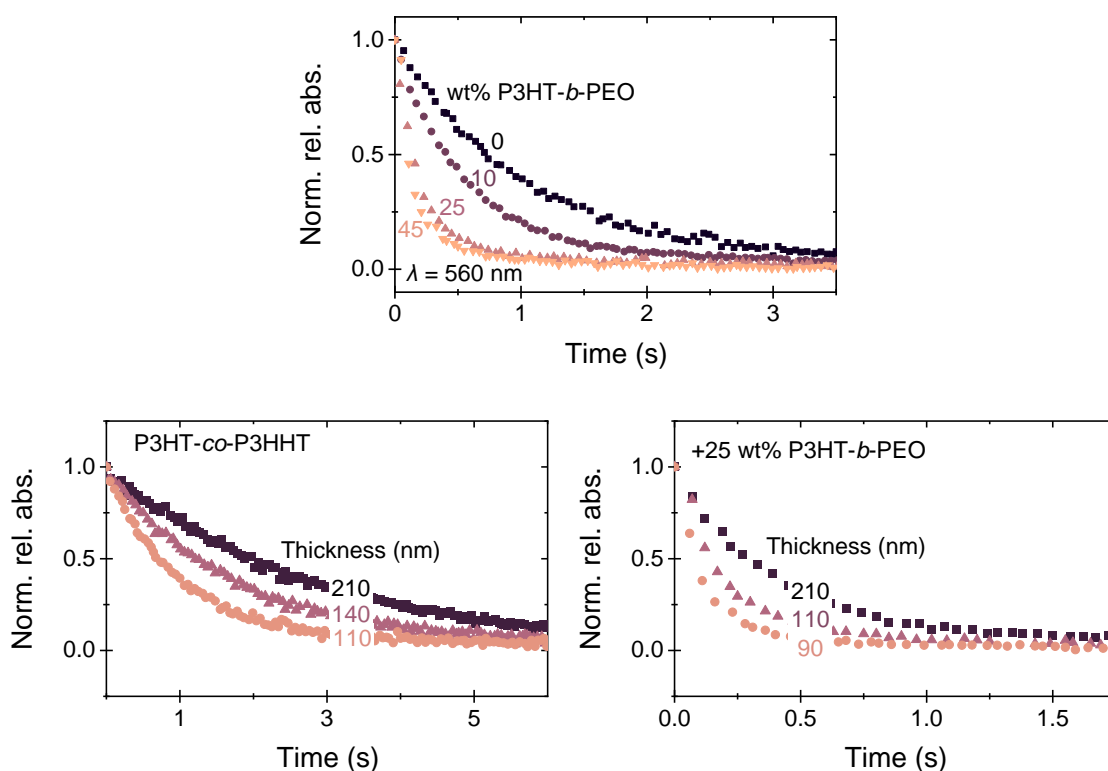


Figure 3.13. Normalized peak absorbance transients rescaled 0-1 (norm. rel. abs) of P3HT-co-P3HHT and its blends with P3HT-b-PEO (film thickness $d = 110 \pm 10 \text{ nm}$) upon application of bias (top). Normalized peak absorbance transients of P3HT-co-P3HHT

(bottom-left) and its blend with 25 wt% P3HT-*b*-PEO (bottom-right) for different film thicknesses.

3.3.2.3. Monophasic exponential kinetic model

Assuming that the change in absorbance is directly proportional to the decrease of neutral polythiophene segments to form polaronic species and follows first order kinetics, we estimate the electrochemical doping rates from the rate constants (k) extracted from exponential decay fits to the transients. **Figure 3.14** shows that a single-phase exponential decay function fits adequately with the experimental data until about 90% of the total change, beyond which the data deviates from the model as it approaches steady state.

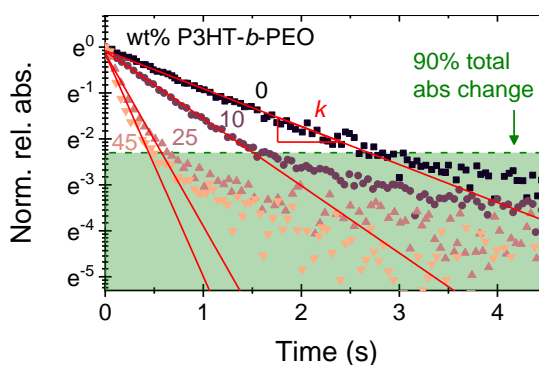


Figure 3.14. First-order kinetic model fits (solid red line) to the initial 90% of normalized absorbance transients of P3HT-co-P3HHT and its blends with P3HT-*b*-PEO to extract electrochemical doping rates (k).

The rate constants (k) extracted for each blend composition at different film thicknesses (d) are summarized in **Figure 3.15**. Blends with more block copolymer content show generally higher rates while also stronger dependence of k on film thickness. Again, this highlights the power of blending as a tool to manipulate the transient electrochemical

behavior of polymeric mixed conductors. Furthermore, upon normalizing the rate constants to film thickness (kd^{-1}) from the slopes of k versus d , we find that as little as 25 wt% P3HT-*b*-PEO suffices to efficiently enhance the doping kinetics, while increasing the composition further to 45 wt% P3HT-*b*-PEO offers no significant additional improvement. This appears to align well with the trend observed in the water contact angles of the blends.

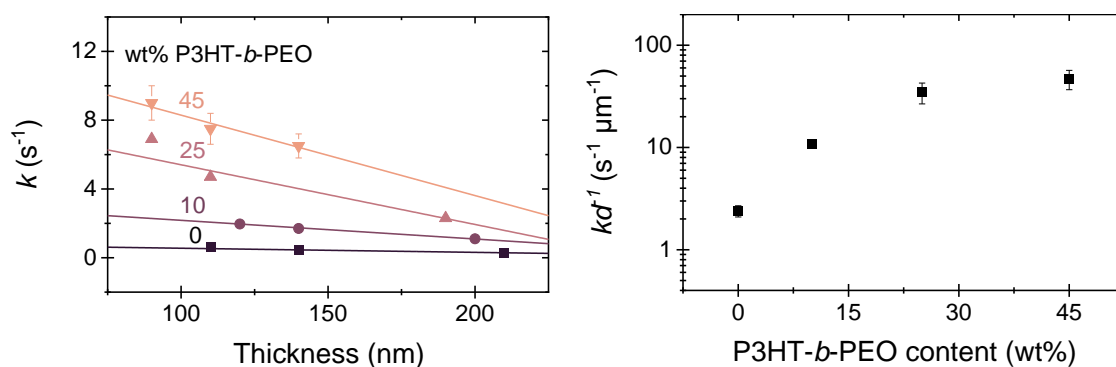


Figure 3.15. Summary of electrochemical doping rates (k) extracted for P3HT-co-P3HHT and its blends with P3HT-*b*-PEO at various film thicknesses (left). Thickness-normalized rates (kd^{-1}) plotted against blend composition (right).

3.3.2.4. Biphasic exponential kinetic model

The single-phase exponential model can sufficiently describe most of the signal change during the early regime of the absorbance decay, however it does not consider simultaneous processes occurring at different rates. Multiphase exponential functions can better account for these. A biphasic exponential decay function of the form shown in **Figure 3.16** fits satisfactorily with the experimental data up to steady state conditions and describes well enough the slower regime of the transient. Consequently, two rate constants can be extracted corresponding to faster (k_1) and slower (k_2) kinetic processes that proceed at the same time during electrochemical doping.

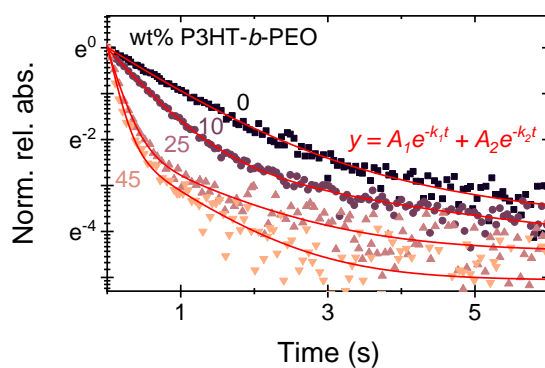


Figure 3.16. Biphasic exponential model fits (red solid line) to normalized absorbance transients of P3HT-co-P3HHT and its blends with P3HT-b-PEO.

Plots of k_1 and k_2 obtained for each blend composition in **Figure 3.17** shows the same trend as that observed in the rate constants extracted from monophasic exponential fits. Meanwhile, although logarithmic plots show that both rate constants increase with higher block copolymer content, the increase in k_1 is much more significant than k_2 .

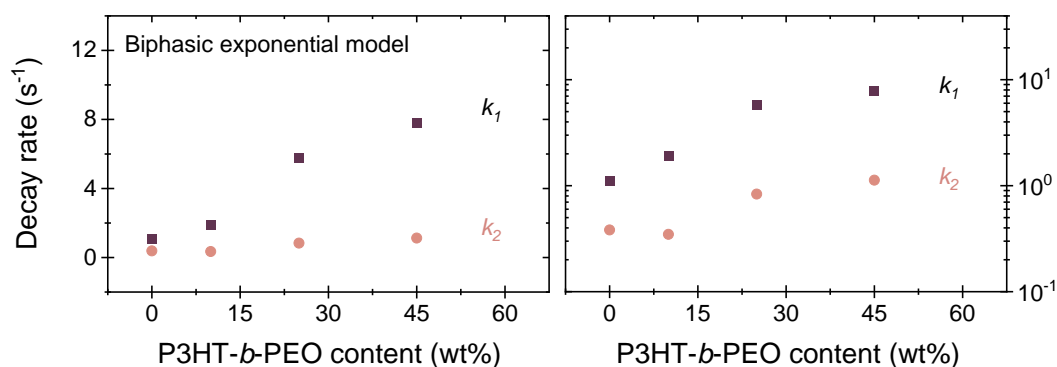


Figure 3.17. Summary of decay rates extracted for P3HT-co-P3HHT and its blends with P3HT-b-PEO of similar film thickness (110 ± 10 nm) using biphasic exponential functions, plotted linearly (left) and logarithmically (right).

Concurrent doping mechanisms with different kinetics in polymeric mixed conductors may be the result of a distribution of charge injection energy barriers in the material due to its complex solid-state structure. For instance, we could speculate that the faster processes indicated by k_1 can be attributed to more facile ion injection in the amorphous phases of the material while the slower processes represented by k_2 might reflect ion injection into the densely packed ordered aggregates. This is inspired from literature investigating the structure of P3HT in electrochemical devices gated with an ionic liquid,⁹ which suggests that at low voltages and high frequencies, ions only enter the amorphous fraction of the polymer, while at high voltages and low frequencies, ions may penetrate the crystallites. We could then further surmise that the stronger influence of blending on k_1 reflects that the hydrophilic, ionically conducting PEO segments are well integrated with the active semiconducting P3HT-co-P3HHT segments in the amorphous phases. Meanwhile, ion uptake in the ordered P3HT-co-P3HHT domains indicated by k_2 is less affected by blending, perhaps due to the large extent of micro-scale phase separation leading to greater purity in the ordered phases, as we deduced from investigating the physical properties of the blend.

3.3.3. Impedance behavior

Examination of the results from spectroelectrochemistry reveals that the incorporation of P3HT-*b*-PEO in blends with P3HT-co-P3HHT strongly influences its electrochemical transient behavior, while the steady state response appears to be unaffected. We further investigate the doped state of the materials using electrochemical impedance spectroscopy (EIS), which also provides insight into the bulk capacitance of the films.

In the absence of inductive effects, the complex impedance (Z) of a simple AC circuit defined in **Equation 3.1** arises from the combination of an ohmic resistance (R) equivalent to the real part of the impedance (Z_{re}) and a capacitive reactance ($X_c = -(\omega C)^{-1}$), constituting the imaginary part of the impedance (jZ_{im}).^{10,11}

$$Z = Z_{re} + jZ_{im} \quad \mathbf{3.1}$$

Where

$$Z_{re} = R$$

$$Z_{im} = X_c = -(\omega C)^{-1}$$

Conventionally, the reactance of a capacitive element (X_c) is negative to reflect the phase lag of the AC voltage with respect to the AC current in a charging capacitor.¹² It follows that the phase angle (θ) between Z_{re} and Z vectors is also negative, but for the purpose of clarity we temporarily omit the sign. For an ideal capacitor, $\theta = 90^\circ$. However, typically $\theta < 90^\circ$ in real capacitors due to parasitic resistances. In the case where effects from diffusion processes (e.g., diffusion of reactive species,¹³ adsorption of ions on porous electrodes¹⁴) dominate, the phase shift may approach 45° and the impedance response can be modelled by a Warburg element.¹⁵ Dominance of resistive effects is indicated by the imaginary part of the complex impedance (θ and Z_{im}) approaching zero.¹¹

The impedance response of P3HT-*co*-P3HHT and its blends with P3HT-*b*-PEO was measured over a frequency range of 10^{-1} to 10^4 Hz while applying a DC offset bias at 0.75 V to probe the doped state of the materials. We note that the doping bias was applied prior to beginning the impedance measurement over a sufficient time period to reach equilibrium (about 30-60 seconds depending on the blend composition and film thickness, based on observations during spectroelectrochemical measurements). The frequency-dependence of

the impedance magnitude ($|Z|$ vs f), imaginary part of the impedance ($-Z_{im}$ vs f), and phase angle (θ vs f), as well as the Nyquist plots (Z_{im} vs Z_{re}) measured for the different blends are shown in **Figure 3.18**.

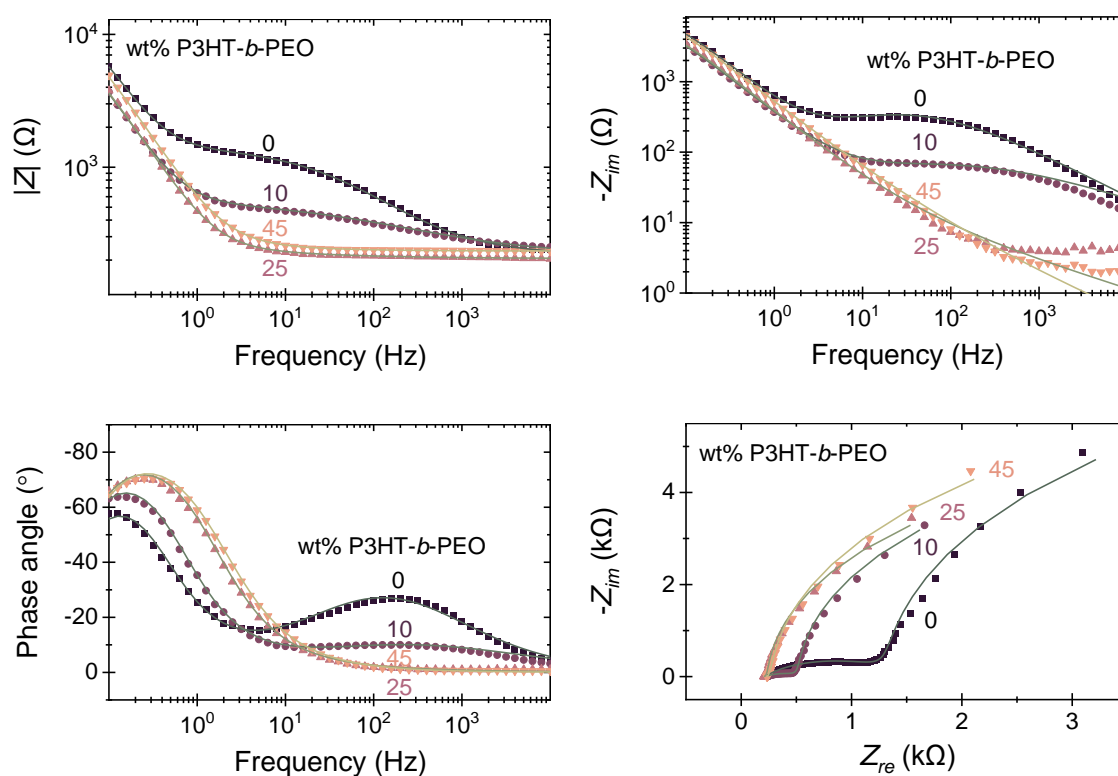


Figure 3.18. Impedance magnitude ($|Z|$, top-left), imaginary impedance ($-Z_{im}$, top-right) and phase angle (bottom-left) plotted against frequency, and Nyquist plots (Z_{re} vs $-Z_{im}$, bottom-right) of P3HT-co-P3HHT and its blends with P3HT-b-PEO. Scatter plots refer to experimental data while solid lines correspond to equivalent circuit model fits.

At high frequencies, $f > 10^3$ Hz, all materials exhibit minimum $|Z|$ with Z_{im} and phase angles approaching zero, implying mostly resistive behavior, which we attribute to the resistance of the electrolyte solution. Operating at low frequencies, $f < 1$ Hz, $|Z|$ and Z_{im} rise in all materials to approximately the same magnitude of about 5 k Ω at 0.1 Hz, while the phase angle approaches its global maximum peak of around -60° to -70° , indicative of

capacitive effects dominating the impedance response at longer time periods. We note that the blends with higher block copolymer content display onsets of the phase angle peaks at slightly higher frequencies, which could suggest that their capacitive behavior manifests at shorter time periods relative to the neat P3HT-co-P3HHT. This might correlate with the trends observed in the OECT transient current data and absorption transients measured during electrochemical doping.

Major differences in the impedance response of the neat material and the blends arise at the mid-frequency range between 1 and 10^3 Hz. Neat P3HT-co-P3HHT exhibits a plateau of $|Z|$ and Z_{im} at about 1 and 3 k Ω , respectively, and a local maximum phase angle of -30° , which we attribute to diffusion effects dominating the impedance response. We speculate that the diffusion-limited mid-frequency impedance response results from hampered penetration of hydrated ions into the relatively hydrophobic film. This could also explain the depressed semi-circle feature apparent in the Nyquist plots of the neat material (**Figure 3.18**, bottom-right). Blending appears to suppress this behavior, indicated by the drop of the impedance plateaus to lower magnitudes and the phase angle approaching zero at higher block copolymer compositions. This trend might correlate with enhanced ion transfer efficiency across the polymer-electrolyte interface in the more hydrophilic material.

3.3.3.1. Equivalent circuit model-fitting

To facilitate interpretation of the impedance response and extraction of physical parameters such as the capacitance of the polymer films, we fit the experimental data with an equivalent circuit model. The spectra could be fit reasonably well with a second order Voigt-type equivalent circuit typically used in simplified models of Li-ion battery and supercapacitor cells.^{16,17} The model is shown in **Figure 3.19** and consists of a capacitor (C) describing the capacitance of the film in parallel with a resistor (R_p), in series with a constant

phase element (CPE_i) in parallel with a resistor (R_i), and in series with a solution resistance (R_s). A CPE was included in place of an ideal capacitor element to better describe the mid-frequency impedance behavior and depressed semi-circle feature in the Nyquist plots of neat P3HT-co-P3HHT.

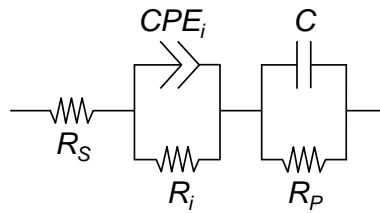


Figure 3.19. Equivalent circuit model fitted to experimental impedance data in Figure 3.17 (solid green lines) consisting of a resistor (R_s) in series with a constant phase element (CPE_i) and resistor (R_i) in parallel, also in series with a capacitor (C) and resistor (R_p) in parallel.

The total impedance of the equivalent circuit described above is given in **Equation 3.2**.

$$Z_{tot} = Z_s + Z_{CPE_i||R_i} + Z_{C||R_p} \quad 3.2$$

Where

$$Z_s = R_s$$

$$Z_{CPE_i||R_i} = \frac{1}{Q(j\omega)^n} + R_i$$

$$Z_{C||R_p} = \frac{1}{Cj\omega} + R_p$$

Note that for the CPE, when $n = 1$, it is equivalent to a capacitor element ($Q = C$), and when $n = 0.5$, it is equivalent to a Warburg element that models diffusion processes.¹⁸ Results from extracting the various circuit parameters given in **Table 3.4** show that the values of n for the neat P3HT-co-P3HHT range from about 0.55 to 0.65, which could indicate a diffusion-dominated response. Furthermore, we observe that increasing the P3HT-b-PEO content yields lower R_i and significantly higher Q parameter, implying reduced impedance contribution by the CPE. This describes well the decrease of the mid-frequency impedances and local phase angle maxima, as well as suppression of the semi-circle feature in the Nyquist plots upon blending. Consequently, the equivalent circuit approaches that of a simple Randle's cell ($R_s(C||R_p)$), frequently used in literature to model polymer mixed conductors and deduce the volumetric capacitance (C^*), which describes the strength of ionic-electronic coupling in the material and can be related to the charge carrier density.¹⁹⁻

22

Table 3.4. Parameters extracted from equivalent circuit model fits to experimental impedance data of P3HT-co-P3HHT and its blends with P3HT-b-PEO of various film thicknesses.

P3HT-b-PEO content (wt%)	Thickness (nm)	R_s (Ω)	Q ($\mu\text{S s}^n$)	n	R_i (Ω)	R_p (k Ω)	C (μF)	C^* (F cm^{-3})
0	110 \pm 10	217	28.8	0.643	1170	14	293	190 \pm 30
	150 \pm 10	181	51	0.569	803	7	542	
	210 \pm 10	179	19	0.657	1270	4	720	
10	110 \pm 10	232	138	0.512	302	9.9	450	212 \pm 6
	140 \pm 10	206	129	0.509	318	7.5	550	
	200 \pm 10	213	122	0.505	339	5.5	750	
25	90 \pm 10	198	5500	0.35	90	10.9	346	200 \pm 20
	110 \pm 10	205	6000	0.40	90	9.8	422	
	190 \pm 10	203	5100	0.50	40	4.3	630	
45	90 \pm 10	224	6300	0.38	70	15.5	256	170 \pm 20
	110 \pm 10	232	6700	0.42	140	11.8	324	
	140 \pm 10	231	5000	0.52	130	8.9	490	

3.3.3.2. Volumetric capacitance, C^*

Using the extracted values of C for films with different thicknesses, we could calculate the average C^* of our materials. The results summarized in **Figure 3.20** show relatively small variation in the values between the neat P3HT-co-P3HHT and its blends with P3HT-*b*-PEO under similar doping conditions (DC offset at 0.75 V).

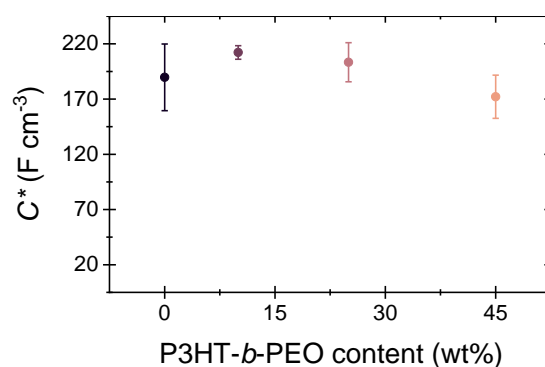


Figure 3.20. Summary of volumetric capacitances calculated for P3HT-co-P3HHT and its blends with P3HT-*b*-PEO, showing relatively similar values.

Assuming that C^* originates from the combination of double-layer capacitances formed between injected ions and charge carriers in the bulk of mixed conductors and is therefore dependent on the bulk charge carrier concentration,²¹ it appears that blending does not change the polaron density of the electrochemically doped material. One explanation for this might be that a significant fraction of the neat material itself does not participate in polaron formation. Hence, the bulk electronic properties of the material may remain insensitive to the incorporation of an insulating moiety, so long as it maintains the structural order of the active semiconducting component necessary for charge carrier formation and transport. Indeed, it has been shown in literature that as little as 3 wt% P3HT in blends with different commodity plastics like polystyrene and polyethylene can yield FET

mobilities approaching that of the neat P3HT with appropriate control of the blend crystallization.²³ This might also explain why the OECTs of the blends exhibit performance, indicated by maximum I_d , g_m , and μC^* , similar to that of devices of the neat P3HT-co-P3HHT, as discussed in the previous chapter.

3.4. Summary

Initial characterizations of the solution-processed blends of P3HT-co-P3HHT and P3HT-*b*-PEO indicate some intermixing or compatibility in the blend despite evidence of phase-separation. Also, the short- and long-range molecular order of P3HT-co-P3HHT in the resulting film is not largely affected upon blending, while no large-scale phase separation is observed *via* optical microscopy. On the other hand, blending notably decreases the contact angles of water on the films, which could indicate increased hydrophilicity of the surface and, therefore, better compatibility of the polymer interface with water-rich media. As a result, the blends seem to exhibit enhanced ion uptake efficiency when operated in aqueous electrolyte, leading to drastically faster electrochemical doping processes observed *via* spectroelectrochemistry. The thickness-normalized spectroelectrochemical rate constant (kd^1) of the neat P3HT-co-P3HHT ($\approx 2.4 \pm 0.3 \text{ s}^{-1} \mu\text{m}^{-1}$), estimated from exponential fits to the absorption transients of the films of different thicknesses and assumed to be proportional to the electrochemical doping rate, could be enhanced at least a full order of magnitude by blending with only 25 wt% P3HT-*b*-PEO ($\approx 35 \pm 8 \text{ s}^{-1} \mu\text{m}^{-1}$), while less dramatic increase is observed with higher block copolymer content ($\approx 48 \pm 10 \text{ s}^{-1} \mu\text{m}^{-1}$). Conversely, the volumetric capacitance of doped P3HT-co-P3HHT ($190 \pm 30 \text{ F cm}^{-3}$), extracted from equivalent circuit model fits to the impedance spectra of the doped films, does not seem to change upon blending. This might indicate that the density of charge carriers, which we assume interacts with injected ions to contribute to double-layer capacitances in the bulk, is relatively similar across the different

blend compositions. This further implies that a large fraction of the neat P3HT-co-P3HHT itself does not participate in polaron formation and transport. We suspect then that the electrical properties of the bulk material may be relatively insensitive to blending with an electronically insulating component, as long as it maintains the necessary structural order of the active semiconducting component in the resulting films. We believe this is achieved in the compatibilized blends and, therefore, explains the sustained C^* and the similar electrical performance of their OECTs relative to that of the neat material.

3.5. References

1. Spano, F. C. & Silva, C. H- and J-Aggregate Behavior in Polymeric Semiconductors. *Annu. Rev. Phys. Chem.* **65**, 477–500 (2014).
2. Dyson, M. J. *et al.* Managing Local Order in Conjugated Polymer Blends via Polarity Contrast. *Chem. Mater.* **31**, 6540–6547 (2019).
3. Clark, J., Chang, J. F., Spano, F. C., Friend, R. H. & Silva, C. Determining exciton bandwidth and film microstructure in polythiophene films using linear absorption spectroscopy. *Appl. Phys. Lett.* **94**, 163306 (2009).
4. Pacheco-Moreno, C. M. *et al.* The Importance of Materials Design to Make Ions Flow: Toward Novel Materials Platforms for Bioelectronics Applications. *Adv. Mater.* **29**, 1604446 (2017).
5. Koch, F. P. V. *et al.* The impact of molecular weight on microstructure and charge transport in semicrystalline polymer semiconductors-poly(3-hexylthiophene), a model study. *Prog. Polym. Sci.* **38**, 1978–1989 (2013).
6. Wunderlich, B. & Czornyj, G. A Study of Equilibrium Melting of Polyethylene. *Macromolecules* **10**, 906–913 (2002).
7. Fetters, L. J., Lohse, D. J., Richter, D., Witten, T. A. & Zirkel, A. Connection between Polymer Molecular Weight, Density, Chain Dimensions, and Melt Viscoelastic Properties. *Macromolecules* **27**, 4639–4647 (1994).
8. Nengl, C. *et al.* Doping-Induced Absorption Bands in P3HT: Polarons and Bipolarons. *ChemPhysChem* **17**, 3836–3844 (2016).
9. Guardado, J. O. & Salleo, A. Structural Effects of Gating Poly(3-hexylthiophene) through an Ionic Liquid. *Adv. Funct. Mater.* **27**, 1–12 (2017).

10. Nave, C. HyperPhysics Concepts. *Georgia State University* (2012). Available at: <http://hyperphysics.phy-astr.gsu.edu/hbase/hph.html>. (Accessed: 23rd October 2021)
11. Arfken, G. B., Griffing, D. F., Kelly, D. C. & Priest, J. ALTERNATING CURRENTS. in *International Edition University Physics* 702–729 (Elsevier, 1984).
12. Bird, J. O. & Chivers, P. J. Single phase series a.c. circuits. in *Newnes Engineering and Physical Science Pocket Book* 103–110 (Newnes, 1993).
13. Vedalakshmi, R., Saraswathy, V., Song, H. W. & Palaniswamy, N. Determination of diffusion coefficient of chloride in concrete using Warburg diffusion coefficient. *Corros. Sci.* **51**, 1299–1307 (2009).
14. Cooper, S. J., Bertei, A., Finegan, D. P. & Brandon, N. P. Simulated impedance of diffusion in porous media. *Electrochim. Acta* **251**, 681–689 (2017).
15. Criado, C., Galán-Montenegro, P., Velásquez, P. & Ramos-Barrado, J. R. Diffusion with general boundary conditions in electrochemical systems. *J. Electroanal. Chem.* **488**, 59–63 (2000).
16. Meddings, N. *et al.* Application of electrochemical impedance spectroscopy to commercial Li-ion cells: A review. *J. Power Sources* **480**, (2020).
17. Zou, C. *et al.* A review of fractional-order techniques applied to lithium-ion batteries, lead-acid batteries, and supercapacitors. *J. Power Sources* **390**, 286–296 (2018).
18. Von Hauff, E. Impedance Spectroscopy for Emerging Photovoltaics. *J. Phys. Chem. C* **123**, 11329–11346 (2019).
19. Rivnay, J. *et al.* High-performance transistors for bioelectronics through tuning of channel thickness. *Sci. Adv.* **1**, e1400251–e1400251 (2015).
20. Inal, S., Malliaras, G. G. & Rivnay, J. Benchmarking organic mixed conductors for transistors. *Nat. Commun.* **8**, 1767 (2017).
21. Proctor, C. M., Rivnay, J. & Malliaras, G. G. Understanding volumetric capacitance in conducting polymers. *J. Polym. Sci. Part B Polym. Phys.* **54**, 1433–1436 (2016).
22. Paulsen, B. D., Tybrandt, K., Stavrinidou, E. & Rivnay, J. Organic mixed ionic–electronic conductors. *Nature Materials* **19**, 13–26 (2020).
23. Goffri, S. *et al.* Multicomponent semiconducting polymer systems with low crystallization- induced percolation threshold. *Nat. Mater.* **5**, 950–956 (2006).

CHAPTER 4:

Stability of mixed conducting polymer blends

4.1. Introduction	145
4.2. Operational stability of blends with P3HT- <i>b</i> -PEO	145
4.2.1. Transfer characteristics	146
4.2.1. Transient performance	147
4.2.2. Stability in water: preliminary QCM investigation	148
4.3. Blends of P3HT- <i>co</i> -P3HHT with PEO.....	152
4.3.1. Physical properties	152
4.3.2. Electrochemical properties	157
4.3.3. OECT performance	164
4.4. Stability of blends with PEO	167
4.4.1. Preliminary QCM analysis	167
4.4.2. OECT transfer characteristics	168
4.4.3. OECT transient characteristics	169
4.5. Summary	171
4.6. References.....	173

4.1. Introduction

We have shown so far that blends of P3HT-*co*-P3HHT and P3HT-*b*-PEO exhibit enhanced electrochemical doping kinetics resulting in faster OECT performance. Meanwhile, the transduction performance of the devices related to the electronic conductivity and charge storage capacity of the films do not seem to change upon blending, which we suspect is facilitated by phase separation in the blend despite some intermixing of the components. We also believe that the P3HT-block chemically linked to the PEO compatibilizes the solution-cast blends, which should help maintain their structural stability and, subsequently, their long-term device performance. To test this, we examine the performance of their OECTs during prolonged immersion in water and probe the stability of the blends in aqueous media through quartz crystal microbalance measurements (QCM). Additionally, we investigate whether we can improve the mixed conducting properties and transistor performance of P3HT-*co*-P3HHT by blending with a PEO homopolymer instead, which might intercept the need for additional synthetic steps to make the block copolymer. However, results show relatively poorer stability of the blends with PEO, implicating the advantages of employing block copolymers.

4.2. Operational stability of blends with P3HT-*b*-PEO

To investigate the operational stability of the devices we track the steady-state and transient performance of OECTs of P3HT-*co*-P3HHT and its blends with P3HT-*b*-PEO over time with prolonged immersion of the transistors in water. To facilitate comparison of the different materials, we test their devices constituting similar channel dimensions ($W = 100 \mu\text{m}$, $L = 10 \mu\text{m}$, $d = 100 \pm 10 \text{ nm}$). The initial performance is measured in aqueous electrolyte, followed by rinsing and continuous storage submerged in water before subsequent characterizations. The devices are measured every other day to every week for over one

month. To minimize the possibility of electrically deteriorating the polymers, the potentials applied are limited to a V_d of -0.4 V and a V_g range of 0.2 to -0.6 V. Sufficiently slow sweep rates are employed when measuring the transfer characteristics of the neat material in order to operate in the saturation regime using lower potentials (according to observations made in section **2.2 OECT characteristics at various operating rates, Figure 2.2**) and yield detectable “on” currents. Finally, the transient behavior of the devices is measured upon application of a V_g step from 0 V (“off”) to -0.6 V (“on”) and held over a period long enough to observe steady state conditions.

4.2.1. Transfer characteristics

Investigation of the transfer characteristics reveals that the OECT of the neat material shows good operational stability while that of the blend shows gradual degradation of its performance with continuous long-term exposure to aqueous media. **Figure 4.1** plots the transfer characteristics and transconductances measured for devices of P3HT-co-P3HHT and its blends comprising 25 wt% P3HT-*b*-PEO. The OECT of the neat material does not display significant deterioration of its “on” currents and transconductances during one month of continuous immersion in water, which suggests that the structural and mixed conducting properties of the P3HT-co-P3HHT film is sturdy in ambient, aqueous environment. Meanwhile, the blend exhibits only small decrease of the “on” currents and slightly larger current hysteresis after one week. However, after two weeks being stored in water, significant decrease of the transconductance is eventually observed. These findings could indicate either degradation of the electronic conductivity in the blend or simply slower device response relative to the operating speed (50 mV s^{-1}).

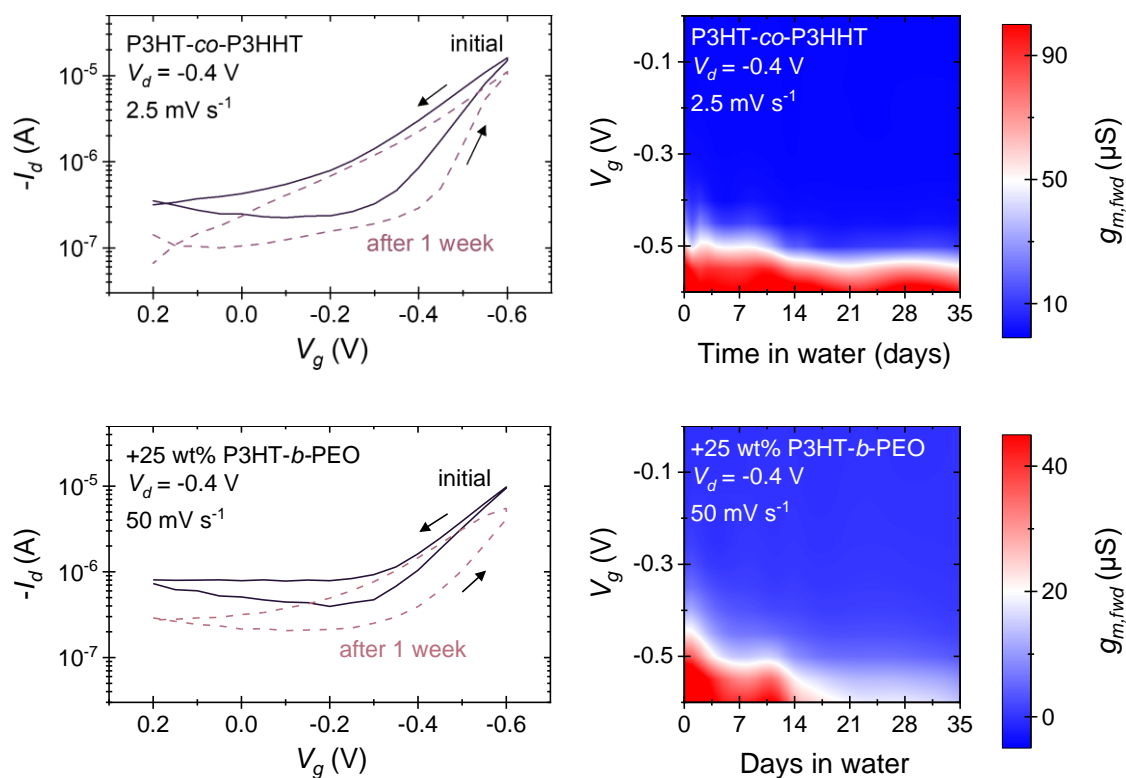


Figure 4.1. OECT transfer characteristics of P3HT-co-P3HHT and its blends with P3HT-b-PEO before and after 1 week of repeated measurements and storage in water (left). Color maps showing evolution of g_m in devices constantly stored in water over time (right).

4.2.1. Transient performance

Inspection of the transient currents in both devices, plotted in **Figure 4.2** for measurements made over one month while storing the OECTs in water, reveals that only the transistor time constant (τ) changes while the steady state currents (I_{SS}) are sustained. OECTs of the neat material and its blend with P3HT-b-PEO display I_{SS} approaching 10^{-5} ($I_{on/off} \approx 10^3$) even after one month of repeated measurement and immersion in water. On the other hand, the values of τ indicated by the shoulders on the drain current transients are observed to decrease for both material systems. The neat material, which already shows initially long response times lasting up to 10 s, exhibits slightly further increase of τ over time. However, the device of the blend exhibits more significant change of τ from an initial

value of 80 ms to about 5 s after a month, two orders of magnitude higher, which explains the conspicuous decline of the drain currents and transconductances observed uniquely in the transfer curves of the blend. We attribute this to less efficient charge injection resulting from prolonged exposure to water that may have been preceded by the disintegration of the blend induced by the water-soluble, low molecular weight PEO component.

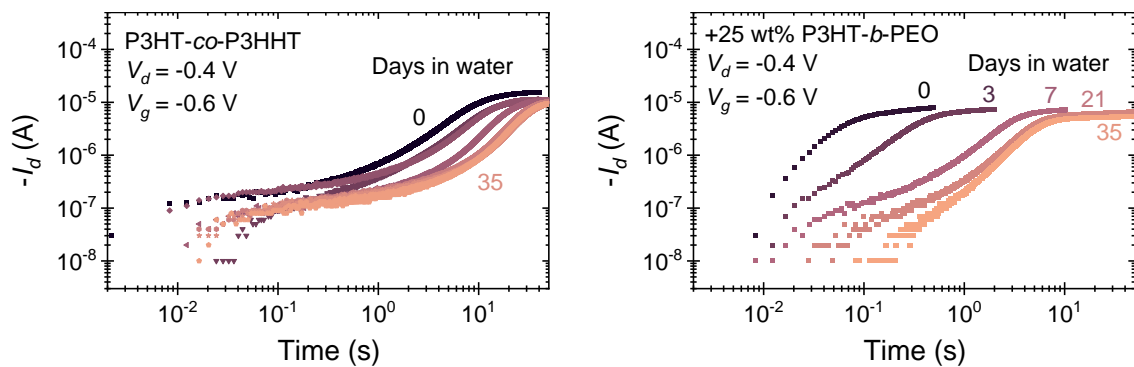


Figure 4.2. Evolution of OECT I_d transients from devices of P3HT-co-P3HHT and its blend with P3HT-b-PEO stored in water over time.

4.2.2. Stability in water: preliminary QCM investigation

To further explore the instability observed in the OECTs of the blends, we qualitatively investigated the robustness of the films when submerged in water using a quartz crystal microbalance (QCM) technique. Deposition of a thin film onto a piezoelectric quartz crystal resonator leads to a shift in its resonant frequency (Δf) inversely proportional to the mass of the film (Δm), as indicated by the Sauerbrey approximation given in **Equation 4.1**.¹

$$\Delta f = -C_f \cdot \Delta m \quad 4.1$$

where C_f is the mass sensitivity factor specific to the quartz sensor (56.6 Hz μg^{-1} cm^2 for a 5 MHz crystal driven at its fundamental frequency). Thus, an increase of the resonance frequency typically indicates a decrease of mass at the surface of the sensor.

We note that quantification of mass changes using **Equation 4.1** is only possible in the case of homogeneous rigid thin film coatings such as metals or dry polymers. However, when analyzing soft viscoelastic materials like polymer films in contact with a liquid, the viscoelastic properties of the material and the surrounding liquid must be considered for accurate calculation of mass changes since these can effectively dampen the crystal oscillation.^{2,3} It is therefore useful to measure both Δf and the dissipation factor (ΔD) describing the oscillation damping, which can be related by viscoelastic models to the deposited material's thickness, density, viscosity, and shear modulus, as well as the density and viscosity of the surrounding media.⁴ Furthermore, for more accurate fits of the data to such models, measurements are typically done at multiple higher-order overtones of the fundamental frequency ($n = 3, 5, 7, 9, 11, \text{ and } 13$).⁵ However, due to the limitations of the QCM equipment used in this work (see appendix section **A.5 Quartz crystal microbalance** for details on instrumentation and methodology), we could not access ΔD nor Δf at higher-order overtones $n > 1$. Therefore, the preliminary results presented here provide only a crude first impression of the behavior of the films when immersed in water.

The resonance frequency of the blank quartz sensors were first tested in “dry” conditions ($f_0 \approx 5$ MHz for AT-cut and polished quartz crystals with chromium/gold electrodes) under nitrogen flow (0.5 L min^{-1}) in a sealed chamber and in “wet” conditions ($\Delta f_{0,wet} = f - f_0$) by immersing the sensor holder in a water bath, allowing 60-90 minutes in each state for the signal to stabilize. The sensors were then coated with the polymer films by spin-casting their solutions following the same protocols used for OECT fabrication. Once dry, the frequencies of the coated sensors were measured under dry ($\Delta f_{dry} = f - f_0$) and wet conditions over several cycles ($\Delta f_{wet,x} = f - \Delta f_{0,wet}$, where $x = \text{cycle ordinal number}$).

After each measurement in wet conditions, the sensors were lightly rinsed with water and allowed to dry under nitrogen flow, then re-immersed in the water bath for subsequent measurements. At least three dry-wet cycles ($x = 3$) were recorded for each material system. Further details on the methodology may be found in the appendix.

Results from QCM measurements on P3HT-co-P3HHT plotted in **Figure 4.3** suggest that the film is structurally stable when immersed in water. A quartz sensor coated with the neat material exhibits a frequency shift of $\Delta f_{dry} \approx -0.61$ kHz relative to the initial frequency of the uncoated sensor in nitrogen gas environment. According to **Equation 4.1**, this is equivalent to an areal density of $11 \mu\text{g cm}^{-2}$, which, assuming uniform thickness over the sensor area and a volumetric density of 1 g cm^{-3} , translates to a film thickness of about 110 nm matching results from profilometry measurements on previous films spun-cast using the same parameters.

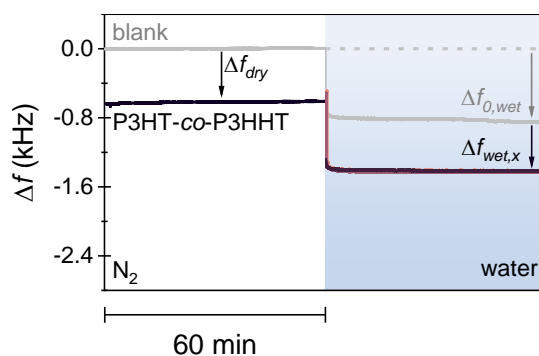


Figure 4.3. Shifts of the fundamental frequency (overtone order $n = 1$) of a QCM sensor before (“blank”) and after coating with P3HT-co-P3HHT, measured under N_2 gas atmosphere (Δf_{dry}) and while immersed in water ($\Delta f_{wet,x}$) for x consecutive dry-wet cycles (dark to light pink solid lines indicate $x = 1, 2,$ and $3,$ in that order). The frequency change upon immersing the blank quartz crystal sensor in water is also shown ($\Delta f_{wet,0}$).

In water, the frequency of the crystal decreases further due to damping of the crystal oscillation. The uncoated sensor exhibits $\Delta f_{0,wet} \approx -0.85$ kHz in water relative to the dry state. Meanwhile, the same sensor coated with P3HT-co-P3HHT shows $f - \Delta f_{0,wet} = \Delta f_{wet,1} \approx -0.57$ kHz relative to the wet uncoated sensor. The close values of $\Delta f_{wet,1}$ and Δf_{dry} could suggest that the mass of the deposited P3HT-co-P3HHT does not really change during the first immersion in water. Furthermore, no significant change of the frequency is observed after consecutive dry-wet cycles ($\Delta f_{wet,1} = \Delta f_{wet,2} = \Delta f_{wet,3}$), implying that films of P3HT-co-P3HHT are mechanically stable in water-rich environments.

While the mechanical properties of P3HT-co-P3HHT appear to be insensitive to aqueous environments, the QCM response of the blend is observed to undergo more significant changes upon immersion in water, as shown in **Figure 4.4**. Coating a sensor with the blend results in $\Delta f_{dry} \approx -0.94$ kHz, from which a thickness of about 170 nm is estimated, which is within range of the values measured from profilometry for spun-cast films at similar conditions. During the first immersion in water, $\Delta f_{wet,1}$ is measured at about -1.2 kHz, 0.26 kHz less than Δf_{dry} indicating at least 40 nm of thickness increase ($\geq +24\%$), which might result from swelling of the film. Similar behavior has been observed for films of p(g2T-TT) and crosslinked PEDOT:PSS that swell by up to 15% and 85%, respectively, in wet conditions.⁶⁸ Furthermore, the frequency measured during the second and third immersion of the blend-coated sensor at $\Delta f_{wet,2} = \Delta f_{wet,3} \approx -1.1$ kHz is 0.1 kHz higher than that of the first immersion, $\Delta f_{wet,1}$, translating to a decrease in areal mass by about $2 \mu\text{g cm}^{-2}$ ($\approx -10\%$). This suggests that blends with P3HT-*b*-PEO are susceptible to both swelling and loss of material when exposed to water-rich environments, which might explain how the initially fast response speed of their OECTs eventually slows down over time.

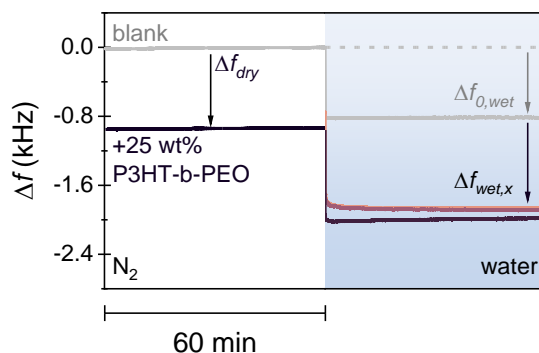


Figure 4.4. Shifts in the frequency (overtone order $n = 1$) of QCM sensors before (“blank”) and after coating with the 25 wt% P3HT-b-PEO blend under N_2 gas (Δf_{dry}), and in water ($\Delta f_{wet,x}$) for x consecutive dry-wet cycles (dark to light pink solid lines indicate $x = 1, 2,$ and $3,$ in that order).

4.3. Blends of P3HT-co-P3HHT with PEO

To investigate whether the instability observed in the transient performance of the blends is driven by the solubility of the PEO moiety, we examine the properties of P3HT-co-P3HHT blended with a PEO homopolymer of similar molecular weight as that in the block copolymer ($M_{n,PEO} \approx 20 \text{ kg mol}^{-1}$). First, we determine whether we can also achieve compatible blends processed from solution without chemically linking the PEO with a P3HT-block, using the same film-deposition protocols as that of blends with the block copolymer. We then investigate the electrochemical properties of these materials to forecast the performance of their devices.

4.3.1. Physical properties

Inspection of the thermal properties extracted from the thermograms plotted in **Figure 4.5** and tabulated in **Table 4.1** provides evidence of a phase-separated blend. The first heat trace of the solution-processed blend shows distinct endotherms attributed to PEO

($T_{m1,end} = 70\text{ }^{\circ}\text{C}$, $\Delta H_1 = 159\text{ J g}^{-1}$) and P3HT-co-P3HHT ($T_{m2,end} = 254\text{ }^{\circ}\text{C}$, $\Delta H_2 = 40\text{ J g}^{-1}$) melting. Both melting temperatures are depressed relative to those in the neat films ($T_{m,PEO} = 71\text{ }^{\circ}\text{C}$ and $T_{m,P3HT-co-P3HHT} = 259\text{ }^{\circ}\text{C}$), indicating smaller crystals, while the normalized melting enthalpy of PEO in the blend is lower than that of its neat film ($\Delta H_{PEO} = 171\text{ J g}^{-1}$). Although this might indicate compatibility, we observe in the left panel of **Figure 4.6** that the melting enthalpies of each phase from the first heat scan align almost exactly with the expected values for completely phase separated components, which implies that the solution-cast blend with the PEO homopolymer is significantly less compatible compared to the blend with the block copolymer (see section **3.2.2 Thermal properties, Figure 3.4**).

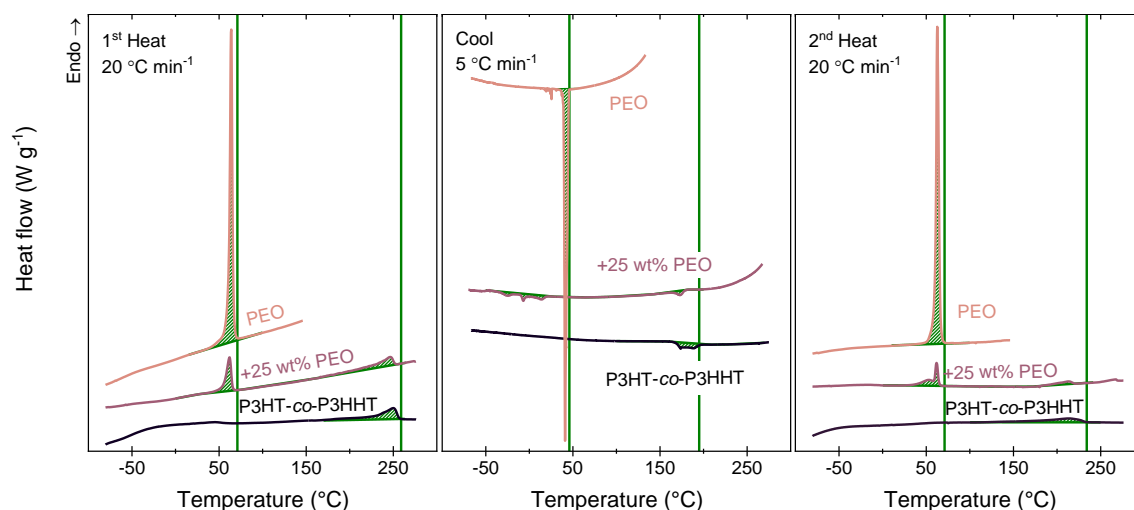


Figure 4.5. Thermograms of P3HT-co-P3HHT and its blend with PEO during the 1st heat, cool, and 2nd heat scans.

Table 4.1. Transition temperatures and enthalpies from thermograms of P3HT-co-P3HHT and its blends with PEO.

PEO content (wt%)	Mass (mg)	1 st Heat				Cool				2 nd Heat			
		$T_{m1,end}$ (°C)	ΔH_1^a (J g ⁻¹)	$T_{m2,end}$ (°C)	ΔH_2^b (J g ⁻¹)	$T_{c1,on}$ (°C)	ΔH_1^a (J g ⁻¹)	$T_{c2,on}$ (°C)	ΔH_2^b (J g ⁻¹)	$T_{m1,end}$ (°C)	ΔH_1^a (J g ⁻¹)	$T_{m2,end}$ (°C)	ΔH_2^b (J g ⁻¹)
0	1.6	--	--	259	40	--	--	195	-17	--	--	233	26
25	1.4	70	159	254	40	20	-77	178	-6	68	91	220	10
100	1.3	71	171	--	--	46	-157	--	--	71	162	--	--

^a Normalized to weight fraction of PEO moiety; ^b Normalized to weight fraction of P3HT and P3HHT moieties;

On the other hand, the cooling traces show significantly suppressed crystallization of PEO and P3HT-co-P3HHT in the blend leading to lower enthalpies and larger supercooling ($\Delta T = T_{m,end}(2^{nd} \text{ heat}) - T_c$) compared to the neat materials. This might indicate that the melt-process blend with PEO is compatible, which is also reflected in the right panel of **Figure 4.6**. This suggests sufficient interaction between PEO and P3HT-co-P3HHT, which appears to be diluted when processed from solution.

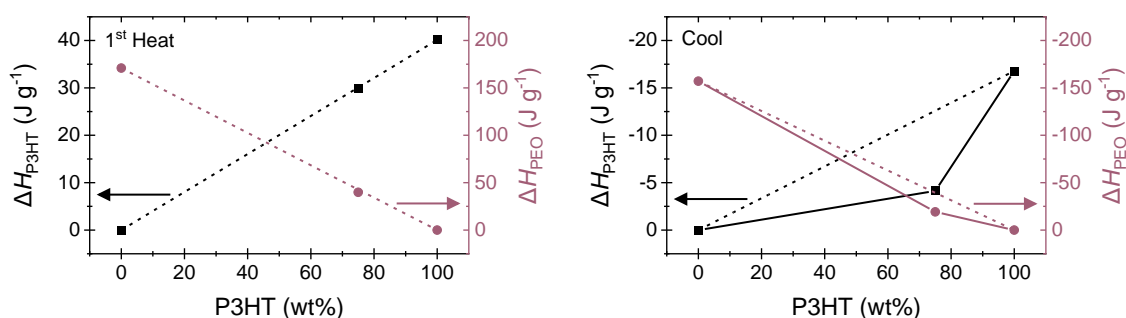


Figure 4.6. Enthalpies of the P3HT (black, left axis) and PEO (pink, right axis) moieties in blends of P3HT-co-P3HHT and PEO cast from solution (left) and cooled from the melt (right), extracted from thermograms. The dashed lines indicate “ideal” values for completely phase-separated components.

Phase separation in the solution-cast blend seems to be limited to very fine length scales. This is indicated by the absence of large-scale phase separation observable in the microscopy images of the blends with PEO, shown in **Figure 4.7**, even when viewed in cross-polarized mode to detect birefringence.

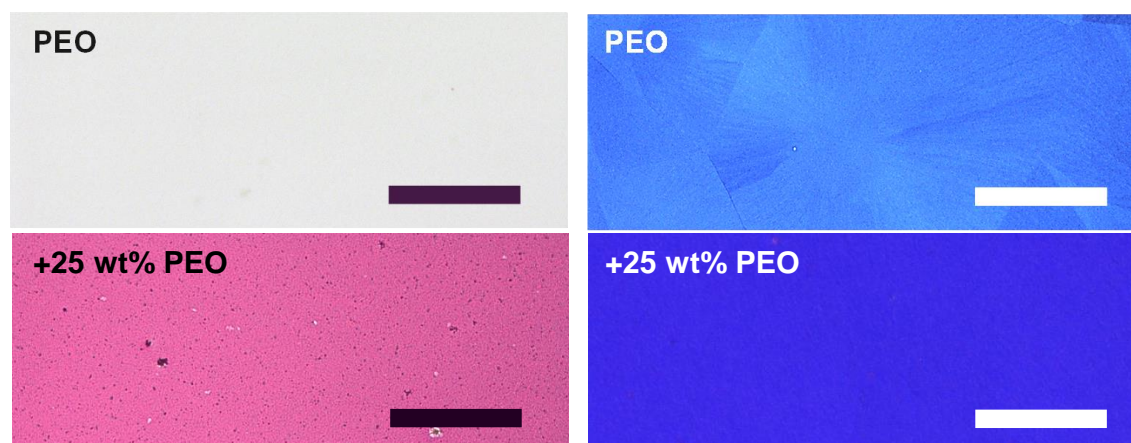


Figure 4.7. Optical microscopy images of PEO and its blend with P3HT-co-P3HHT in transmittance mode (left) and corresponding cross-polarized mode (right), showing no large-scale phase separation. Scale bar measures 200 μm .

Meanwhile, we do not observe large differences in the local molecular ordering of P3HT-co-P3HHT upon blending with PEO. Specifically, the UV-Vis absorption spectra of the blend given in **Figure 4.8** is almost identical with that of the neat P3HT-co-P3HHT and shows only slightly higher A_{0-0}/A_{0-1} intensity ratio. The small influence of blending on the optical properties could reflect minimal interaction of the components due to their microphase separation as implied by the thermal properties of the solution-cast blend.

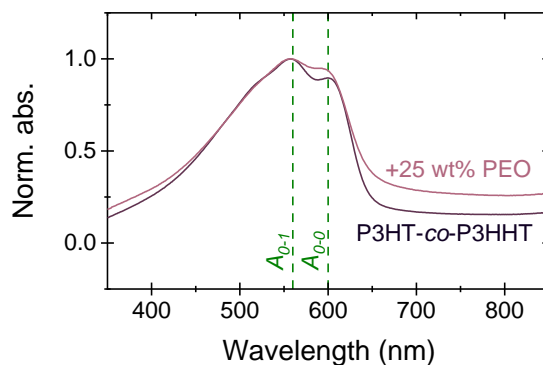


Figure 4.8. UV-Vis absorption spectra of P3HT-co-P3HHT and its blend with PEO.

While blending with PEO does not strongly influence the short-range order of P3HT-co-P3HHT when compared to the neat material, it does seem to increase the hydrophilicity of the films, much like the effect of blending with the block copolymer. **Figure 4.9** plots the water contact angles measured for the neat P3HT-co-P3HHT and its blends with 25 wt% P3HT-*b*-PEO and 25 wt% PEO.

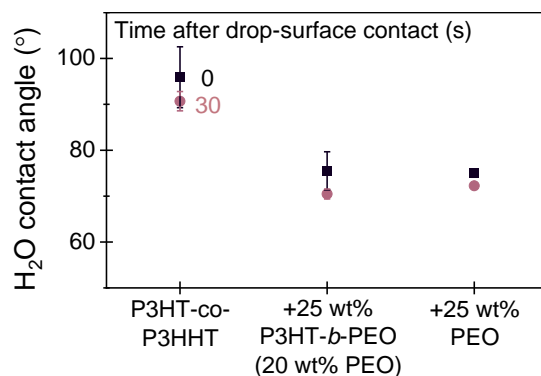


Figure 4.9. Water contact angles of P3HT-co-P3HHT and its blends with P3HT-*b*-PEO and PEO.

Intriguingly, the angle decreases and approaches 70° in both blend systems despite there being even less PEO fraction in blends with the block copolymer (e.g., 20 wt% PEO

in a blend with 25 wt% P3HT-*b*-PEO according to its molecular weight fraction). This suggests that the hydrophobic P3HT-block linked to PEO does not limit its influence on the hydrophilicity of the blends and that the trend saturates at low PEO compositions. Indeed, we find from plotting the compiled data from measuring both blend systems in **Figure 4.10** that no further significant decrease of the contact angle can be achieved at compositions above 20 wt% PEO. This leads us to predict that we can enhance the electrochemical properties of the material operating in aqueous conditions, linked to its hydrophilicity, by blending with PEO at relatively low compositions.

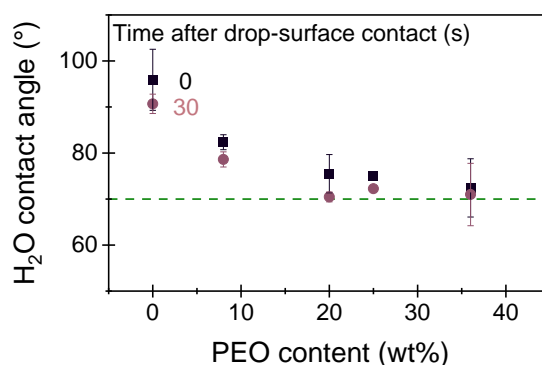


Figure 4.10. Compiled water contact angles measured from blends with P3HT-*b*-PEO and PEO, showing plateau above 20 wt% PEO.

4.3.2. Electrochemical properties

The strong similarities between the physical properties of the blends comprising either P3HT-*b*-PEO or the PEO homopolymer allows us to predict that adding PEO should also enhance the transient electrochemical properties of the material. We begin by verifying that blending with PEO does not drastically change its charging behavior relative to that of the neat material or its blend with the block copolymer through comparing their cyclic

voltammograms measured in aqueous electrolyte (0.1 M KCl), given in **Figure 4.11**. The PEO blends do exhibit oxidation onsets and peak anodic potentials close to that of the blends with the block copolymer and the neat P3HT-*co*-P3HHT, as indicated in **Table 4.2**. Thus, we use similar potentials to operate and compare electrodes of the different materials.

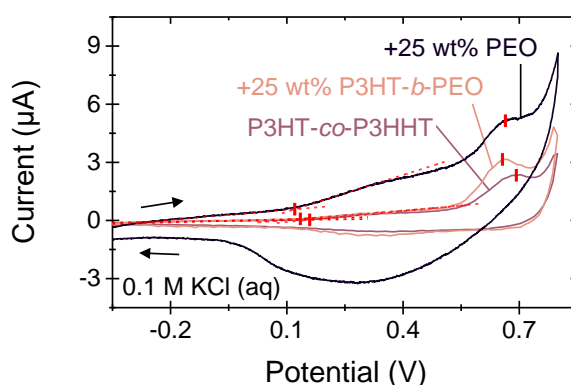


Figure 4.11. Cyclic voltammograms of films of P3HT-*co*-P3HHT and its blend with PEO in aqueous electrolyte measured at a scan rate of 2 mV s⁻¹. Oxidation onsets and peaks are indicated (dashed red lines and ticks). Blend with P3HT-*b*-PEO is also shown for comparison.

Table 4.2. Oxidation onsets and peaks extracted from voltammograms of polymers measured against Ag/AgCl as reference at 2 mV s⁻¹ in 0.1 M KCl.

Polymer	$E_{ox,on}$ (V)	E_{pa} (V)
P3HT- <i>co</i> -P3HHT	0.16	0.69
+ 25 wt% P3HT- <i>b</i> -PEO	0.12	0.66
+ 25 wt% PEO	0.14	0.66

Further examination of the oxidation behavior using spectroelectrochemistry to probe the electrochemical doping kinetics reveals that blending with PEO does indeed

accelerate doping of the material with aqueous electrolyte. The absorption spectra change depicted in **Figure 4.12** reflects oxidation of the thiophene aggregates and formation of positive polarons (p-type doping) upon application of bias (0.75 V). The peak absorption ($\lambda = 560$ nm) decreases to half the initial value (*norm. abs.* ≈ 0.5) at steady state within 500 ms, faster than what was observed for the neat P3HT-*co*-P3HHT (see section **3.3.2.1 Electrochemical bleaching, Figure 3.11**).

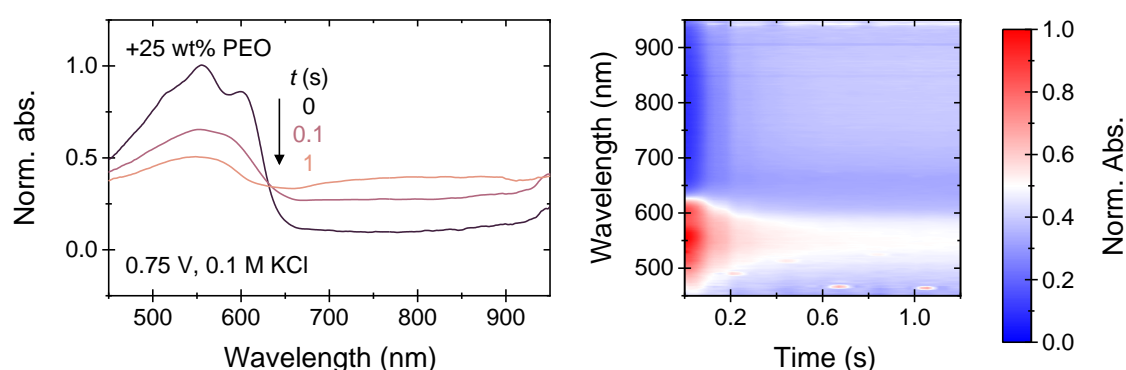


Figure 4.12. Evolution of absorption spectra over time upon application of a step bias (0.75 V) to a blend of P3HT-*co*-P3HHT and PEO cast on an ITO electrode in aqueous electrolyte.

Closer inspection of the relative peak absorption changes, given in the left panel of **Figure 4.13** for different film thicknesses (d), allows us to extract the electrochemical doping rates (k) by fitting the data with a first-order kinetic model in the form of a monophasic exponential function (described further in section **3.3.2.3 Monophasic exponential kinetic model**). Steeper transients resulting in higher rate constants are measured for thinner films, signifying bulk doping phenomena, as expected for mixed conducting polymers. Additionally, in comparing the different materials, we find that blends with either PEO or P3HT-*b*-PEO exhibit almost equivalent rate constants over different film thicknesses, as indicated by the overlap of their k -versus- d plots in the right panel of **Figure 4.13**.

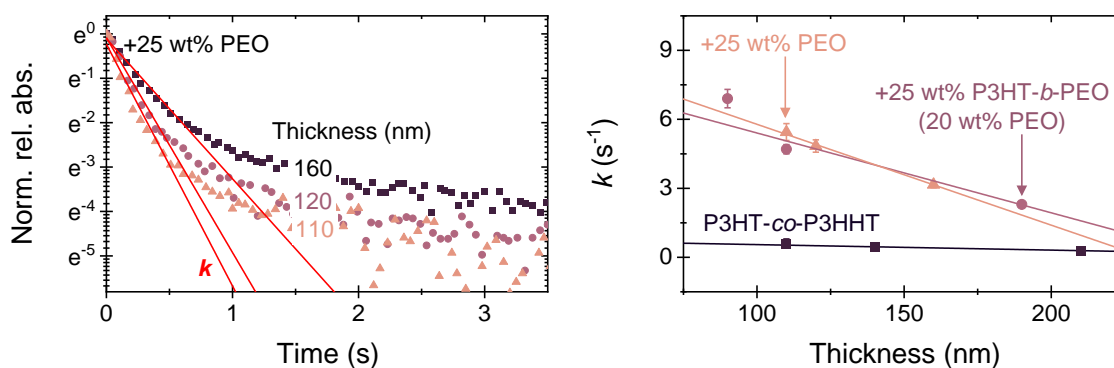


Figure 4.13. Normalized absorption change (rescaled 0 to 1) at initial peak wavelength ($\lambda = 560$ nm) in blends with PEO of various thicknesses (left). Doping rates (k) plotted against thickness for P3HT-co-P3HHT and its blends with P3HT-b-PEO and PEO (right).

It follows that the regression slopes of the k - d plots corresponding to the thickness-normalized rate constants (kd^{-1}) are virtually the same for blends comprising either 25 wt% PEO (44 ± 2 s $^{-1}$ μm^{-1}) or 25 wt% P3HT-*b*-PEO (35 ± 8 s $^{-1}$ μm^{-1}), despite the latter containing less PEO fraction (20 wt% PEO), which suggests that the effect of PEO on the transient electrochemical properties of the material saturates at low compositions. To investigate this further, we compile the kd^{-1} values obtained for the different blend systems and plot them according to PEO content in **Figure 4.14**. Significant enhancement of the rate constants in the blends is displayed only up to $kd^{-1} \approx 40$ s $^{-1}$ μm^{-1} at a composition of 20 wt% PEO, above which no further increase is achieved. This is reminiscent of the trend observed in the water contact angles of the materials, also plotted in **Figure 4.14** (right axis) for comparison, indicating a correlation between surface hydrophilicity and efficiency of ion uptake during electrochemical device operation in water-rich media.

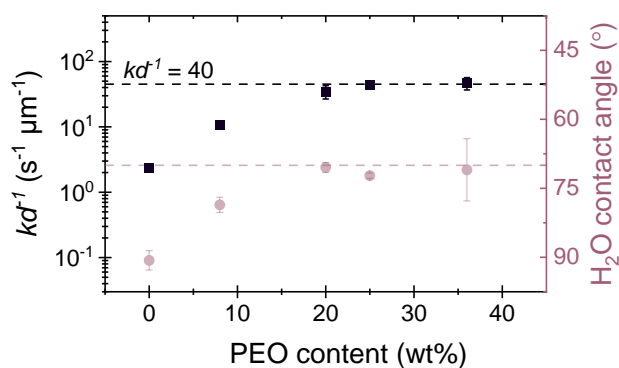


Figure 4.14. Thickness-normalized rate constants (kd^1) plotted against PEO content using compiled data from blends with either PEO or P3HT-*b*-PEO, showing a plateau of the rate increase above 20 wt% PEO. Data from water contact angle measurements also shown (pink transparent plot, right axis) for comparison.

Blending with PEO also influences the mid-frequency complex impedance response of the material much like blending with the block copolymer (see section **3.3.3 Impedance behavior**). In **Figure 4.15** we recall that the impedance behavior observed in the neat P3HT-*co*-P3HHT exhibits a plateau of the impedance magnitude ($|Z|$) and imaginary impedance (Z_{im}) between the frequency range $10 \text{ Hz} < f < 10^3 \text{ Hz}$, a local peak of the phase angle to -30° at around 200 Hz, and a depressed semi-circle in the Nyquist plots ($-Z_{im}$ vs Z_{re}). We speculate this is due to effects resulting from inefficient ion diffusion across polymer-electrolyte interface. Blending with PEO appears to minimize this effect as indicated by the decrease of the mid-frequency $|Z|$ and Z_{im} , lowering of the phase angles to almost 0° , and suppression of the semi-circle feature in the Nyquist plot. Thus, this might correlate with the enhanced ion uptake efficiency in the blends observed from spectroelectrochemistry.

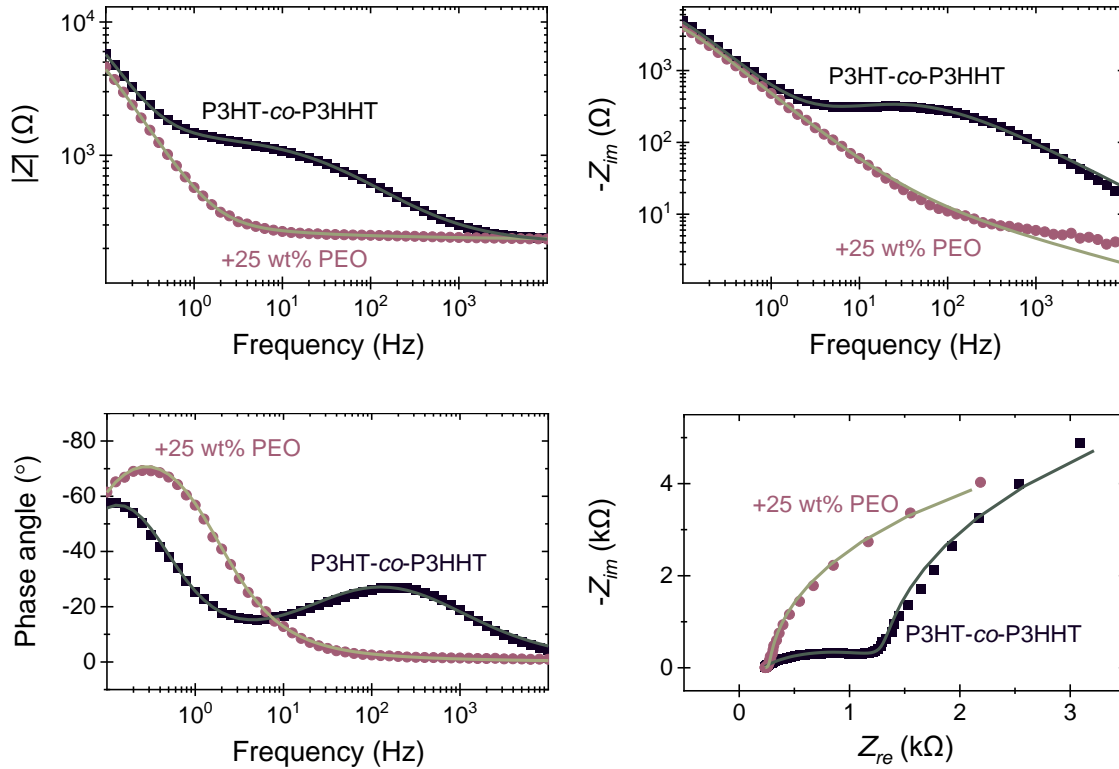


Figure 4.15. Impedance magnitude ($|Z|$, top-left), imaginary impedance ($-Z_{im}$, top-right) and phase angle (bottom-left) plotted against frequency, and Nyquist plots (Z_{re} vs $-Z_{im}$, bottom-right) of P3HT-co-P3HHT and its blends with PEO. Scatter plots refer to experimental data while solid lines correspond to equivalent circuit model fits.

Table 4.3. Parameters extracted from equivalent circuit model fits to EIS spectra measured for blends with PEO.

PEO content (wt%)	Thickness (nm)	R_S (Ω)	Q ($\mu\text{S s}^n$)	n	R_i (Ω)	R_p (k Ω)	C (μF)	C^* (F cm $^{-3}$)
25	110 \pm 10	234	5700	0.34	140	10	340	190 \pm 30
	120 \pm 10	230	3300	0.30	170	11	400	
	160 \pm 10	260	4000	0.30	220	7.5	640	

Fitting the impedance data with an appropriate equivalent circuit model allows us to extract the capacitance of the doped material of known thickness, from which the volumetric capacitance (C^*) may be calculated. A modified Randle's circuit ($R_S(\text{CPE}_i||R_i)(C||R_p)$, see

also section **3.3.3.1 Equivalent circuit model-fitting**) is employed to fit the experimental data (solid lines in **Figure 4.15**) and extract the parameters tabulated in **Table 4.3**. For the blend with PEO, we determine a C^* value of about $200 \pm 30 \text{ F cm}^{-3}$, which is essentially the same as that obtained for the blends with the block copolymer and the neat P3HT-co-P3HHT, as shown in **Figure 4.16**.

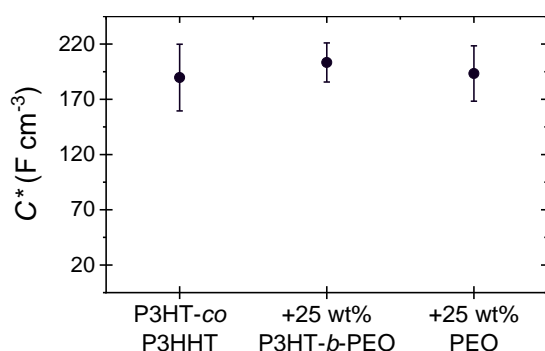


Figure 4.16. Summary of volumetric capacitances, C^* , calculated from values extracted from equivalent circuit model fits to impedance data of P3HT-co-P3HHT and its blends with P3HT-b-PEO and PEO.

Assuming that C^* results from combined double-layer capacitances formed between injected ions and charged polarons in mixed conductors,⁷ this implies that adding PEO does not apparently change the polaron density of the electrochemically doped material. Again, we suspect this may be due to a large fraction of the neat material not participating in polaron formation nor electronic conduction (see section **3.3.3.2 Volumetric capacitance, C^***). Thus, we expect similar steady state current output and transduction performance from the electrochemical transistors of the neat P3HT-co-P3HHT and its blend with PEO.

4.3.3. OECT performance

Characterization of OECTs fabricated with the blends confirms that adding the PEO component, even without a chemically attached P3HT-block, to the channel material enhances the device response speed while maintaining its steady state performance. Specifically, inspection of the OECT output curves of the blend with PEO in the top panel of **Figure 4.17** shows that the onset of saturation of the drain current with applied drain voltage occurs at V_d as low as -0.3 V for a sweep rate of 0.5 V s⁻¹. Additionally, the transfer curves measured for the blends with PEO in the bottom panel of **Figure 4.17** show minimal hysteresis even at V_g sweep rates higher than 1 V s⁻¹ and relatively reproducible maximum I_d across a wide range of operating speeds. This is unlike the OECTs of the neat P3HT-co-P3HHT, which only show I_d saturation at V_d more negative than -0.7 V for a V_d sweep rate of 0.5 V s⁻¹, large hysteresis in their transfer curves, and significant decrease of their $I_{d,max}$ with faster V_g sweep rates from 0.01 to 0.5 V s⁻¹ (see results in section **2.2.1 P3HT-co-P3HHT**), indicating much slower response speeds than devices of the blends. Meanwhile, blending does not seem to change the OECT threshold voltage at $V_t \approx -0.5$ V, $I_{d,max}$ of around 60 μ A, and $g_{m,max}$ of 0.4 mS relative to that of the neat P3HT-co-P3HHT measured at the same biasing conditions ($V_g(I_{d,max}) = -0.8$ V, $V_d = -0.6$ V), channel dimensions ($W = 100$ μ m, $L = 50$ μ m, and $d = 100$ nm), and slow V_g sweep rates (0.06 V s⁻¹). Accordingly, OECTs of the blend with PEO exhibit a relatively low response time of $\tau = 70$ ms, extracted from the transient drain current measured upon application of a V_g step (0 to -0.6 V at $V_d = -0.4$ V) and depicted in **Figure 4.18**.

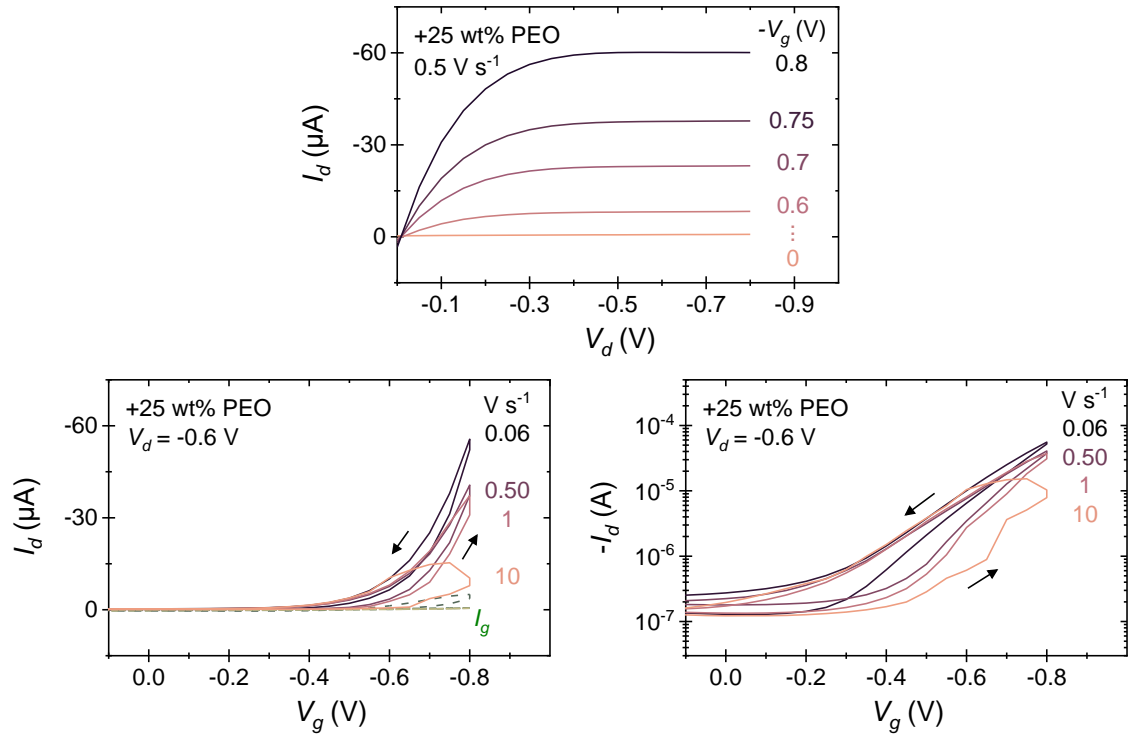


Figure 4.17. OECT output (top) and transfer characteristics (bottom) plotted linearly (left) and logarithmically (right) for a blend of P3HT-co-P3HHT and PEO measured at various V_g sweep rates as indicated.

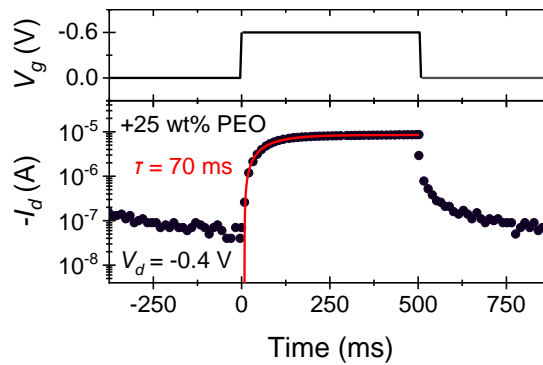


Figure 4.18. OECT transient performance upon application of a V_g pulse for a blend of P3HT-co-P3HHT and PEO. The time constant extracted from an exponential fit (solid red line) is shown.

Again, this indicates faster speed than devices of the neat P3HT-co-P3HHT for which τ is as high as 8 s at the same biasing conditions (see **2.5 Transient response, Figure 2.17**). Not surprisingly, the OECT response time for blends with 25 wt% PEO is almost identical to that of the blends with 25 wt% P3HT-*b*-PEO ($\tau = 80$ ms), which we relate to maximization of the doping rates at 20 wt% PEO based on the results from spectroelectrochemical analysis.

Characterization of several devices of the blend with PEO and examination of their transconductances (g_m) plotted in **Figure 4.19** allows us to extract the μC^* parameter, which describes the mixed conducting performance of the active channel material independent of the channel dimensions and biasing. A value of about $14 \text{ F cm}^{-1} \text{ V}^{-1} \text{ s}^{-1}$ is obtained for the blend with 25 wt% PEO, which is within the range of values obtained for the neat P3HT-co-P3HHT and its blends with P3HT-*b*-PEO (10 to $55 \text{ F cm}^{-1} \text{ V}^{-1} \text{ s}^{-1}$). Thus, we establish that blending the mixed conducting P3HT-co-P3HHT with the electronically insulating PEO homopolymer is also a feasible strategy to enhance its transient electrochemical behavior and, subsequently, the response speed of its devices without losing its electronic properties.

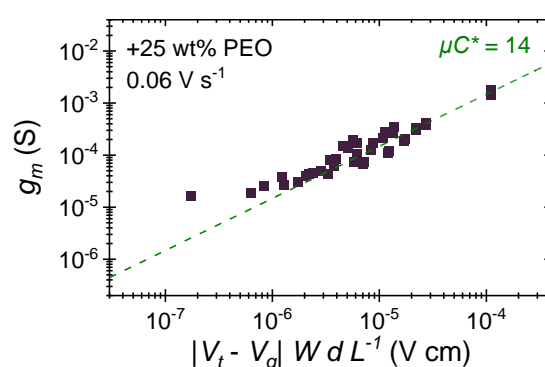


Figure 4.19. Scaling of g_m with $|V_t - V_g| W d L^{-1}$ for OECTs of blends of P3HT-co-P3HHT and PEO at the indicated V_g sweep rate. μC^* extracted from model fit (dashed green line) is shown.

4.4. Stability of blends with PEO

Having determined that blending the mixed conductor with PEO can efficiently enhance its transient electrochemical properties and transistor performance, we proceed to examine their long-term operational stability in aqueous context with reference to the instability observed in the blends of the block copolymer. We predict that, without the P3HT-segment chemically linked to the PEO to limit its solubility in water, the structural stability of the blends and their subsequent long-term device performance will be relatively poor.

4.4.1. Preliminary QCM analysis

QCM measurements of the blends with PEO plotted in **Figure 4.20** do seem to indicate that the film partially delaminates when immersed in water. The quartz sensor exhibits a frequency shift of $\Delta f_{dry} \approx -1$ kHz relative to the initial frequency of the uncoated sensor in the dry state. Using **Equation 4.1**, this is equivalent to an areal density of about $18 \mu\text{g cm}^{-1}$ and translates to a film thickness of approximately 180 nm, which is near the values of the thickness measured using profilometry on previous films cast using similar protocols. During the first immersion in water the frequency of the coated quartz decreases further to about -1.8 kHz, yielding a difference of $\Delta f_{wet,1} \approx -0.9$ Hz between the wet coated sensor and wet uncoated sensor ($\Delta f_{0,wet} \approx -0.87$ Hz). The change from Δf_{dry} to $\Delta f_{wet,1}$ by about +0.1 Hz might suggest that during the first immersion in water the film already starts to lose around $2 \mu\text{g cm}^{-1}$ worth of material ($\approx -10\%$). In subsequent immersions the frequency shifts even more to $\Delta f_{wet,2} = \Delta f_{wet,3} \approx -0.8$ Hz, equivalent to a total change of +0.2 Hz relative to the dry coated sensor and indicating a cumulative decrease of areal mass by approximately $4 \mu\text{g cm}^{-1}$ ($\approx -20\%$). Conversely, we recall that the blends with P3HT-*b*-PEO exhibit just up to 10% mass loss, which we observe only after the first immersion (see section **4.2.2 Stability in water: preliminary QCM investigation, Figure 4.4**). We gather

from these preliminary investigations that the blends with PEO potentially disintegrate faster and to a greater extent than the blends with P3HT-*b*-PEO when interfaced with water-rich media.

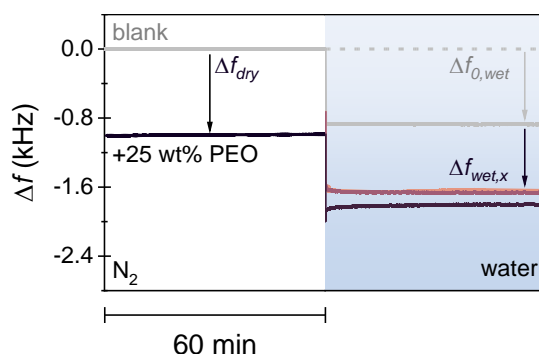


Figure 4.20. Shifts of the fundamental frequency (overtone $n = 1$) of a QCM sensor before (“blank”) and after coating with P3HT-co-P3HHT blended with PEO under N_2 gas atmosphere (Δf_{dry}) and while immersed in water ($\Delta f_{wet,x}$) for x consecutive dry-wet cycles (dark to light pink solid lines indicate $x = 1, 2,$ and $3,$ in that order). The frequency change upon immersing the blank quartz crystal sensor in water is also shown ($\Delta f_{0,wet}$).

4.4.2. OECT transfer characteristics

The mechanical instability observed in the blends with PEO during prolonged exposure to water may inevitably lead to degradation of its electrochemical performance over time. To demonstrate this, we track the OECT characteristics of a blend with PEO while continuously storing the device in water over a month. To prevent electrical overstress of the devices, lower potentials are employed ($V_d = -0.4$ V and $V_g = 0.2$ to -0.6 V). The transfer characteristics plotted in the right panel of **Figure 4.21** clearly evidences the decay of the “on” currents from $I_{ON/OFF} \approx 10^2$ to virtually no current transduction within 1 week of repeatedly measuring and storing the devices in water using the same biasing parameters. It follows that the transconductances extracted from the transfer curves and mapped in the

left panel of **Figure 4.21** decline rapidly, reaching insignificant values after just two days. As expected, the performance loss in devices of the blends with PEO occurs at a faster rate than what was observed for blends with the block copolymer, the latter exhibiting steady transfer characteristics up to two weeks before degradation (refer to **Figure 4.1**).

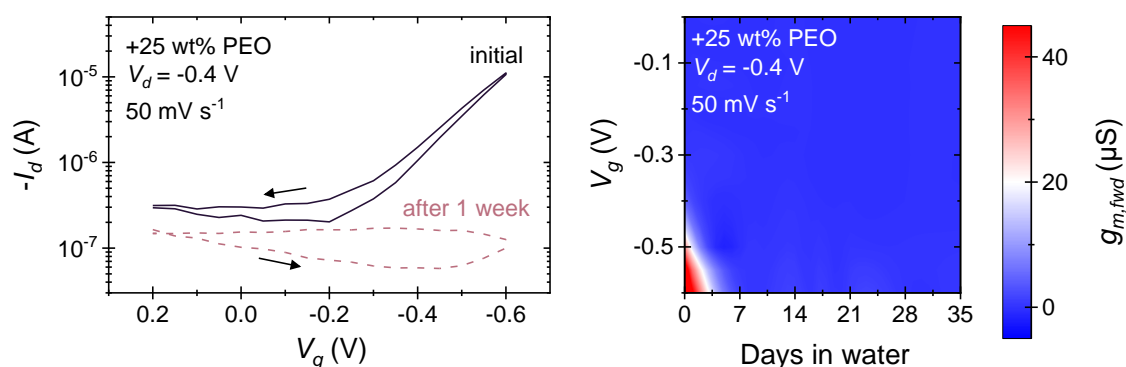


Figure 4.21. OECT transfer characteristics of P3HT-co-P3HHT and its blends with PEO before and after 1 week of repeated measurements and storage in water (left). Color maps showing evolution of g_m in devices stored in water over time (right).

4.4.3. OECT transient characteristics

Examining the evolution of the OECT transient currents during continuous immersion in water over time, depicted in **Figure 4.22**, verifies that the observed loss in performance originates solely from the retardation of the device response and not from diminished electronic properties. Specifically, no significant change in the drain current at steady state (I_{ss}) upon application of a V_g step from 0 to -0.6 V is detected after 1 month, which implies that the conductivity of the doped channel at equilibrium is preserved. This is in accordance with the electronic stability observed in devices of the neat P3HT-co-P3HHT presented here (see **Figure 4.1** and **Figure 4.2**) and in previous work.⁶ On the other hand,

the time constant (τ), indicated by the shoulder of the transient current plots, shifts drastically by two orders of magnitude after only a week.

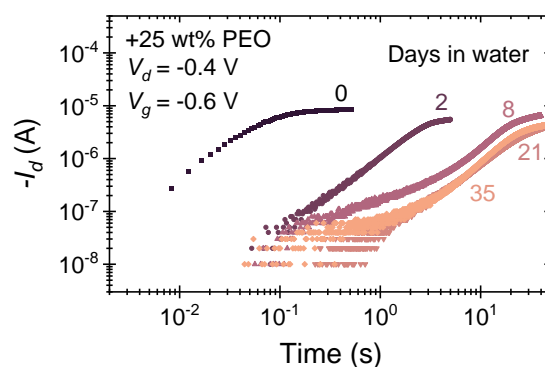


Figure 4.22. Evolution of OECT I_d transients from devices of P3HT-co-P3HHT blended with PEO stored in water over time.

To facilitate comparison and discussion, **Figure 4.23** summarizes the values of I_{SS} and τ extracted from exponential fits to the transient currents measured over one month for the OECTs of each material system. Devices of the neat P3HT-co-P3HHT show steady values of I_{SS} and τ , indicative of its structural and electronic stability against prolonged exposure to aqueous media. It follows then that the blends with PEO or P3HT-*b*-PEO also show sustained I_{SS} over time since this only depends on the properties of the semiconducting component. Conversely, although both blend systems show initially faster performance than the neat material indicated by the lower values of τ , which we attribute to the increased hydrophilicity of the materials as discussed before, the devices do become slower with longer immersion in water. Particularly, the blends with PEO exhibit rapid increase of τ in their OECTs to essentially the same values as that of the neat material after only a week, leading us to suspect that the blends lose a significant fraction of the PEO-rich, ion-conducting phases to the surrounding media. Meanwhile, even though OECTs of the blends with the block copolymer do lose some speed within the first week, they appear

to sustain a τ almost one order lower than the neat material even after one month in water. This might reflect less fraction of the ion-conducting phases lost to the aqueous environment, which would suggest a more structurally stable blend and aligns with the deductions from QCM analysis. We suppose that this behavior is supported by better compatibility of the blend with the block copolymer. The hydrophobic P3HT-block chemically linked to the PEO might also contribute to limiting material dissolution. Notwithstanding that the stability of the transient performance can still be improved further, the results presented here allude to potential advantages in choosing amphiphilic block copolymers as co-components in designing compatibilized mixed conducting polymer blends.

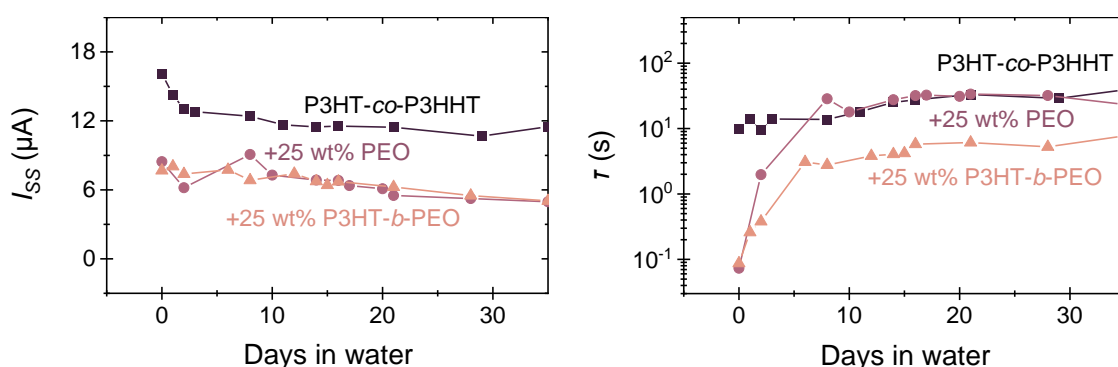


Figure 4.23. Evolution of steady state I_d (I_{ss}) and time constants (τ) extracted from exponential model fits to transient data measured for OECTs of P3HT-co-P3HHT and its blends with P3HT-b-PEO and PEO stored in water over time.

4.5. Summary

Evaluation of the long-term performance of OECTs reveals that the device of the neat P3HT-co-P3HHT exhibits stable operation even after one month of continuous immersion in water. Upon blending with P3HT-b-PEO, although the transistor shows initially enhanced transient performance, its response speed eventually slows down after two

weeks, indicated by an increase of its time constant from $\tau = 80$ ms to about 4 s. Preliminary QCM analysis suggests that the blend may lose around 10% of the material during prolonged exposure to aqueous media, which we attribute to the water-soluble low molecular weight PEO moiety. To test this, we investigate blends of P3HT-co-P3HHT and a PEO homopolymer of the same molecular weight as the PEO moiety in the block copolymer. We find that blending with PEO affects the material properties much like blending with the block copolymer. Specifically, both blend systems show a decrease of the water contact angle to 70° and similar enhancement of the electrochemical doping rates relative to the neat material. This might indicate that the effect of blending on the mixed conductor transient properties is dictated by the PEO moiety. Furthermore, we determine that only up to 20 wt% PEO content in either blend system is needed to effectively modulate the material properties. As a result, OECTs of the blend with PEO show enhanced transient behavior indicated by relatively low response times ($\tau = 70$ ms). Meanwhile, the volumetric capacitance of the blends with PEO is essentially equivalent to that of the neat material (190 ± 30 F cm⁻³). Subsequently, OECTs comprising the PEO blend show similar steady state characteristics and μC^* parameter (14 F cm⁻¹ V⁻¹ s⁻¹) within range of that of the neat P3HT-co-P3HHT (10 - 55 F cm⁻¹ V⁻¹ s⁻¹). Although these results imply that blending with the PEO homopolymer may be a viable method to enhance the properties of the mixed conductor, preliminary QCM analysis suggests that the blends with PEO can exhibit loss of about 20 wt% of material during prolonged exposure to aqueous media, likely due to the water-solubility of the PEO. As a result, its devices exhibit poor long-term operational stability, showing more rapid degradation of its transient performance and to a greater extent, from $\tau = 70$ ms to about 30 s, than that observed in the blend with the block copolymer within a week of continuous storage in water. The superior long-term stability of the blends with the block copolymer might be due to its compatibility and due to the hydrophobic P3HT-block linked to the PEO, which helps limit its solubility and could therefore support the mechanical stability of the blend. These findings imply opportunities

for future research on block copolymer design and engineering as promising co-components to improve the performance and stability of mixed conducting conjugated polymer blends.

4.6. References

1. Sauerbrey, G. Verwendung von Schwingquarzen zur Wägung dünner Schichten und zur Mikrowägung. *Zeitschrift für Phys.* **155**, 206–222 (1959).
2. Easley, A. D. *et al.* A practical guide to quartz crystal microbalance with dissipation monitoring of thin polymer films. *Journal of Polymer Science* pol.20210324 (2021).
3. Kankare, J. Sauerbrey equation of quartz crystal microbalance in liquid medium. *Langmuir* **18**, 7092–7094 (2002).
4. Voinova, M. V, Rodahl, M., Jonson, M. & Kasemo, B. Viscoelastic Acoustic Response of Layered Polymer Films at Fluid-Solid Interfaces: Continuum Mechanics Approach. *Phys. Scr.* **59**, 391 (1999).
5. Johannsmann, D. Viscoelastic analysis of organic thin films on quartz resonators. *Macromol. Chem. Phys* **200**, 501–516 (1999).
6. Nicolini, T. *et al.* A Low-Swelling Polymeric Mixed Conductor Operating in Aqueous Electrolytes. *Adv. Mater.* **33**, 1–7 (2021).
7. Proctor, C. M., Rivnay, J. & Malliaras, G. G. Understanding volumetric capacitance in conducting polymers. *J. Polym. Sci. Part B Polym. Phys.* **54**, 1433–1436 (2016).

General conclusions and perspectives

Our work demonstrates that blending of a mixed conductor with a “compatibilizing” block copolymer is a viable strategy to enhance the transient electrochemical performance of an active material without the need for its direct chemical modification. Specifically, we find that adding hydrophilic, ion-conducting PEO-based additives (P3HT-*b*-PEO block copolymer) to the mixed conducting P3HT-*co*-P3HHT supports faster electrochemical doping of the material in aqueous media. This consequently improves the response speed of its transistors (from $\tau = 8$ s in neat P3HT-*co*-P3HHT to $\tau = 80$ ms in the blends) and appears to be more effective than tuning the geometry of the active channel. We attribute this to enhanced efficiency of ion uptake in the blend due to a more compatible interface with the aqueous electrolyte. Water contact angle measurements do suggest increased hydrophilicity of the material with increasing block copolymer content. This might also explain the reduced mid-frequency impedances observed upon blending if we interpret that the diffusion-dominated impedance response in the neat P3HT-*co*-P3HHT electrodes arises due to limited transport of hydrated ions across the relatively hydrophobic polymer surface. By comparing the trends observed from water contact angle measurements and the electrochemical doping rates extracted from spectroelectrochemistry, we find that only up to 25 wt% of the block copolymer is necessary to achieve efficient modulation of the transient properties by blending.

Results also suggest that our blending approach does not strongly affect the bulk electronic performance of the material. For instance, although counterions penetrate the material faster and, thus, are more readily available in the blends, the volumetric capacitance, which can be related to the polaron density of the electrochemically doped polymer, does not change ($C^* \approx 190$ F cm⁻³). Likewise, the threshold voltages ($V_t \approx 0.45$ - 0.55 V), the transconductances ($g_{m,max} \approx 0.4$ mS), and the steady state currents ($I_{SS} \approx 10^{-5}$ A at $V_g = -0.6$ V and $V_d = -0.4$ V) of the OECTs are preserved, given the same biasing

parameters and device geometry, even after incorporating an electronically insulating component in the channel. We also find that the μC^* performance measured for the neat P3HT-co-P3HHT at practical device operating speeds (≈ 13 to $23 \text{ F cm}^{-1} \text{ V}^{-1} \text{ s}^{-1}$ at sweep rates of 0.5 and 0.25 V s^{-1}) is sustained after blending (≈ 14 - $35 \text{ F cm}^{-1} \text{ V}^{-1} \text{ s}^{-1}$ for blends comprising between 10 and 40 wt\% P3HT-*b*-PEO). These results imply that the electronic conductivity of P3HT-co-P3HHT is virtually unaffected by blending with the PEO-based block copolymer investigated here. This further suggests that a percolation pathway is maintained despite some intermixing of the components as evidenced by the vitrification effect observed in DSC (lowering of melting enthalpies).

Furthermore, we conclude that employing block copolymer “additives” possessing moieties compatible with the mixed conducting component supports the stability of the blend. Specifically, the P3HT-block chemically linked to the PEO compatibilizes its blend with P3HT-co-P3HHT and therefore supports its structural stability and long-term device performance. This is in strong contrast to blends with the PEO homopolymer. Analysis of the thermal properties of both blend systems (blends with the P3HT-*b*-PEO block copolymer and blends with the PEO homopolymer) provides evidence that the blends with the block copolymer exhibit more compatibility than the blend with the PEO homopolymer. Furthermore, preliminary QCM results suggest that films of the blends with the block copolymer “lose” less material upon immersion in water than blends with the PEO homopolymer. This might imply that the hydrophobic P3HT-block helps to limit dissolution or delamination induced by the water-soluble PEO-rich phases. Consequently, upon evaluating the long-term operation stability of OECTs that have been continuously immersed water, devices of the blends with the block copolymer sustain faster transient performance than those of the neat P3HT-co-P3HHT and its blend with the PEO homopolymer. While OECTs comprising P3HT-*b*-PEO do show around 50-fold slower response time after one month stored in water, devices of the blend with the PEO

homopolymer degrade more rapidly (500-fold slower) and approaches that of the devices made of the neat P3HT-*co*-P3HHT.

These results suggest further work focusing on block copolymer engineering to improve the stability and performance of mixed conducting polymer blends. For instance, molecular weights of either moiety in P3HT-*b*-PEO may be increased to offer more robust films when continuously operated in water, but without drastically affecting the mixed conductivity of the material. Additionally, semicrystalline polymer mixtures and block copolymers can follow different solidification pathways that may be manipulated *via* temperature and solution-processing techniques. These may be exploited to control the solid-state structure of resulting films and investigate their consequences on their mixed ionic and electronic conducting properties to establish widely applicable structure-processing--property relationships.

For the general development of new polymeric mixed conductors, polymer blending may provide a way to distinctly manipulate ionic and electronic transport in organic systems, notwithstanding the coupled nature of these processes, by addressing each polymer component and controlling phase separation in the blend (degree of intermixing; length-scale of phase-separation). This promises to open up new avenues for semiconducting polymers and polymer electrolytes that have been originally designed for field effect transistors and batteries. Overall, the blending approach presented in this thesis can be employed in designing materials for applications such as electrochemical biosensing that require fast switching device operation, high signal amplification, and long-term stability.

APPENDIX:

Methodology and supplementary information

A.1. Materials and film deposition	185
A.2. Organic electrochemical transistors (OECT).....	186
A.2.1 Instrumentation	186
A.2.2 OECT device architecture.....	186
A.2.3 OECT measurement parameters	189
A.2.4 OECT operational stability in water	189
A.3. Characterization of physical properties	189
A.3.1 Grazing incidence wide angle x-ray scattering (GIWAXS).....	189
A.3.2 Differential scanning calorimetry	190
A.3.3 Optical microscopy	191
A.3.4 Contact angle measurements	191
A.4. Electrochemical characterization	191
A.4.1 Cyclic voltammetry.....	192
A.4.2 Spectroelectrochemistry	193
A.4.3 Electrochemical impedance spectroscopy	194
A.5. Quartz crystal microbalance (QCM).....	194
A.6. References	195

A.1. Materials and film deposition

The random copolymer P3HT-co-P3HHT (50% -3HT random comonomer composition; $M_n = 30 \text{ kg mol}^{-1}$, dispersity $\mathcal{D} = 1.9$) was synthesized by Dr. Olivier Dautel at the Institut Charles Gerhardt Montpellier following previously described protocols.¹ Block copolymer P3HT-*b*-PEO ($M_n, P3HT = 5 \text{ kg mol}^{-1}$, $\mathcal{D}_{P3HT} = 1.2$, $M_n, PEO = 20 \text{ kg mol}^{-1}$, $\mathcal{D}_{PEO} \leq 1.2$) was synthesized and provided by Dr. Cyril Brochon at the Laboratoire de Chimie des Polymères Organiques (LCPO). P3HT ($M_n = 23 - 34 \text{ kg mol}^{-1}$, $\mathcal{D} = 2.2$, Sigma-Aldrich) and PEO ($M_n = 20 \text{ kg mol}^{-1}$, $\mathcal{D} \leq 1.2$, Sigma-Aldrich) were purchased. All polymers were dissolved with a concentration of 15 mg mL^{-1} in a 1:1 mixture of THF and NMP (Sigma-Aldrich). Solutions were stirred at $55 \text{ }^\circ\text{C}$ for at least 2 hours to ensure dissolution and homogeneity. Solutions of the neat polymers were mixed and stirred further for at least 30-60 minutes to achieve different blend compositions (10, 25, 33, 40, and 45 wt% P3HT-*b*-PEO), before deposition onto appropriate substrates for subsequent characterization. All glass (Menzel-gläser, 15 mm by 15 mm) and ITO (VisionTek Systems Ltd., 28 mm by 28 mm, $10 \text{ } \Omega \text{ sq}^{-1}$) substrates were cleaned by bath sonication in distilled water, acetone, and IPA, for 15 minutes each, followed by UV-ozone treatment for 15 minutes. Substrates were heated to $75 \text{ }^\circ\text{C}$ before immediately depositing polymer solutions by spin-coating (200CBX, Brewer Science) at various speeds (1000, 2000, 3000, or 3500 rpm) to achieve different thicknesses ($d = 80\text{-}200 \text{ nm}$) measured by mechanical profilometry (Dektak XT-A, Bruker). The films were subsequently dried at $55 \text{ }^\circ\text{C}$ for 3-8 min and then stored in ambient conditions before characterization soon afterward.

A.2. Organic electrochemical transistors (OECT)

A.2.1 Instrumentation

Device characteristics were measured using a Semiconductor Device Parameter Analyzer (B1500A, Keysight Technologies) equipped with modules (B1511B Medium Power SMU and B1510A High Power SMU) for current-voltage application and monitoring, controlled using the Keysight EasyEXPERT group+ GUI based software. Application of input waveforms for transient measurements was done using a separate waveform generator (RSDG 830, RS PRO).

A.2.2 OECT device architecture

OECT devices were fabricated following the general architecture illustrated in **Figure A.1**.

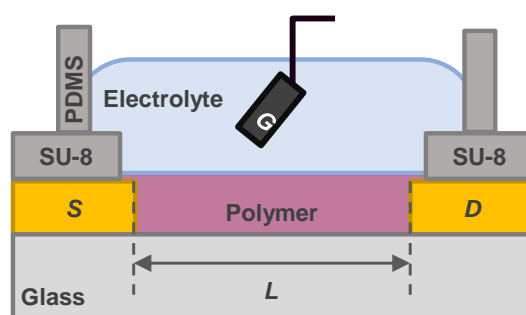


Figure A.1. Schematic diagram of the OECTs used in this work. An Ag/AgCl pellet electrode was used as the gate (G) while patterned gold electrodes were used as the source (S) and drain (D), which were partially insulated from the electrolyte (0.1 M KCl aqueous solution) by a negative photoresist (SU-8).

The photolithographically patterned micro-scale devices were fabricated and provided by Dr. Guillaume Wantz and Dr. Damien Thuau of Laboratoire de l'Intégration du Matériau au Système following protocols reported in literature.^{2,3} The dimensions of the small devices (channel width $W \approx 90 \mu\text{m}$ and lengths $L \approx 20, 30,$ and $60 \mu\text{m}$) were measured using an optical microscope (Nikon LV100ND) and indicated in **Figure A.2**.

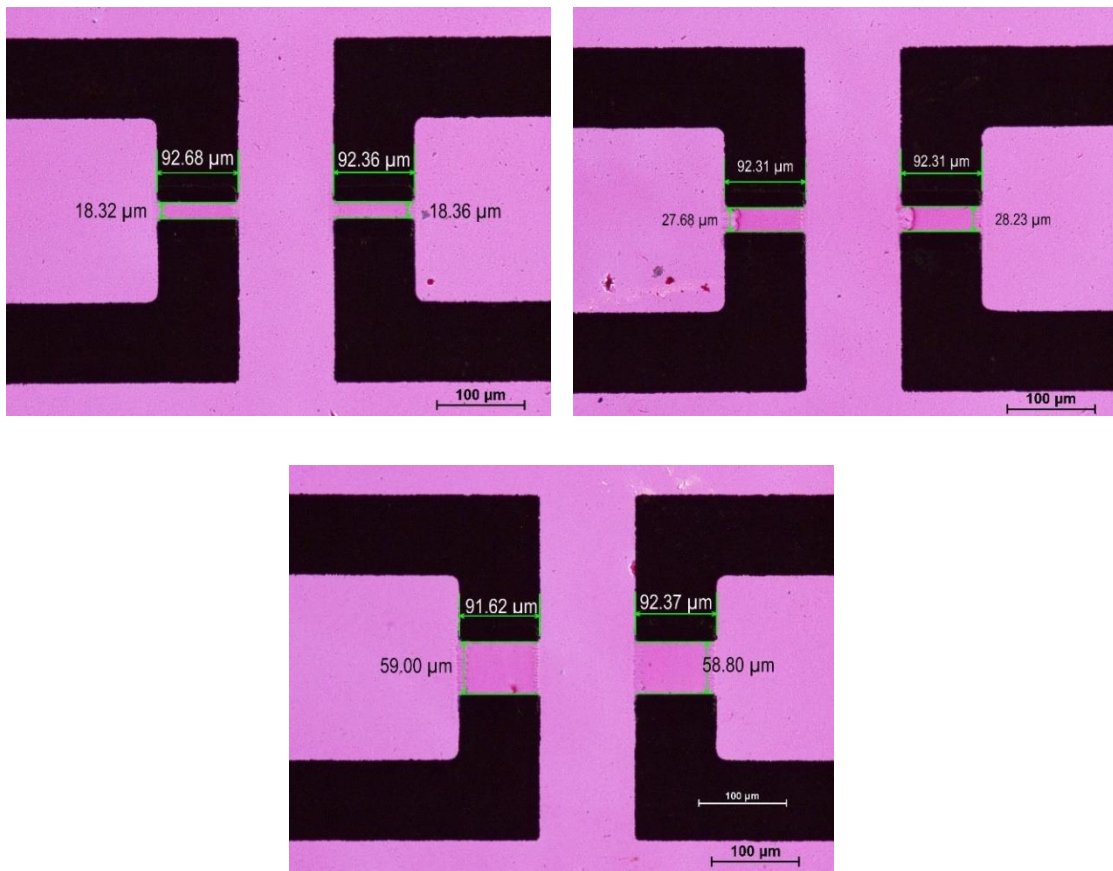


Figure A.2. Optical microscopy images of the patterned source and drain electrodes of micro-scale OECTs with measurements of their widths and lengths indicated.

Larger devices were fabricated by the author. The source and drain electrodes in devices with large channels ($W \approx 2500 \mu\text{m}$, $L \approx 50, 110, 190,$ and $380 \mu\text{m}$) were patterned by vapor-deposition (ME400B, Plassys) of chromium (10 nm) followed by gold (100 nm)

through a steel mask onto cleaned glass slides. The chromium layer was integrated to allow better adhesion of gold onto the glass surface. Each substrate consisted of electrodes worth three devices. For practical reasons, the large devices did not consist of a patterned insulator between electrodes. Instead, the devices were parted by simply scratching or wiping off the semiconducting polymer around the active channel area and electrode interconnects. A PDMS well was positioned over the channels to hold an aqueous electrolyte of 0.1 M of KCl (Sigma-Aldrich) dissolved in deionized water (18.2 M Ω , dispensed from Purelab Flex, ELGA LabWater). The circuit was completed by submerging an Ag/AgCl cylindrical pellet electrode (Warner Instruments, height = 2 mm, diameter = 2 mm) in the electrolyte as the gate electrode. We note that measurements of the transconductances and μC^* parameter of devices of P3HT-co-P3HHT in **Figure A.3** ($V_d = -0.6$ V, V_g sweep rate = 0.04 V s $^{-1}$, $|V_t - V_g| = 0.2$ V) show that no significant difference in performance was observed depending on how the large devices were separated, indicating a relatively robust architecture.

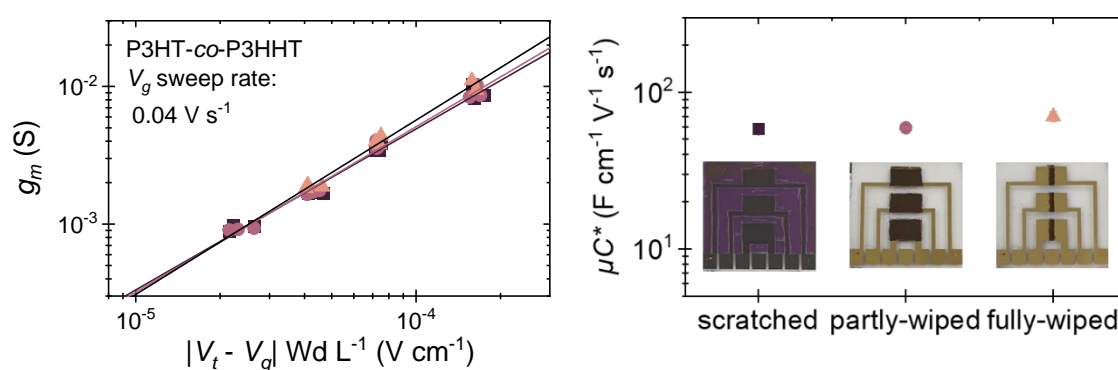


Figure A.3. Scaling of transconductances (g_m , left) lead to values of μC^* (right) measured for various large devices of P3HT-co-P3HHT. No significant difference is observed whether the devices are separated either by scratching the polymer film or completely wiping the contact electrodes, as shown in the inset images.

A.2.3 OECT measurement parameters

The output curves were obtained by measuring I_d over V_d (0 to -0.8 V at 50 mV increments) at constant V_g (0.2 to -0.8 V at 50 mV increments) using various V_d sweep rates (0.25 and 0.50 V s⁻¹, as indicated in the main text). The transfer curves were obtained by measuring I_d over V_g (0.2 to -0.8 V at 50 mV increments) at constant V_d (-0.6 V unless otherwise stated in the main text) using various V_g sweep rates (0.01 to 10 V s⁻¹, as indicated in the main text). The values of g_m were extracted from differentiating the transfer curves, while V_t and ΔV_t were extracted from plots of $|I_d|^{1/2}$ vs V_g , explained further in the main text. The μC^* parameter was extracted from plotting the g_m extracted at $|V_t - V_g| \approx 0.2$ V from devices of different channel dimensions. The transient currents were measured during application of a V_g step from 0 to -0.6 V or application of various V_g waveforms (detailed in the main text) at a constant V_d of -0.4 V.

A.2.4 OECT operational stability in water

To test their long-term operational stability when interfacing with water-rich media, the OECTs were first characterized upon fabrication then stored in deionized water. The same devices were measured periodically to track the evolution of their performance while continuously stored in water.

A.3. Characterization of physical properties

A.3.1 Grazing incidence wide angle x-ray scattering (GIWAXS)

The polymer samples were spin-cast onto cleaned silicon wafer chips following the same film deposition protocols outlined above. GIWAXS characterization was performed at

NSLS-II (CMS 11-BM Beamline). Chips were cut into 5 x 5 mm² and positioned in a vacuum chamber. Automated sample alignment procedure was performed prior to irradiating the samples for data collection. X-rays with 13.5 keV beam energy ($\lambda = 0.918402 \text{ \AA}$) were used to probe the structure of the thin films and scattering patterns were collected onto a 2D Pilatus CCD detector (pixel size 0.172 x 0.172 mm²), positioned at a distance of roughly 26 cm from the sample. A silver behenate standard was used to calibrate sample-to-detector distance (258.1 mm) and beam center x- and y-positions using 9 ring-shaped reflections. NIKA version 1.75 package⁴ within IGORPro v.6.37, along with some custom macros developed at NIST, was used to perform calibration, GI correction and general image treatment.

A.3.2 Differential scanning calorimetry

The polymer samples (1-2 mg) were drop-cast from solution (80 μL of 15 mg mL⁻¹ THF:NMP) onto microscope glass slides (VWR, 75 mm by 25 mm) at 75 °C, dried at 55 °C, and then quenched to room temperature, following similar protocols employed when depositing films for OECT and polymer/ITO electrode fabrication. The films were dried further overnight under a fume hood, then shred to fine pieces and loaded into aluminium crucibles (ME-26763, Mettler Toledo, 40 μL). DSC 1 (Mettler Toledo) was used to record the first heating trace (-90 °C to 280 °C at a rate of 20 °C min⁻¹), the cooling trace (280 °C to -90 °C at a rate of -5 °C min⁻¹), and the second heating trace (-90 °C to 280 °C at a rate of 20 °C min⁻¹) of the samples.

A.3.3 Optical microscopy

A Nikon LV100ND optical microscope equipped with polarizer was used to capture images of the films in transmission mode.

A.3.4 Contact angle measurements

A DSA100 drop shape analyzer (KRÜSS) was used to measure the water contact angles of the various polymer films by sessile drop method. Specifically, the wetting angle between the droplet contour and the contacted surface was measured, depicted in **Figure A.4**. Lower angles ($< 90^\circ$) indicates better wettability of the surface.⁵ The angles were measured immediately upon contact of the water drop to the polymer surface ($t = 0$ s) and a short period after droplet-surface contact ($t = 30$ s), showing no significant change in the average value within this time period.

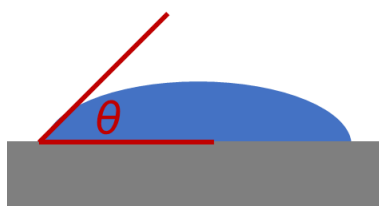


Figure A.4. Diagram depicting the water contact angle (red) reported in this work.

A.4. Electrochemical characterization

Cyclic voltammetry, spectroelectrochemistry and electrochemical impedance spectroscopy were performed on polymer-coated ITO electrodes using a VersaSTAT3 potentiostat (Princeton Applied Research) and accompanying VersaStudio software.

A.4.1 Cyclic voltammetry

Cyclic voltammograms of polymer-coated ITO electrodes were measured at room temperature (22 °C) against a Pt/Ti wire as counter electrode (ET078, eDAQ) and Ag/AgCl reference electrode (MF-2056, BASi) in 0.1 M TBAPF₆ in acetonitrile (Sigma-Aldrich) as organic electrolyte and 0.1 M KCl (Sigma-Aldrich) as aqueous electrolyte (active area = 0.18 cm²). Voltammograms were measured over four cycles and showed no significant changes for all materials investigated. Results from the fourth cycle was reported here for each material.

Anodic peak currents in the voltammograms of P3HT-*co*-P3HHT and its blends were more easily identifiable within the limits of the potential window that could be employed with an aqueous electrolyte (-0.4 to 0.8 V) at slower cycling speeds (see **Figure A.5**). Hence, only results from slow scan rates (2 mV s⁻¹) were discussed in main text. Nonetheless, the voltammograms measured at faster scan rates (30 mV s⁻¹) seem to indicate lower oxidation onset potentials in the blend (\approx 0.1 V) than in the neat P3HT-*co*-P3HHT (\approx 0.3 V), similar to what was observed in the results from slower measurements and discussed in the main text.

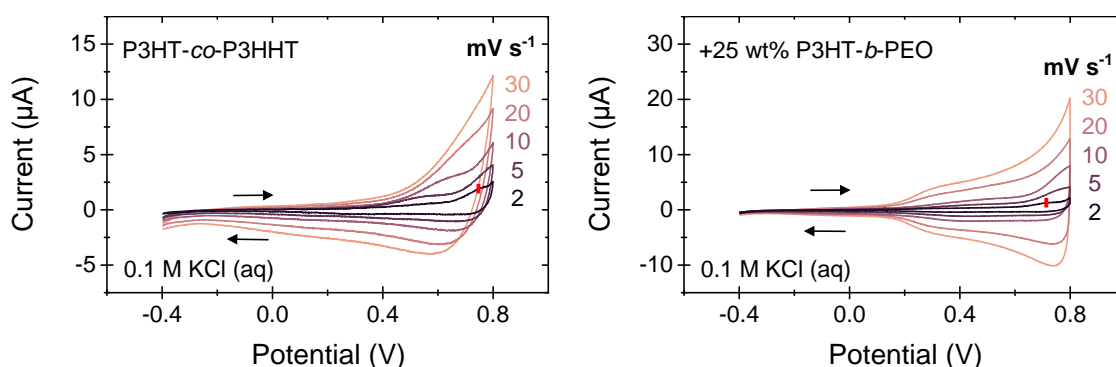


Figure A.5. Cyclic voltammograms of P3HT-*co*-P3HHT measured against Ag/AgCl as reference at various indicated scan rates in 0.1 M KCl aqueous electrolyte. Identifiable peak anodic current is indicated (solid red tick).

A.4.2 Spectroelectrochemistry

The polymers were characterized by spectroelectrochemistry to investigate their electrochemical doping behavior, tracking changes in the absorbance due to polaron formation upon electrochemical oxidation of the polymer backbone, as previously reported.¹ The experimental set-up is illustrated in **Figure A.6**.

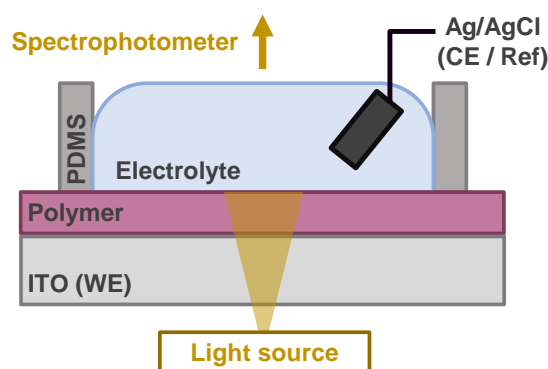


Figure A.6. Schematic diagram of spectroelectrochemistry set-up.

The neutral absorbance of the films as-cast was first measured using a UV-Vis Spectrophotometer (UV-2600, Shimadzu) equipped with a thin film sample holder in reference to a blank substrate. During doping experiments, a USB-spectrometer (CXR-SR-50, StellarNet) connected by fiber optic actuators to a stand equipped with collimating lenses was used to collect UV-vis absorption data in transmission while applying potential steps (0.75, 0, and -0.75 V) on polymer-coated ITO electrodes in 0.1 M KCl (active area = 0.49 cm²) against the same Ag/AgCl pellet electrode used in OECT characterization. The bias was sustained long enough until saturation of the absorbance intensity and current was observed (about 20-30 s for doping, 10 s for de-doping). At least 3 to 5 doping/de-doping cycles were performed on each sample to check for significant irreproducibility of behavior, of which none was observed. Data was processed using OriginPro software.

A.4.3 Electrochemical impedance spectroscopy

The impedance spectra of polymer-coated ITO electrodes of different thicknesses were measured against a Pt/Ti wire as counter electrode (ET078, eDAQ) and an Ag/AgCl wire as pseudo-reference electrode (ET073, eDAQ) in 0.1 M KCl electrolyte (active area = 0.18 cm²). An AC signal with 10 mV amplitude was applied to the polymer over the frequency range of 0.1-10000 Hz, while simultaneously applying DC bias to characterize the behavior of the doped films. A chronoamperometric experiment was performed immediately prior to the impedance measurements by applying a DC potential to the polymer until currents stabilized (after about 10-30 s) to ensure that the polymer was in the targeted doped state. The raw data were fitted with the equivalent circuit described in the main text using an EIS spectrum analyser software available online (<http://www.abc.chemistry.bsu.by/vi/analyser/>).⁶

A.5. Quartz crystal microbalance (QCM)

Measurements were performed using a QCM crystal oscillator (QCM25, Stanford Research Systems) connected to a digital controller (QCM200, Stanford Research Systems) equipped with a built-in frequency counter. Polished, AT-cut quartz crystals with chromium/gold keyhole style electrodes and resonance frequency of 5 MHz (O100RX1, Stanford Research Systems) were used as the QCM sensors, which could be fixed to a crystal holder with the active face exposed. The sample holder comprised of electrode contact springs connected to the oscillator *via* a BNC connector. For measurements in “dry” conditions, a home-built gas chamber was fixed around the crystal holder with inlet and outlet tubes for nitrogen gas flow (0.5 L min⁻¹) regulated by a multichannel gas controller (647C, MKS Instruments). For measurements in “wet” conditions, the gas chamber was detached from the sample holder, which was then immersed in a water (milliQ) bath at 25

°C without removing or replacing the crystal sensor. Each instance that the surrounding media was changed, a varactor equipped in the QCM instrument was adjusted to nullify shunt capacitances for more accurate resonant frequency measurement as specified by the manufacturer.⁷

Measurements were performed in each media for at least 60 to 90 minutes continuously to reach steady state conditions. The blank crystal sensors were first measured in dry (f_0) and wet ($f_{0,wet}$) conditions for reference. The pre-characterized sensors were then coated with the polymer films to be analyzed following the same deposition protocols described above. The coated crystals were first measured in dry conditions to characterize the as-cast films (Δf_{dry}) then measured in wet conditions ($\Delta f_{wet,x}$), after which the samples were removed from the water bath without detaching from the sample holder and dried by carefully purging the exposed sensor face and the sample holder with compressed air. These dry-wet measurement cycles were performed three times ($X = 3$) for each sample to detect any progressive effects of water immersion as discussed in the main text.

A.6. References

1. Pacheco-Moreno, C. M. *et al.* The Importance of Materials Design to Make Ions Flow: Toward Novel Materials Platforms for Bioelectronics Applications. *Adv. Mater.* **29**, 1604446 (2017).
2. Nicolini, T. *et al.* A Low-Swelling Polymeric Mixed Conductor Operating in Aqueous Electrolytes. *Adv. Mater.* **33**, 1–7 (2021).
3. Giovannitti, A. *et al.* N-type organic electrochemical transistors with stability in water. *Nat. Commun.* **7**, 1–10 (2016).
4. Ilavsky, J. Nika: Software for two-dimensional data reduction. *J. Appl. Crystallogr.*

- 45**, 324–328 (2012).
5. Huhtamäki, T., Tian, X., Korhonen, J. T. & Ras, R. H. A. Surface-wetting characterization using contact-angle measurements. *Nat. Protoc.* **13**, 1521–1538 (2018).
 6. Bondarenko, A. S. & Ragoisha, G. A. Inverse Problem In Potentiodynamic Electrochemical Impedance. in *Progress in Chemometrics Research* (ed. Pomerantsev, A. L.) 89–102 (Nova Science Publishers, 2005).
 7. Stanford Research Systems. QCM200: Operation and service manual. (2018). Available at: <https://www.thinksrs.com/downloads/pdfs/manuals/QCM200m.pdf>.

